DANISH METEOROLOGICAL INSTITUTE

SCIENTIFIC REPORT

99-6

Retrieval Analysis and Methodologies in Atmospheric Limb Sounding Using the GNSS Radio Occultation Technique

Stig Syndergaard

COPENHAGEN 1999

ISSN Nr. 0905-3263 (printed)
ISSN Nr. 1399-1949 (online)
ISBN-Nr. 87-7478-394-7

Preface

This PhD thesis is based on research done during a three year study at the Danish Meteorological Institute. Part of the study was done at the University of Arizona, Tucson, Arizona, during a nine month visit from Sep. 1996 to May 1997. The thesis has been accepted by the Niels Bohr Institute for Astronomy, Physics and Geophysics, Faculty of Science, University of Copenhagen, Denmark, as a partial fulfillment of the requirements for the attainment of the PhD degree.

The thesis consists of a main body supplemented with three published or recently submitted papers attached as Appendix C. Emphasis has been placed on selected subjects within the retrieval mechanism of radio occultation data, subjects that I have found as candidates for a more profound study, and which, in some cases resulted in improvements or new ideas of retrieval methods. Thus, not all aspects of the radio occultation technique are covered with equal weight.

The development and implementation of processing software going from GNSS (Global Navigation Satellite System) phase measurements to atmospheric profiles of bending angles, refractivity, pressure and temperature has been a part of the study. All but a few results presented in this thesis are obtained with this software. The forward modeling of phase measurements has been obtained with a ray tracing code named ROSAP (Radio Occultation Simulator for Atmospheric Profiling) developed in connection with an ESA (European Space Agency) study [*Høeg et al.*, 1996] prior to the present study. Only a few modifications of the ray tracing code has been implemented during the present study. All the software made by the author is available on request.

The papers in Appendix C.1 and C.3 have been slightly changed from their submitted versions, edited for misprints and grammar errors discovered after the submission of the papers and the submission of the first version of this thesis. An apparent inconsistency regarding the terminology used for the phase measurements has been clarified in the paper in Appendix C.1.

The study has been carried out under the supervision of my advisers, Per Høeg, at the Danish Meteorological Institute, and Carl Christian Tscherning and Klaus Mosegaard, both at the University of Copenhagen. The research was funded by a grant from the Danish Space Board.

October 1999

Stig Syndergaard
E-mail: ssy@dmi.dk

Abstract

The Global Positioning System (GPS) continuously transmit radio waves at two frequencies. The signals are affected by the electron density in the ionosphere and by the pressure, temperature and moisture in the neutral atmosphere. Since April 1995, with the launch of the GPS/MET experiment, it has been possible to utilize these signals to obtain information about the ionosphere and the neutral atmosphere, using the radio occultation technique. From the proof-of-concept GPS/MET radio occultation experiment atmospheric temperature with very high vertical resolution ($\sim$ 1 km) has been achieved with an accuracy of about 1–2 Kelvin up to 30–40 km altitude. In the tropical troposphere, where water vapor is appreciable, profiles of the water vapor pressure can be obtained using auxiliary information of the temperature.

The occultation data are inverted using the Abel transform assuming local spherical symmetry. The spherical symmetry assumption gives a unique relation between the signal bending angle and the refractive index in the atmosphere. Assuming a dry atmosphere and applying the hydrostatic equilibrium assumption together with the equation of state, it is possible to derive vertical profiles of the so-called *dry temperature*.

In this thesis an error covariance analysis, in the geometrical optics approximation, taking into account the bending and defocusing of rays in the lower part of the atmosphere, is presented. The results reveal that a relatively high degree of vertical correlation can be expected when applying the hydrostatic integration to obtain pressure and temperature profiles. A simulation study shows that this vertical correlation is decreased substantially when using model profiles of bending angles at the high altitude end, e.g. by applying statistical optimization techniques.

A new and improved phase path correction method for calibration of ionospheric effects, and dealing with the problem of ray path separation, is presented. Through Taylor expansions, using the assumption of spherical symmetry, formulas are derived showing how both the dispersion and second order ionospheric effects can be mitigated using measurements of the satellite-to-satellite integrated electron content. The residuals for various conditions in the ionosphere are estimated numerically and compared to the analytic estimates. The remaining bending angle residual bias is of the order of a few tenths of a μrad under extreme ionospheric conditions. A formulation of the difference between this improved phase path correction method and the traditional bending angle correction method is obtained and confirmed by simulation results. Further improvements involving a triplex-frequency combination is also discussed.

The neglect of the Earth's oblateness in the retrieval of temperature profiles may cause a bias at altitudes below 40 km. From this altitude the temperature bias increases downwards, and can, in extreme cases, become as large as 3 K at 10 km altitude and 6 K at the ground. The size of the bias depends on the occultation geometry and the geographical latitude of the limb zone. A method to correct for the bias is proposed using

an assumption of local spherical symmetry tangential to the ellipsoid. After a simple correction, dry temperature profiles are retrieved within 0.25 K ($\sim 0.1\%$) accuracy at the ground. It is shown that the orientation of the occultation plane has to be taken into account in the correction procedure if pressure profiles are to be retrieved to better than 0.4% accuracy.

Using the assumption of local spherical symmetry, horizontal refractivity gradients may cause retrieval errors in the temperature of a few Kelvin. Simulations show that even in the vicinity of an intense frontal system, errors are generally not larger than 2 K.

Retrieval algorithms are applied to data from the GPS/MET experiment and results are validated against radiosonde data and data from numerical weather analyses.

Acronyms and Abbreviations

AMSU	Advanced MSU
AS	Anti-Spoofing
ATOVS	Advanced TOVS
CHAMP	Challenging Microsatellite Payload
DMI	Danish Meteorological Institute
DMSP	Defense Meteorological Satellite Program
DoC	Department of Commerce
DoD	Department of Defense
ECMWF	European Centre for Medium-Range Weather Forecasts
EPS	EUMETSAT Polar System
ESA	European Space Agency
EUMETSAT	European Organisation for the Exploitation of Meteorological Satellites
GLONASS	Global Navigation Satellite System (Russian constellation)
GNSS	Global Navigation Satellite System (general constellation)
GOES	Geostationary Operational Environmental Satellite
GPS	Global Positioning System
GPS/MET	GPS/Meteorology
HALOE	Halogen Occultation Experiment
HIRS	High-resolution Infrared Radiation Sounder
LEO	Low Earth Orbit
METOP	Meteorological Operational (satellite)
MLS	Microwave Limb Sounder
MSISE	Mass Spectrometer and Incoherent Scatter (model) - Extended
MSU	Microwave Sounding Unit
NASA	National Aeronautics and Space Administration
NCEP	National Centers for Environmental Prediction
NOAA	National Oceanic and Atmospheric Administration
NPOESS	National Polar-orbiting Operational Environmental Satellite System
NWP	Numerical Weather Prediction
RMS	Root Mean Square
ROSAP	Radio Occultation Simulator for Atmospheric Profiling
SA	Selective Availability
SAC-C	Satelite de Aplicaciones Cientificas - C
SSU	Stratospheric Sounding Unit
SSM/T-1	Special Sensor Microwave Temperature Sounder

SSM/T-2	Special Sensor Microwave Water Vapor Sounder
S–S	Satellite-to-Satellite
SUNSAT	Stellenbosch University Satellite
TEC	Total Electron Content
TIROS	Television Infrared Observation Satellite
TOVS	TIROS Operational Vertical Sounder
UARS	Upper Atmosphere Research Satellite
UCAR	University Corporation for Atmospheric Research
US	United States

Contents

Preface **iii**

Abstract **iv**

Acronyms and Abbreviations **vi**

1 Introduction **1**
1.1 Background 1
1.2 Principle of GNSS Radio Occultations 5
1.3 The Refractive Index and Refractivity 8
1.4 The Abel Transform 9
1.5 General Retrieval Methodology 10

2 Error Sources and Resolution **13**
2.1 Double Differencing 13
2.2 Random Errors 14
2.3 Systematic Errors 15
2.4 Illegitimate Errors 16
2.5 Vertical Resolution 18
2.6 Horizontal Resolution 18

3 Random Error Propagation **19**
3.1 Error Covariance Analysis 20
3.1.1 Excess Phase Filtering 21
3.1.2 Excess Doppler 25
3.1.3 Bending Angles 27
3.1.4 Refractivity 31
3.1.5 Dry Pressure 35
3.1.6 Dry Temperature 37
3.1.7 Discussion of Results 38
3.2 Simulation of Temperature Errors and Correlations 42
3.2.1 Results 43
3.2.2 Empirical Relation Between Phase and Temperature Errors . . . 46

4 Systematic Errors and Improvements **48**
4.1 Ionosphere Calibration 48
4.2 The Spherical Symmetry Assumption 49
4.2.1 Impact of Earth's Oblateness 50

4.2.2 Atmospheric Frontal System 52

5 Conclusions and Prospects **56**
5.1 Conclusions 56
5.1.1 Random Error Propagation 56
5.1.2 Ionosphere Calibration 58
5.1.3 Impact of Earth's Oblateness 60
5.1.4 Atmospheric Frontal System 60
5.2 Prospects 60

Acknowledgments **62**

References **63**

Appendices **70**

A Discretization of the Abel Transform **70**

B Refractivity Field of a Front **72**

C Published and Submitted Papers **76**
C.1 On the Ionosphere Calibration in GPS Occultation Measurements . . . 77
C.2 Modeling the Impact of the Earth's Oblateness on the Retrieval of Temperature and Pressure Profiles from Limb Sounding 103
C.3 Inversion of GPS Occultation Data for Atmospheric Profiling 115

Chapter 1

Introduction

1.1 Background

Precise quantitative knowledge of the atmospheric state is an indispensable input to Numerical Weather Prediction (NWP) models. As NWP models become increasingly complex, taking into account more and more relevant physical and dynamical processes, and doing this on a finer and finer scale—and as computers become faster—the possibility of predicting the weather several days ahead in time, relies considerably on the initial conditions that we put into the models. At present, uncertainties in the initial conditions does not allow useful forecasts more than 5–6 days ahead. Also, precise measurements and monitoring of various atmospheric parameters can help to the further understanding of many of the physical and dynamical processes in the atmosphere, eventually leading to improved NWP models and forecasts. Long-term monitoring of specific parameters over periods of years, gives input to climate research as well.

Radiosonde (balloon borne instrument packet) soundings have for a long time been the most effective way of collecting important atmospheric parameters like pressure, temperature, moisture, and wind. The first radiosonde stations was inaugurated by the US Weather Bureau in 1936 to obtain upper air soundings on a routine basis [*Hopkins*, 1996]. In 1991 more than 1000 radiosonde stations were operated worldwide [*Rocken et al.*, 1997] and they have become the backbone of the global upper air observing system, providing input to NWP models. At each station, radiosondes are usually launched twice a day, providing high vertical resolution data from near the surface to an altitude of about 20–30 km, where the balloon bursts due to the surrounding low pressure. Under ideal conditions radiosonde temperatures are accurate to within 0.5 K and relative humidities are accurate to within a few percent. In the upper troposphere and stratosphere temperature accuracy is degraded, with typical errors of 1 K above 250 hPa ($\sim$ 10 km) increasing to as large as 4 K at 10 hPa ($\sim$ 30 km) [*Rocken et al.*, 1997]. Unfortunately, radiosonde stations are not evenly distributed over the Earth. Most stations are in the northern hemisphere and there is only a very few stations in oceanic regions.

With the "satellite age" remote sensing of the terrestrial atmosphere has become a very powerful method to obtain additional data—especially in deserted areas and over the oceans—and to extend our knowledge about the atmosphere. Since the early 1960's satellites have made it possible to observe the atmosphere in any area of the globe, and related to a wide range of altitudes. This have had a major impact on atmospheric

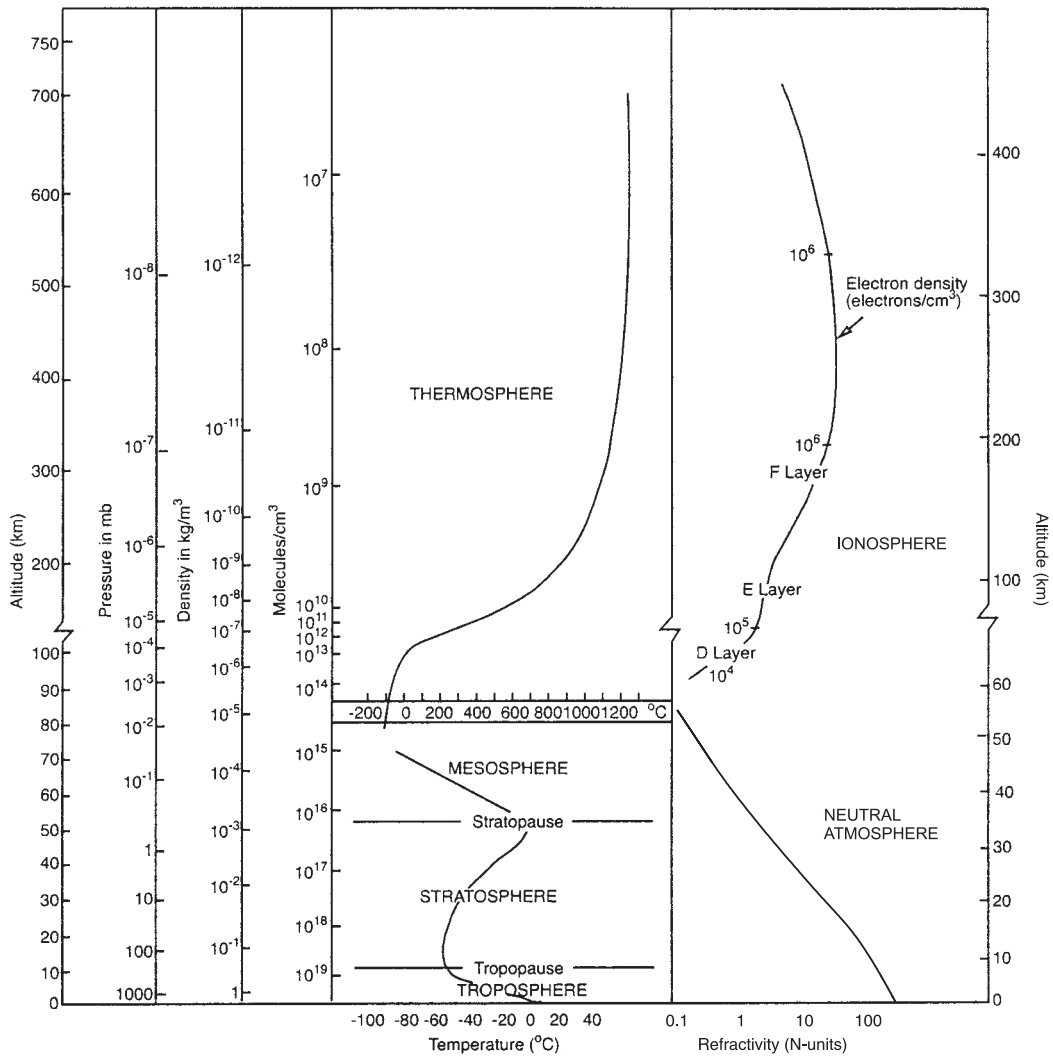

Figure 1.1 The mean vertical structure of Earth's atmosphere showing the temperature, refractivity, and electron density distributions. The refractivity is for L-band (1–2 GHz) frequencies (adapted from *Rocken et al.* [1997]).

sciences and weather forecasting.

Many atmospheric parameters can be provided by, or derived from remote sensing measurements using satellites. To limit the discussion below we shall concentrate on the temperature and humidity observations only. The succeeding sections and chapters mostly deals with the atmospheric refractivity, pressure, and temperature in the troposphere, stratosphere, and mesosphere, and to a lesser extent, the tropospheric water vapor and the ionosphere electron density. Figure 1.1 gives an overview of the mean vertical temperature and refractivity distribution in the atmosphere and the electron density distribution in the ionosphere as well as the nomenclature used for the different spheres and layers.

In satellite remote sensing, vertical profiles of temperature and water vapor are usually derived from passive observations of radiances. Several instruments on different satellite platforms are/have been able to provide such data. One of them, the GOES-

I/M Sounder on board the Geostationary Operational Environmental Satellites (GOES), placed over the US, measures the radiation at different wavelengths originating from broad layers in the atmosphere. With a first guess profile the data are then inverted to obtain temperature and humidity profiles. However, the quality of the GOES temperature soundings is questionable, because normally the temperature retrieval is not very different from the first guess, and thus does not provide much new information. *Rocken et al.* [1997] compare GOES temperatures with NCEP temperatures and other correlative temperature data, and demonstrate that there is a large bias in the GOES soundings at altitudes above 25 km.

Another operational system, the TIROS-N/NOAA series of polar orbiting satellites, also provides tropospheric and stratospheric temperature profiles as well as vertically integrated moisture content using infrared and microwave emissions at a variety of wavelengths [*Smith et al.*, 1979]. The TIROS Operational Vertical Sounder (TOVS) is in fact three instruments complementing each other and giving tropospheric water vapor and temperature profiles from the surface and up to about 50 km. The TOVS consists of the High-resolution Infrared Radiation Sounder (HIRS), the Microwave Sounding Unit (MSU) and the Stratospheric Sounding Unit (SSU). A new instrument, the Advanced MSU (AMSU) is soon replacing the MSU and the SSU, so that the Advanced TOVS (ATOVS) consists then of the HIRS and the AMSU [*Eyre and Offiler*, 1998]. In cloud-free areas, temperature differences between TOVS and NCEP analyses has been reported to be about 2–3 K [*Rocken et al.*, 1997].

The DMSP (Defense Meteorological Satellite Program) near polar orbiting satellites are yet another system of satellites worth mentioning. The DMSP satellites also have both a temperature sensor, SSM/T-1, and a humidity sensor, SSM/T-2, on board. Temperature can be retrieved with an accuracy of about 3 K between the surface and 10 hPa ($\sim$ 30 km), while the relative humidity can be retrieved to about 30% [*Rieder*, 1998].

Like the GOES-I/M Sounder the TOVS, ATOVS, and SSM/T sounders are all near nadir viewing instruments, and the resulting vertical resolution is therefore rather poor. The vertical resolution of the GOES-I/M Sounder is 3–5 km [*Haskell and Mikkelsen*, 1999] and for the TOVS the combined vertical resolution is 2–3 km in cloud-free areas and worse in cloudy areas [*Eyre and Offiler*, 1998]. However, the horizontal resolution of these systems is rather well, being about 50 km for the GOES [*Haskell and Mikkelsen*, 1999] and 20–150 km for the TOVS [*Antikidis et al.*, 1998].

The Upper Atmosphere Research Satellite (UARS), launched in 1991, uses *limb sounding* to measure stratospheric and mesospheric temperatures. It has several limb sounding instruments on board of which two of them are still operating: the Microwave Limb Sounder (MLS) and the Halogen Occultation Experiment (HALOE). The MLS is a passive sounder looking at microwave thermal emission from the limb of the Earth's atmosphere, and giving—among a variety of other parameters—temperature and pressure in the range $\sim$ 25–55 km. The accuracy and vertical resolution, respectively, are varying from 2 K and 1.5 km in the troposphere and lower stratosphere to 5 K and 6 km in the mesosphere [*Fishbein et al.*, 1996]. The HALOE uses solar infrared occultation to measure vertical profiles of various molecular species as well as temperature and pressure profiles in the range $\sim$ 35–85 km. The estimated accuracy of the HALOE is 5–10 K, depending on altitude and validation method, and the resulting vertical resolution is estimated to be about 4 km [*Hervig et al.*, 1996].

The GNSS[1] radio occultation technique complements many of the above mentioned sounding methods. A satellite in a Low Earth Orbit (LEO) utilizes the signals from the existing GNSS constellations (currently the GPS, and potentially the Russian GLONASS or other future constellations) and measures the propagation delay rather than the intensity. The observations gives information on the atmospheric refractivity related to the pressure, temperature and moisture as well as the ionosphere electron density. Accurate temperature profiles ($\sim$ 1 K) can be obtained in the troposphere and stratosphere up to 30–40 km, while profiles of water vapor can be derived in the tropical troposphere using auxiliary temperature information. The GPS signals are transmitted at wavelengths around 20 cm, at which there is only little effect from aerosols, clouds, and rain [*Hardy et al.*, 1994]. The method has an inherently high vertical resolution determined by the first Fresnel diameter [*Melbourne et al.*, 1994], being about 1.5 km in the stratosphere (depending on orbit height) and gradually improving to about 0.5 km in the lower troposphere. In the horizontal direction, the measurement is an integrated effect over a large range along the signal path, though heavily weighted at the ray path tangent point closest to Earth's surface, thus resulting in a 200–300 km horizontal resolution.

Generally the radio occultation method has been widely used in various planetary missions the last 30–35 years, and has given unique information about the atmospheres of the other planets in our solar system [*Kliore et al.*, 1965; *Fjeldbo et al.*, 1971; *Kliore and Woiceshyn*, 1976; *Fjeldbo et al.*, 1976; *Tyler*, 1987; *Lindal*, 1992]. The planetary missions exploit the situation when the spacecraft rises or sets behind the planet as seen from Earth. In these situations radio signals emitted from the spacecraft and received on Earth are subject to refraction due to the planetary atmospheric limb.

Using the occultation method on Earth was first proposed by *Fischbach* [1965], suggesting that a LEO satellite should measure stellar refraction in the Earth's atmosphere. *Lusignan et al.* [1969] analyzed the potentials of a constellation of satellites continuously transmitting signals to each other through the limb of the atmosphere. The first actual satellite radio occultation of Earth's atmosphere came in 1975 using satellite-to-satellite tracking data from the Apollo-Soyuz Test Project. The results of refractivity, pressure and temperature profiles from this lone occultation was reported by *Rangaswamy* [1976], showing the potentials of the method, but also that further study and more accurate measurements were needed to obtain the accuracy levels required for NWP input.

The Global Positioning System (GPS) installed during the 1980's and the early 1990's [e.g., *Seeber*, 1993] provided the foundation for applying the radio occultation technique to the Earth's atmosphere on a regular basis. With the launch of the American GPS/MET (GPS/Meteorology) experiment in April 1995 the technique has now been successfully applied to the Earth's atmosphere [*Feng et al.*, 1995; *Hajj et al.*, 1995; *Ware et al.*, 1996; *Kursinski et al.*, 1996; *Hocke*, 1997; *Rocken et al.*, 1997; *Kursinski*, 1997; *Kuo et al.*, 1998; *Hajj and Romans*, 1998; *Gorbunov and Gurvich*, 1998a; *Steiner et al.*, 1999]. The GPS/MET instrumentation consists of a modified Turbo-Rogue GPS receiver on board a micro-satellite—MicroLab-1—in a 740 km circular orbit with a 70 degree inclination. So far there has only been this one proof-of-concept GPS/MET experiment, but recently, in February 1999, two more micro-satellites, the Danish Ørsted satellite and the South African SUNSAT, both carrying a Turbo-Rogue receiver, were launched and will provide GPS radio occultation data as well.

The GPS/MET experiment has provided researchers with meteorological data of

[1]GNSS is a common acronym for GPS and GLONASS and any similar future constellations.

a high quality. Even though many GPS/MET soundings has failed to penetrate the lowest 5 km of the troposphere in the presence of significant water vapor, *Rocken et al.* [1997] demonstrate 1 K mean temperature agreement with the best correlative data sets (TOVS, MLS, HALOE, radiosondes and global analysis data from NCEP and ECMWF) between 1 and 40 km. Standard deviations are generally found to be less than 2–3 K. Also *Kursinski et al.* [1996] finds good agreement between GPS/MET and ECMWF analyses in the range 5–30 km, with a mean accuracy better than 1 K and standard deviation of 1–2 K. Additionally *Kursinski et al.* [1996] interestingly finds that there is a better agreement in the northern hemisphere than in the southern hemisphere, a result that has recently been confirmed by *Steiner et al.* [1999]. This indicates that the ECMWF analysis, which is heavily based on radiosonde data, is less accurate in data sparse regions like the Southern Pacific than over the continents (primarily Europe and the USA) where the density of radiosonde data is relatively high [*Kursinski et al.*, 1996; *Steiner et al.*, 1999]. Since radio occultation data from the GPS/MET is more or less globally distributed, it is believed that such data, if assimilated into NWP models, may contribute significantly to improved weather predictions. At present, considerable efforts are made to develop techniques for assimilation of radio occultation data into NWP models [*Kornblueh et al.*, 1997; *Zou et al.*, 1995, 1998a, b]

Until the GPS/MET experiment was turned off in 1997 due to lack of funding, it was capable of providing about 150 soundings per day under optimal conditions [*Rocken et al.*, 1997]. Ideally, about 250 occultations are happening each day counting only either setting or rising occultations. Putting both an aft-looking antenna and a forward-looking antenna on a LEO satellite, and including the GLONASS constellation together with the GPS, thus gives about 1000 setting or rising occultations each day. Three such LEO satellites in orbit would provide a globally distributed set of daily profiles twice the number provided by the present radiosonde network [*Kursinski et al.*, 1997].

More satellites carrying GNSS receivers are indeed to come in the near future. Besides Ørsted and SUNSAT, the Argentinian SAC-C and the German CHAMP are probably going to be the next research satellites in line for launch carrying a Turbo-Rogue GPS receiver. On top of that, both US (DoD/DoC/NASA) and European (ESA/EUMETSAT) agencies plan to put several receivers in orbit on the future operational systems, NPOESS and METOP/EPS, perhaps eventually being capable of tracking both the GPS and the GLONASS signals.

1.2 Principle of GNSS Radio Occultations

Since the GPS/MET experiment is only tracking the GPS (not the GLONASS) signals, many considerations in this thesis are based on the GPS constellation. However, all subjects dealt with may in principle apply to the GLONASS or any future GNSS constellations as well. For convenience, and to avoid a detailed discussion about the practical differences between the GPS and the GLONASS, the occultation principle will be described using the characteristics of the GPS (see *Seeber* [1993] for the main differences between the GPS and the GLONASS).

The basis of the GPS/MET occultation experiment is the GPS constellation, originally designed by the US military for precise positioning. The GPS constellation consists of 24 satellites in 6 orbital planes at a distance of about 20,200 km from the Earth's surface. These satellites continuously transmit electro-magnetic waves at two L-band

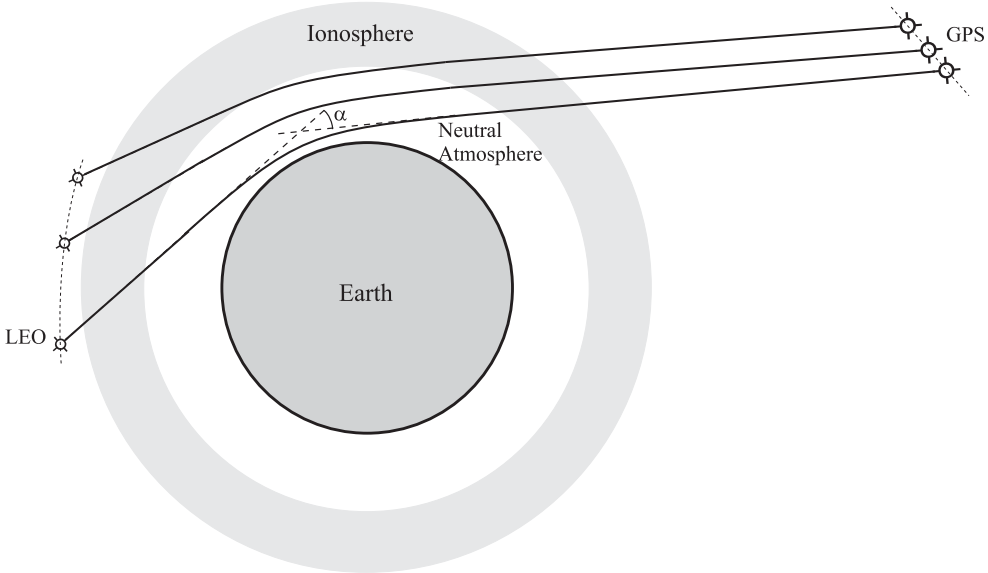

Figure 1.2 Illustration of the occultation geometry. Signals transmitted by a GPS satellite are refracted by the ionosphere and the neutral atmosphere. When received at a LEO-satellite outside the main part of the ionosphere the signals have been subject to bending. The point on the ray that is closest to the Earth's surface is called the ray perigee or tangent point.

frequencies: $f_1 = 1.57542$ GHz, $f_2 = 1.22760$ GHz. In the occultation experiment the signals are received at a Low Earth Orbit (LEO) satellite (generally about 500-2000 km above surface). On their way the signals pass through the Earth's ionosphere and neutral atmosphere (Figure 1.2). In the ionosphere and atmosphere the signals are distorted because of the refractive index of the medium. In the geometrical optics approximation the result is that a signal received at the LEO has been subject to a small bending. If we know the precise positions and velocities of the satellites (in principle obtained by simultaneous observations of different non-occulting GPS satellites), we are able to measure the bending angle, α. Due to the satellite motions, the whole atmosphere from top to surface are scanned, obtaining a set of bending angles related to different heights in the atmosphere. Vertical electron density gradients at the top of the ionosphere F-layer (cf Figure 1.1) will contribute to a net bending away from the Earth, but for rays penetrating layers below the bulk of the ionosphere the total bending will usually be towards the Earth as in Figure 1.2. Below the D-layer of the ionosphere the bending is predominantly determined by the density and its vertical gradients in the neutral atmosphere, increasing almost exponentially as we go down through the atmosphere. For rays close to the surface the bending angle becomes 1–2 degrees depending on the vertical gradients due to water vapor in the lowest part of the atmosphere. In the case that one is only interested in the neutral atmosphere the scanned region is restricted to the lowest ∼100 km of the atmosphere. In this region the GPS/MET Turbo-Rogue receiver collects data at a 50 Hz sampling rate, resulting in approximately 3000 samples with vertical spacings at the tangent points of ~ 50 m or less. Such an occultation takes about 1 minute.

In fact the observable is the phase path (or optical path length), not the bending angle. Ideally the L1 and L2 phase path observables are given by the line integral of the

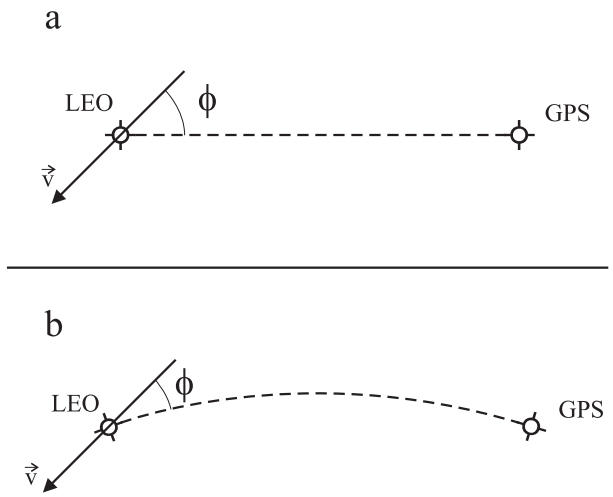

Figure 1.3 Simplistic picture of the measurement. **a)** The vacuum case: the Doppler shift depends on the relative velocities, including the incident angle, ϕ, between the ray direction and the LEO satellite velocity direction. **b)** If the ray is bend due to atmospheric refraction, the Doppler shift is a little different than expected from velocities only.

refractive index, μ, along the ray paths between the GPS satellite and the LEO satellite:

$$L_1 = \int \mu(f_1) ds, \tag{1.1a}$$

$$L_2 = \int \mu(f_2) ds, \tag{1.1b}$$

where ds is an element of length along the ray paths. For microwave frequencies, in the ionosphere the refractive index is less than unity and frequency dependent, while in the neutral atmosphere it is larger than unity and does not depend on the frequency (see equations (1.3) and (1.4) below). In practice the GPS phase observables are only determined to within a constant ambiguity bias being an integer number of wavelengths [e.g., *Han and Rizos*, 1997]. Fortunately only the phase change (i.e., the derivative of the phase path during the occultation) is in practice necessary to derive the bending angle, and from there, the atmospheric parameters.

Without any atmosphere the measured phase change (or Doppler shift) would be that due to the relative satellite motions only. With the atmosphere included, the Doppler shift is a little different due to refraction and bending, giving rise to a slightly different incident angle of the ray path at the LEO satellite (Figure 1.3). The difference between the measured phase path (assuming no phase ambiguities) and the "vacuum" phase path (equal to the geometrical distance between the satellites, R_{LG}) is the *excess phase*[2], ΔL_i $(i = 1, 2)$:

$$\Delta L_i = L_i - R_{\mathrm{LG}}. \tag{1.2}$$

[2]A more complete term would be *excess phase path*. In the literature this quantity has been given many different names. Sometimes it is also termed the *atmospheric phase delay* or derivations thereof. *Rocken et al.* [1997] use the term *excess phase delay* (due to the atmosphere and ionosphere) or shortly *excess phase*. In the paper in Appendix C.2, it is shortly termed the *phase delay*. With this exception it will throughout this thesis be termed the *excess phase*.

For rays with tangent heights above the tropopause, the excess phase is negative due to the penetration of ionospheric layers on both sides of the neutral atmosphere (cf Figure 1.2). Depending on the integrated electron content along the ray paths, simulations have shown that the size of the excess phase is usually of the order of 10 m or less, but may reach more than 100 m at upper altitudes in cases of a dense ionosphere representative of daytime conditions during solar maximum. For rays penetrating the lower atmosphere the effect from the neutral part of the atmosphere exceeds that of the ionosphere, and the excess phase becomes positive around tropopause heights increasing to a size of the order of 1 km for rays with tangent point heights close to the surface. The derivative of the excess phase is the *excess Doppler*. From the excess Doppler and the satellite positions and velocities the total bending angle can be found assuming that the atmosphere is spherically symmetric (Section 1.5 below).

1.3 The Refractive Index and Refractivity

At microwave frequencies, the total refractive index, μ, in the atmosphere is close to unity. For this reason it is convenient to define the refractivity, N, as

$$N = 10^6(\mu - 1). \tag{1.3}$$

The atmospheric refractivity is related to the temperature, T [K], the dry air pressure, p_d [hPa], the partial pressure of water vapor, p_w [hPa], and the ionosphere electron density, N_e [electrons/m^3], as

$$N = k_1\frac{p_\mathrm{d}}{T} + k_2\frac{p_\mathrm{w}}{T} + k_3\frac{p_\mathrm{w}}{T^2} - C\frac{N_\mathrm{e}}{f^2}, \tag{1.4}$$

where k_1, k_2, k_3, and C are constants. The three first terms on the right hand side of (1.4) are the contributions from the neutral atmosphere [*Smith and Wientraub*, 1953], while the last term is the ionospheric contribution. Here we have only retained the first order ionospheric contribution proportional to f^{-2}, f [Hz] being the signal frequency. This term is derived from the more complex Appleton-Hartree dispersion relation giving the refractive index as a function of the electron plasma frequency (depending on the electron density) and the electron cyclotron frequency (depending on the ambient magnetic field) [e.g., *Budden*, 1985]. However, higher order ionospheric terms (as well as the contribution from collisions and positive ion species in the ionosphere) have only limited influence at L-band frequencies [*Melbourne et al.*, 1994; *Høeg et al.*, 1996] (see also Appendix C.1). The values of the three constants ($k_1 = 77.60 \pm 0.05$ K/hPa, $k_2 = 70.4 \pm 2.2$ K/hPa, $k_3 = 3.739 \cdot 10^5 \pm 0.012 \cdot 10^5$ K^2/hPa) has lately been given by *Bevis et al.* [1994] based on a compilation of previous experimental results. The constant $C = 10^6 e^2/8\pi^2\epsilon_0 m_\mathrm{e} \approx 40.3 \cdot 10^6$ m^{3}s^{-2} is based on fundamental physical constants (e is the elementary charge, ϵ_0 is the vacuum permitivity, and m_e is the electron mass). One more term, not included in (1.4), is a scattering term due to liquid water droplets suspended in the atmosphere. For realistic suspensions of water or ice this term is small in comparison with the terms included in (1.4) and is therefore neglected [*Kursinski*, 1997; *Kursinski et al.*, 1997].

Since $k_2 \approx k_1$ and $p_\mathrm{w} \ll p_\mathrm{d}$, the second term in (1.4) is usually included in the first term, resulting in the approximation

$$N = k_1\frac{p}{T} + k_3\frac{p_\mathrm{w}}{T^2} - C\frac{N_\mathrm{e}}{f^2}, \tag{1.5}$$

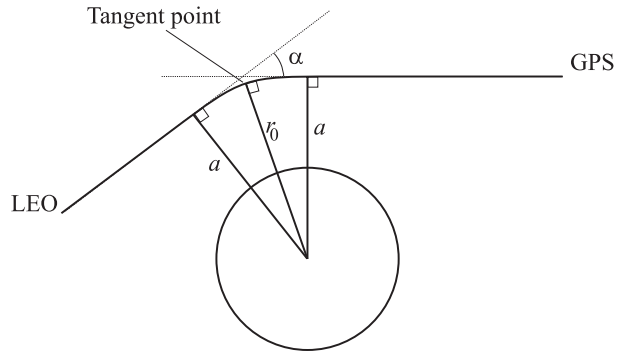

Figure 1.4 The geometry of the occultation is assumed to be spherically symmetric. The impact parameter is defined as the perpendicular distance between either of the ray asymptotes and the center of refraction.

where $p = p_{\mathrm{d}} + p_{\mathrm{w}}$ is the total pressure. To be more accurate the value of k_3 should then be corrected accordingly [*Smith and Wientraub*, 1953], and reduced by about 0.5%.

Since the GPS satellites are transmitting at two frequencies, the first order ionospheric effects on the bending angles may be eliminated to obtain neutral atmospheric bending angles related to the neutral atmosphere refractivity only. Ignoring also the water vapor contribution, which is a fair assumption at high latitudes, a simple relation between refractivity and atmospheric pressure and temperature is then obtained:

$$N = k_1 \frac{p}{T}. \tag{1.6}$$

Generally the water vapor in the lower troposphere can be neglected in regions colder than 250 K [*Kursinski et al.*, 1996]. In the tropical troposphere (1.6) is not sufficient and the derived temperature using (1.6) is therefore often denoted as the *dry temperature*.

1.4 The Abel Transform

In a spherically stratified medium there is a unique relation between the bending angle and the refractive index as a function of radius, r. This relation can be derived from Bouger's rule for a spherically stratified medium and yields [e.g., *Fjeldbo et al.*, 1971]

$$\alpha(a) = -2a \int_{r_0}^{\infty} \frac{d \ln \mu / dr}{\sqrt{\mu^2 r^2 - a^2}} dr, \tag{1.7}$$

where bending towards the Earth is counted positive. The bending angle is connected to an impact parameter, a, which is an invariant for a given ray and can be defined as the perpendicular distance between either of the ray asymptotes and the center of refraction (Figure 1.4). The tangent radius, r_0, is the radial distance from the center to the tangent point, and is related to the impact parameter and the refractive index at the tangent radius as

$$r_0 = \frac{a}{\mu(r_0)}. \tag{1.8}$$

Having the bending angles as a function of impact parameters as measured from the radio occultation data, we are interested in the refractive index as a function of altitude

(radius) in the atmosphere—an inverse problem. *Fischbach* [1965] and *Phinney and Anderson* [1968] pointed out that there exists an analytic transform to this problem, and that the solution is formally equivalent to the Herglotz-Wiechert method for interpreting seismic data [e.g., *Aki and Richards*, 1980]. The transform is in fact a special case of the more general *Abel transform*, named for the nineteenth-century Norweigen mathematician, Niels Henrik Abel. In our case, the Abel transform—as derived by *Fjeldbo et al.* [1971]—results in

$$\mu(r_0) = \exp\left(\frac{1}{\pi}\int_a^\infty \frac{\alpha(x)}{\sqrt{x^2-a^2}}dx\right). \tag{1.9}$$

Given an impact parameter, a, and the physical relation between bending angles and impact parameters above that a, the refractive index can now be found directly at the tangent radius subsequently calculated from (1.8). The validity of the spherical symmetry assumption is discussed in Section 4.2.

1.5 General Retrieval Methodology

As mentioned, the observables are the phase paths, L_1 and L_2, at two frequencies (equations (1.1a) and (1.1b)). Since the ionosphere refractivity to first order is inverse proportional to the frequency squared, the first order contribution from the ionosphere can be eliminated to a certain extent by applying a linear combination of L_1 and L_2 at the same time samples, to obtain the *ionosphere corrected* phase path, L_C:

$$L_\mathrm{C} = \frac{f_1^2 L_1 - f_2^2 L_2}{f_1^2 - f_2^2}. \tag{1.10}$$

Because of the bending, the L1 and the L2 signals follow slightly different paths and are thus not experiencing the exact same environment. This, together with higher order ionosphere terms gives rise to a residual still remaining after calibration using (1.10). Better correction methods can be applied and is discussed in detail in Section 4.1 and Appendix C.1. For now, as an introductory outline of the processing chain, we shall assume that we have been able to eliminate the entire contribution from the ionosphere to obtain an *ionosphere free* phase path, L_F.

A combination similar to (1.10) can be applied to the excess phases obtaining the ionosphere corrected excess phase, ΔL_C, or ideally the ionosphere free excess phase, ΔL_F. The ionosphere free excess phase (or phase path) is what we would measure had there been no ionosphere at all. Theoretically the ionosphere free excess phase is always positive and at the high altitude end it becomes very small. For rays with tangent points at ~ 60 km it is a few centimeter and at ~ 80 km it is about 1 mm—less than the noise level seen on GPS/MET data.

After deriving the excess Doppler, $\Delta\dot{L}_\mathrm{F}$, the bending angle as a function of the impact parameter is found from the geometry of the occultation and the velocities of the satellites (Figure 1.5). For each data sample, the impact parameter, a—assumed the same for both the incident and the emergent ray—can be found by solving the following equation [*Melbourne et al.*, 1994] (see Figure 1.5 for definitions of symbols):

$$\Delta\dot{L}_\mathrm{F} + \dot{R}_\mathrm{LG} - \left(|\dot{\bar{R}}_\mathrm{L}|\cos\varphi(a) - |\dot{\bar{R}}_\mathrm{G}|\cos\chi(a)\right) = 0 \tag{1.11}$$

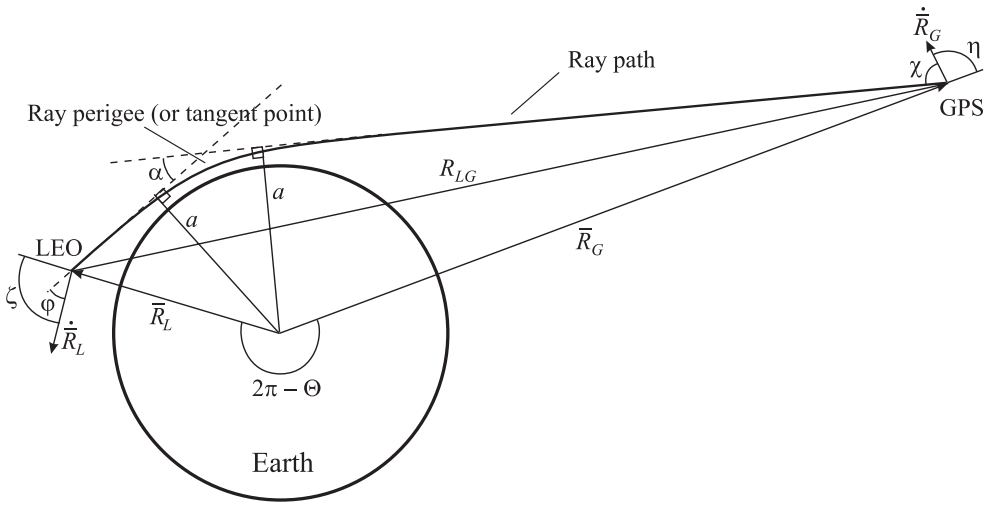

Figure 1.5 The occultation geometry, defining various parameters used in the text. $\dot{\bar{R}}_{\mathrm{L}}$ and $\dot{\bar{R}}_{\mathrm{G}}$ are the projections of the satellite velocities into the occultation plane, defined by the position of the satellites and the center of refraction (adapted from [*Melbourne et al.*, 1994]).

with

$$\varphi(a) = \zeta - \arcsin\left(\frac{a}{|\bar{R}_{\mathrm{L}}|}\right),$$

$$\chi(a) = (\pi - \eta) - \arcsin\left(\frac{a}{|\bar{R}_{\mathrm{G}}|}\right).$$

The bending angle, α, for that a, is then given by

$$\alpha = \Theta - \arccos\left(\frac{a}{|\bar{R}_{\mathrm{L}}|}\right) - \arccos\left(\frac{a}{|\bar{R}_{\mathrm{G}}|}\right). \tag{1.12}$$

In these equations, the refractivity at the satellites has been neglected[3].

Having the relationship $\alpha(a)$ for all samples, equation (1.9) directly gives the refractive index at the tangent point altitudes. At this point in the processing it becomes a practical problem to apply equation (1.9) since our measurements of bending angles does not reach to infinity, and even at high altitudes, where we do have measurements, they may be useless due to random errors and ionosphere residuals. This problem is dealt with by extrapolating bending angles or using statistical optimization techniques where a model bending angle profile gradually replaces the data profile above some specified altitude depending on the noise level [*Sokolovskiy and Hunt*, 1996; *Hocke*, 1997; *Gorbunov and Gurvich*, 1998a].

Proceeding to derive dry pressure[4] and dry temperature, we assume ideal gas behavior, from which it follows that the dry air density, ρ, is proportional to the dry air

[3]Using the ionosphere free phase and thus obtaining neutral atmospheric bending angles, this is a very good approximation. However, the same equations can in principle be applied to find the real bending angles for each of the two frequencies, by inserting L_i $(i = 1, 2)$ instead of L_{F} in (1.11). In that case, depending on the orbit altitude and the ionospheric conditions, the approximation of neglecting the refractivity at the LEO satellite is less accurate, and has been discussed in some detail by *Hajj and Romans* [1998].

[4]Here the *dry pressure* is not generally the same as the partial pressure of dry air, p_{d}, as defined in Section 1.3, but is merely the analogue to the *dry temperature*. Only under dry air conditions, the *dry pressure* and the (partial) pressure of dry air is the same.

refractivity (equation 1.6). From the dry air density profile, pressure, p, as a function of altitude, h, is generated by applying the hydrostatic equilibrium assumption:

$$p(h) = \int_{R+h}^{\infty} \rho(r) g(r) dr, \tag{1.13}$$

where R is the radial distance from the center of refraction to the Earth's surface at the tangent point location, and $g(r)$ is the gravitational acceleration profile at this location. Finally the equation of state is applied once again to obtain temperature:

$$T(h) = \frac{p(h)}{R_{\mathrm{d}} \rho(h)}, \tag{1.14}$$

R_{d} being the gas constant for dry air.

The temperature obtained in this way is a very good estimate of the real temperature in regions where the water vapor term (second term of equation (1.5)) has only little influence on the total refractivity. This is not generally the case in tropical regions at tropospheric heights. Then the dry temperature will underestimate the real temperature. As a consequence, in moist regions the water vapor pressure may be found if auxiliary information of the real temperature is available. From (1.5) it follows (disregarding the ionosphere term which is assumed eliminated) that

$$p_{\mathrm{w}} = T^2 \frac{N - k_1 p/T}{k_3}. \tag{1.15}$$

Here T denotes the auxiliary temperature while N is the refractivity measured from the occultation data. The total pressure, p, may be obtained either from auxiliary sources also, or the hydrostatic equation may be invoked to get the relation between temperature, pressure and moisture. This latter approach becomes an iterative procedure, and methods for water vapor retrieval using such schemes has been elaborated by *Gorbunov et al.* [1996b] and *O'Sullivan et al.* [1999].

In principle, if occultation data are taken at altitudes up to well above the F-layer peak, the Abel transform solution can be applied to obtain an ionosphere refractive index profile, from which the electron density may easily be derived [*Hajj and Romans*, 1998]. However, since it takes a much longer time ($\sim$ 10 minutes) to collect the occultation data at all heights in the ionosphere and because the ionosphere may have large horizontal variations over the range of the occultation, the method, assuming spherical symmetry, may give spurious results like negative electron densities [*Hardy et al.*, 1994; *Høeg et al.*, 1998]. Therefore, the ionosphere occultation data cannot in general be used to obtain very precise vertical electron density profiles without using constraints related to a priori knowledge—better than the spherical symmetry assumption—about the ionosphere electron density distribution.

In this thesis we shall concentrate on the retrieval scheme going from excess phases to dry temperature profiles. Thus, water vapor retrieval in the troposphere, needing auxiliary information, and electron density retrieval in the ionosphere, also requiring auxiliary information of some kind to generally obtain reliable results, are not considered in detail.

Chapter 2

Error Sources and Resolution

All measurements, and derived parameters from a set of measurements, are subject to errors. This, of course, is also the case for the occultation measurements and the derivation of the atmospheric parameters. When presenting results they should always be accompanied by an error assessment. Such an assessment is based on the knowledge of the measurement errors and the way these errors propagate through the processing chain. In addition, retrieval errors, due to approximations and insufficient knowledge from the data, are introduced during the processing.

Another important issue is the spatial resolution of the measurements. Along with the result and the accuracy there should be some information about the vertical and horizontal resolution. If occultation data are to be assimilated into NWP models, the vertical and horizontal error correlations will also be of relevance.

2.1 Double Differencing

Equations (1.1a) and (1.1b) are idealistic representations of the phase observables. More accurately a GPS phase observable can be written as

$$L = \int \mu ds + \Delta\beta - B \tag{2.1}$$

where $\Delta\beta$ is a clock error due to instabilities and drifts of the frequency oscillators in the GPS and LEO receivers, and B is the phase ambiguity bias being an integer number of wavelengths. Embedded in the clock error is also the intentional modulation of the GPS satellite clock—named *Selective Availability* (SA)—which has been incorporated in the GPS for military security reasons. As mentioned, it is not necessary to know the ambiguity bias on the GPS–LEO link since it is a constant during the whole occultation (disregarding cycle-slips) and we only need the derivative of the phase to calculate the bending angles. The clock error and the SA, however, has to be removed. This can be done by various differencing techniques [*Hardy et al.*, 1994; *Kursinski et al.*, 1997], of which double differencing is the most effective and is the one used in the GPS/MET experiment [*Rocken et al.*, 1997]. Double differencing involves one more GPS satellite besides the occulting one, as well as a ground station. The LEO satellite has to be able to see the two GPS satellites simultaneously, while these are able to see the ground station. The technique then eliminates the LEO and GPS clock errors and the SA. The drawback of using the double differencing technique is random and local multipath error magnification, as well as the introduction of tropospherically induced errors

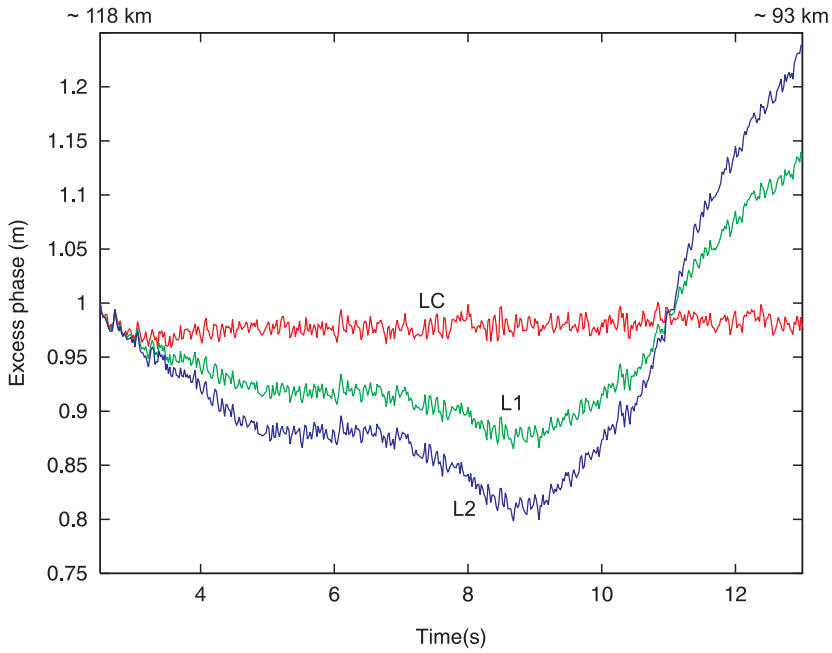

Figure 2.1 Measured excess phases as a function of time for GPS/MET occultation no. 39, day 125, 1995 (UCAR data). Only the first part of the setting occultation, corresponding to heights above $\sim$ 93 km (13 s), is shown. The absolute level on the ordinate is off due to the arbitrary setting of the first point in the dataset (equals 1 m for UCAR data).

on the GPS–ground links [*Hardy et al.*, 1994; *Kursinski et al.*, 1997]. The Russian GLONASS does not have something similar to SA, and it is likely that such a thing will never be implemented [*Seeber*, 1993]. Without the SA it can be advantageous to not difference, depending on the magnitude of the clock error relative to the amplification and introduction of other errors in the double differencing procedure [*Kursinski et al.*, 1997].

2.2 Random Errors

Generally, measurement errors can be classified as either random (statistical), systematic or illegitimate [*Mathiesen*, 1997]. Random errors in the occultation experiment include thermal noise in the LEO and ground receivers as well as—depending on the differencing technique—clock instabilities or tropospheric noise introduced on ground differencing links [*Hardy et al.*, 1994; *Kursinski et al.*, 1997]. For the GPS occultations, random errors are also introduced depending on whether *Anti Spoofing* (AS) is turned on or off. Anti Spoofing is an intentional encryption of the GPS signal code used—like the SA—to degrade the accuracy for non-authorized users. When AS is off, the present receiver used in the GPS/MET experiment gives phase errors less than one millimeter, the errors being uncorrelated between successive samples [*Kursinski et al.*, 1997]. When AS is on, the L2 phase noise increases substantially for the current GPS/MET receiver [*Hajj et al.*, 1995; *Rocken et al.*, 1997]. For the GPS/MET experiment the AS was turned off in periods named "prime-time", where also the MicroLab-1 satellite was oriented so that GPS satellites were occulted in the aft or anti velocity direction toward Earth's limb [*Rocken et al.*, 1997]. All data used in this thesis are from such prime-time periods.

Thermal noise depends on signal strength, background radiation, and receiver hardware. Clock instabilities and tropospheric propagation noise on the GPS–ground links gives only small errors [*Hardy et al.*, 1994; *Kursinski et al.*, 1997], but additionally, a relatively large noise, apparently uncorrelated between successive data samples, but highly correlated between the L1 and L2 signals, is seen on the GPS/MET data. Figure 2.1 shows such an example where only the uppermost part of an occultation, corresponding to ray path tangent heights between 118 km and 93 km, is shown. L1 and L2 denote the phase measurements for each of the two frequencies, while LC denotes the ionosphere corrected phase path using equation (1.10). The L1/L2 correlation is very clear in this example and the noise seems to be of the order of 1 cm. Most occultations have less noise than this, and often the L1/L2 correlation is less conspicuous. The source of this L1/L2 correlated error is not known for sure, but it may be due to residual errors from the LEO satellite clock calibration in the double differencing scheme (E. Robert Kursinski, personal communication, 1998). All of these errors are considered random and they are collectively referred to as *measurement noise*. An analysis of how measurement noise propagates through the processing chain from excess phase to dry temperature is presented in Chapter 3.

2.3 Systematic Errors

Systematic errors in the measurements—assuming that clocks and SA has been calibrated by the double differencing technique—are due to local multi-path and inaccuracies in orbit ephemerides. These errors are highly correlated over the course of an observation, and can, in principle—having precise knowledge about them—be reduced to below significance.

Local multi-path occurs when part of the signal coming into the receiving antenna is scattered off from structures in the vicinity of the antenna. The effect on the occultation phase path due to local multi-path at the ground station—via the double differencing scheme—was simulated by *Hardy et al.* [1994] as a 1 mm sine curve with a period of 300 seconds. Local multi-path at the LEO was simulated as a shorter period oscillation ($\sim$ 40 s) varying in amplitude, and being of order 1 mm. *Kursinski et al.* [1997] simulated LEO local multi-path by a low frequency spectrum ranging ± 0.01 Hz and with an uniform RMS phase error of 10 mm, representative of expected values for broad beam antennas. They found that such an error may be the limiting error in retrieved atmospheric parameters in the stratosphere under otherwise excellent conditions. Local multi-path may be reduced by using more directional antennas, or if the reflecting structures near the antenna is known, the multi-path signal may be modeled and then removed or minimized in the data processing.

Position errors—primarily in the radial direction—mostly affect the determination of the ray path tangent altitude, while velocity errors—primarily the component along the ray path—affects the measured Doppler shift [*Kursinski et al.*, 1997]. For the GPS/MET, comparisons between different orbit determination methods, indicate that LEO receiver positions can be estimated to within about 1 m, while velocity accuracies are of the order of 1 mm/s or less [*Bertiger et al.*, 1996; *Schreiner*, 1996; *Lemoine et al.*, 1996]. However, the precision—based on internal orbit overlap measurements—has been measured to only about 5 cm and 0.05 mm/s for LEO receiver radial positions and along ray velocities, respectively [*Bertiger and Wu*, 1996]. The determination of

the GPS ephemerides can be done to the same order of magnitudes. In a simulation study, *Kirchengast* [1998] investigated the effects of different errors of the ephemerides and found that radial position errors of up to 50 m have no significant effect on dry temperature retrievals. On the other hand, along ray velocity errors of, e.g., 1 mm/s resulted in an error in temperature of 1 K at 18 km and about 5 K at 30 km. For a velocity error of 0.05 mm/s he found that the temperature error stayed within 1 K up to about 45 km altitude. Similar results have been obtained by *Høeg et al.* [1998] using the same simulation software. *Kursinski et al.* [1997] also estimated the effect on retrievals of a 0.05 mm/s velocity error and found fractional errors of refractivity, pressure, and temperature less than 0.1% below 40 km.

Relativistic effects due to gravitational potential differences and the satellite velocities should be eliminated to retrieve bending angles to better than 20 % accuracy above 30 km altitude [*Vorob'ev and Krasil'nikova*, 1994; *Kursinski*, 1997]. Having the above mentioned accuracy of the satellite ephemerides, such a correction is possible to a very high degree so that residual relativistic effects can be considered negligible.

Systematic errors are also introduced via the retrieval procedure. Besides measurement noise, different retrieval errors are the ones generally having the largest impact on the atmospheric parameters obtained. The most significant retrieval errors are: ionosphere calibration errors, upper altitude boundary errors, errors due to the assumption of spherical symmetry not being accurate, and errors induced by atmospheric multipath and diffraction if not properly corrected for. To this comes other minor retrieval errors like refractivity constant uncertainties and non-ideal gas behavior. These latter errors does not contribute significantly in comparison with the other retrieval errors just mentioned [*Kursinski et al.*, 1997].

The temperature/water vapor ambiguity is not really an error source when speaking of refractivity or dry temperature. It is only when the dry temperature is interpreted as the real temperature that the temperature/water vapor ambiguity can be considered a retrieval error. However, the water vapor in the atmosphere indirectly causes errors in retrieved dry temperature through horizontal variations, and through multi-path and diffraction effects if not properly removed. Atmospheric multi-path and diffraction effects *can* be removed, or at least mitigated, using the diffraction correction/back-propagation method [*Karayel and Hinson*, 1997; *Gorbunov and Gurvich*, 1998b].

Ionosphere calibration errors and errors due to the assumption of spherical symmetry not being accurate are dealt with in more detail in Chapter 4.

2.4 Illegitimate Errors

An obvious example of illegitimate measurement errors are the errors produced by cycle-slips in the phase measurements. In the occultation experiment the sampling rate is so high that cycle-slips often result in illegitimate errors over the range of several samples, and sometimes in the troposphere it results in permanent loss of track.

An illustrative example of a cycle-slip in GPS/MET data is shown in Figure 2.2. In this example the cycle-slip is happening at the bottom of the ionosphere at about 7–8 s into the occultation, corresponding to a ray tangent altitude of about 80–77 km. The cycle-slip is evidently happening on the L2 phase path, and carried on to the ionosphere corrected phase path, LC. There is no cycle-slip on L1. To judge from the L1 and L2 signatures, this could very well be a vertical region of atmospheric multi-

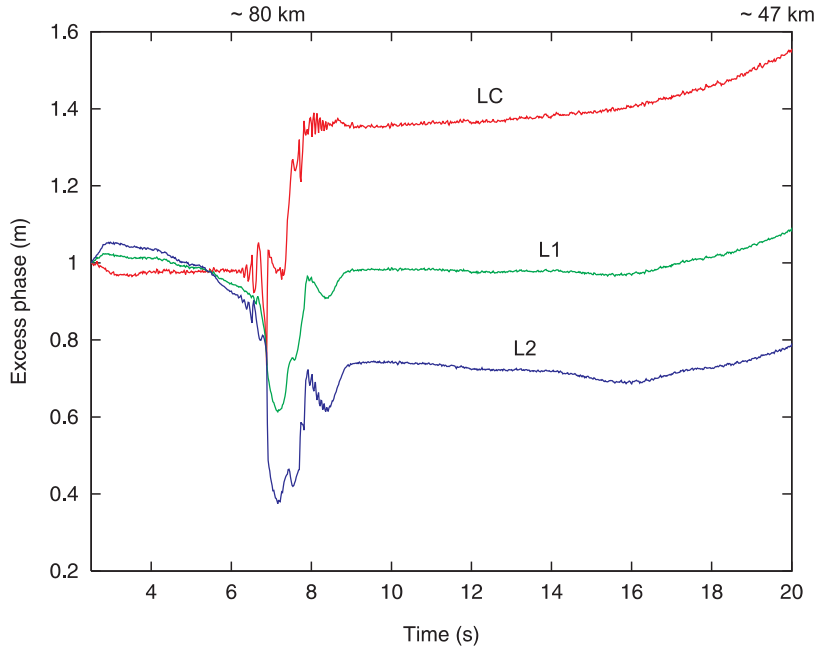

Figure 2.2 Measured excess phases as a function of time for GPS/MET occultation no. 6, day 124, 1995 (UCAR data). Only the first part of the setting occultation, corresponding to heights above $\sim$ 47 km (20 s) is shown. The absolute level on the ordinate is off due to the arbitrary setting of the first point in the dataset (equals 1 m for UCAR data).

path propagation, where the receiver is measuring the combined signal from three or more propagation paths. The cycle-slip on L2 is then triggered by the rapid phase variations happening in this region caused by sharp vertical electron density gradients at the bottom of the ionosphere. For multiple paths to occur it requires some very strong vertical gradients, and since the electron density itself is quite small at these altitudes it is a bit surprising to see such a strong signature. A sporadic-E layer could perhaps be the origin of such gradients, but usually sporadic-E layers are reported at heights above 100 km. However, the judgment that these really are multi-path signatures, is based also on the amplitude signatures (not shown) and on the fact that similar signatures are seen on the results of numerical simulations of tropospheric multi-path propagation published by *Gorbunov and Gurvich* [1998a], as well as on the results of multi-path ray tracing simulations (though also concentrating on the troposphere region) performed by the author.

Although cycle-slips are relatively rare in the upper part of the occultation, they are indeed expected to occur more frequently in the lower troposphere, especially in tropical regions where atmospheric multi-path is caused by strong vertical gradients in the water vapor distribution [*Gorbunov and Gurvich*, 1998b]. The GPS receiver used in the proof-of-concept GPS/MET experiment, has problems tracking the signal in such regions because of the strong oscillations and low magnitude of the signal. *Gorbunov and Gurvich* [1998b] finds only a few GPS/MET occultations where the low-tropospheric signal looks reasonable.

Cycle-slips and large sections of the data where tracking has failed should be removed, having some criteria for their removal. This subject has been dealt with in detail by *Steiner et al.* [1999] correcting for "data runaways" by a 3-sigma level rejection criteria

and using an extrapolation method of L1–L2 Doppler shifts below 12.5 km to obtain more reliable L2 data (based on the L1 and the extrapolated L1–L2 data) at these altitudes.

2.5 Vertical Resolution

The vertical resolution is limited by measurement noise, diffraction, and horizontal atmospheric inhomogeneities [*Rocken et al.*, 1997]. In regions in the lower troposphere atmospheric multi-path propagation may occur which also will limit the accuracy and resolution of the retrieved atmospheric profiles.

The limitation by diffraction is determined by the diameter of the first Fresnel zone [*Melbourne et al.*, 1994; *Kursinski et al.*, 1997] given by

$$z_{\mathrm{F}} = 2\sqrt{\frac{\lambda D}{1 - D\frac{d\alpha}{dh}}}, \tag{2.2}$$

where λ is the wavelength of the signal, D is the *reduced distance* given by $(1/D_{\mathrm{L}} + 1/D_{\mathrm{G}})^{-1}$, where D_{L} and D_{G} are the distances from the LEO and the GPS satellite, respectively, to the tangent point. For the GPS/MET, z_{F} is about 1.5 km in the stratosphere decreasing to about 0.5 km in the lower troposphere.

Fresnel diffraction theory and back-propagation of the signal to a region nearer the tangent point can reduce the Fresnel diameter and thereby the vertical resolution limit [*Melbourne et al.*, 1994; *Karayel and Hinson*, 1997; *Gorbunov and Gurvich*, 1998b]. At the same time such methods corrects, or at least mitigates, the effects of multi-path propagation. *Mortensen et al.* [1999] have shown that theoretically, back-propagation can reduce the vertical resolution limit to 100–150 m.

2.6 Horizontal Resolution

The horizontal resolution is very difficult to asses in the occultation experiment since the measurement is an integrated effect over the entire ray path between the satellites. However, most of the bending occurs over approximately 700 km of the path, centered at the tangent point [*Høeg et al.*, 1996]. The subject has been studied in more detail by *Ahmad and Tyler* [1998a] finding that the horizontal extent of significant contributions is of the order $2\sqrt{4.6 r_0 H_{\mathrm{s}}}$ centered at the tangent point, where H_{s} is the atmospheric scale height. Putting in numbers ($r_0 = 6400$ km, $H_{\mathrm{s}} = 8$ km) gives ~ 970 km.

Taking into account the sphericity of the atmosphere, the first Fresnel diameter, z_{F}, which limit the vertical resolution can be used to define a horizontal resolution at the tangent point as

$$D_{\mathrm{F}} = 2\sqrt{2 r_0 z_{\mathrm{F}}}. \tag{2.3}$$

If $z_{\mathrm{F}} \ll r_0$, D_{F} is approximately the horizontal width of a spherical shell having the thickness equal to the first Fresnel diameter. For $z_{\mathrm{F}} = 1$ km we get $D_{\mathrm{F}} \approx 220$ km.

During the occultation the tangent points are drifting horizontally due to the satellite motion, giving different tangent point locations at different heights. This horizontal drift may become as large as 300 km during the lowest 60 km of ray path descend [*Kursinski et al.*, 1997].

Chapter 3

Random Error Propagation

In this chapter the random error propagation from excess phase to dry temperature is investigated. It is assumed that the measurements are free of systematic errors and that the measurement noise can be regarded as statistically independent from sample to sample. Furthermore it is assumed that the errors are random and Gaussian-distributed. Figure 2.1 indicates that this is a good assumption at least in the upper part of the excess phase-time series. A Fourier analysis of the "flat" part of the LC curve in a few examples showed that the noise to a good approximation can be regarded as being "white".

The following error propagation analysis takes the starting point in the ionosphere-free excess phase, i.e., assuming that the ionosphere contribution has been eliminated. Correction of the ionosphere, using the dual-frequency combination (1.10) (or a similar combination using bending angles (see Section 4.1)), will amplify uncorrelated errors on the L1 and L2 phases (bending angles) by a factor of about 3 on the resulting LC phase (bending angle). As already shown (Figure 2.1) GPS/MET data are not necessarily uncorrelated between L1 and L2 phases, and for that example there is almost no amplification. To simplify things, such an amplification factor is therefore disregarded, but can in principle always be multiplied at the end.

Generally, error covariance matrices of bending angles, refractivity, or temperature are important for assimilation of the data into NWP models (depending on what to be assimilated). However, one of the most influent error sources in the lower atmosphere, namely the effects of horizontal gradients [*Kursinski et al.*, 1997], will invalidate the vertical correlations as found by the error covariance analysis. It is not clear how to take this effect into account, except maybe by numerical simulations. For simplicity we shall only look at the error propagation and the resulting vertical correlations arising in a spherical symmetric atmosphere. The effects of horizontal gradients on the temperature profiles are investigated in more detail in Section 4.2.

Another source of error in the lower atmosphere, if not corrected for, is diffraction effects and atmospheric multi-path propagation. As already mentioned it is possible, at least theoretically, to eliminate or mitigate these effects by applying e.g., the diffraction correction/back-propagation method [*Karayel and Hinson*, 1997; *Gorbunov and Gurvich*, 1998b]. However, in the following error analysis this is not considered, and we shall concentrate on the approach normally used in the geometrical optics approximation.

3.1 Error Covariance Analysis

Error covariance analyses have earlier been carried out for the occultation measurements of temperature profiles of Mars and Venus [*Stewart and Hogan*, 1973; *Lipa and Tyler*, 1979]. Recently it has been done for the GPS/MET experiment also [*Feng and Herman*, 1998]. However, the work of *Stewart and Hogan* [1973] did not take the refractive bending into account, which is necessary in the lower part of the Earth's atmosphere. The works of *Lipa and Tyler* [1979] and *Feng and Herman* [1998] treat the impact parameter as a dependent variable when propagating errors through the Abel transform, whereas it would be more appropriate to treat it as an independent variable and thus transform the errors obtained in the impact parameter to errors on the bending angle. This idea is followed here and is to be elaborated in the subsections below.

To shortly summarize the principles of error propagation using covariance analysis, let $\mathbf{x} = (x_1, x_2, \ldots, x_n)^{\mathrm{T}}$ (with ^{T} denoting the matrix transpose) be a set of measurements with "true" mean values $\bar{x}_i$ $(i = 1, 2, \ldots, n)$ and errors $\delta x_i = x_i - \bar{x}_i$. The error covariance matrix is then given by

$$\mathbf{C}_x = \begin{pmatrix} X_{11} & X_{12} & \cdots & X_{1n} \\ X_{21} & & \cdots & X_{2n} \\ \vdots & & & \\ X_{n1} & & \cdots & X_{nn} \end{pmatrix}, \tag{3.1}$$

where $X_{ij} = \langle \delta x_i \delta x_j \rangle$ is the error covariance between the i'th and the j'th measurement, and $\langle\rangle$ denotes the statistical mean. We may also write (3.1) as

$$\mathbf{C}_x = \langle \delta\mathbf{x}\, \delta\mathbf{x}^{\mathrm{T}} \rangle. \tag{3.2}$$

If a derived set of measurements, $\mathbf{y}(\mathbf{x})$, are connected to $\mathbf{x}$ via a linear relation

$$\mathbf{y} = \mathbf{A}\mathbf{x}, \tag{3.3}$$

and if the independent variable connected to the i's of the measurements (e.g., time) is the same for $\mathbf{y}$ as for $\mathbf{x}$, then

$$\delta\mathbf{y} = \mathbf{A}'\delta\mathbf{x} \tag{3.4}$$

with $\mathbf{A}' = \mathbf{A}$. If the relation is not linear $\mathbf{A}'$ is different from $\mathbf{A}$. Then, using Taylor expansion around the mean, $\bar{\mathbf{x}}$, and on condition that $\|\delta\mathbf{x}\| \ll \|\bar{\mathbf{x}}\|$, (3.4) is valid to first order with

$$\mathbf{A}' = \begin{pmatrix} \partial y_1/\partial x_1 & \partial y_1/\partial x_2 & \cdots & \partial y_1/\partial x_n \\ \partial y_2/\partial x_1 & & \cdots & \partial y_2/\partial x_n \\ \vdots & & & \\ \partial y_n/\partial x_1 & & \cdots & \partial y_n/\partial x_n \end{pmatrix}_{\mathbf{x}=\bar{\mathbf{x}}}. \tag{3.5}$$

However, if the independent variable changes non-linearly in going from $\mathbf{x}$ to $\mathbf{y}$ (e.g., from the time domain to the impact parameter domain), as will be shown in some of the following subsections, $\mathbf{A}'$ will have to be derived by other means. In any case, the error covariance matrix for $\mathbf{y}$, having matrix elements $Y_{ij} = \langle \delta y_i \delta y_j \rangle$, is given by

$$\begin{aligned} \mathbf{C}_y &= \langle \delta\mathbf{y}\, \delta\mathbf{y}^{\mathrm{T}} \rangle \\ &= \mathbf{A}'\mathbf{C}_x\mathbf{A}'^{\mathrm{T}}. \end{aligned} \tag{3.6}$$

From the error covariance matrix the standard deviation of measurement y_i is given by

$$\sigma_i = \sqrt{Y_{ii}}, \tag{3.7}$$

and the error correlation between measurements y_i and y_j is

$$c_{ij} = \frac{Y_{ij}}{\sigma_i \sigma_j}. \tag{3.8}$$

3.1.1 Excess Phase Filtering

The first step in the processing chain is a low pass filtering. High frequency noise, if not reduced, eventually results in large amplitude oscillations in retrieved temperature in the stratosphere and above. To obtain a solution of the temperature profile that are within 1–2 K at 30–40 km altitude, some kind of smoothing is necessary at the high altitude end. When no diffraction correction/back propagation is applied, data smoothing in the low altitude end should be performed to reduce diffraction effects and mitigate signatures resulting from atmospheric multi-path propagation.

Here we shall follow an approach suggested by *Feng and Herman* [1998], using conventional regularization (also termed constrained linear inversion) to smooth the data. This approach makes it particularly easy to calculate the resulting error covariance matrix of the smoothed excess phase data, given the error covariance of the unsmoothed data. Generally, a linear inverse problem with regularization may be formulated as minimizing

$$f_\lambda(\mathbf{x}) = \|\mathbf{A}\mathbf{x} - \mathbf{y}\|^2 + \lambda \|\mathbf{S}\mathbf{x}\|^2 \tag{3.9}$$

with respect to the unknown "model" vector $\mathbf{x}$ [e.g., *Twomey*, 1977]. In (3.9) $\mathbf{A}$ is a matrix representing the linear relationship between the "model" vector, $\mathbf{x}$, and the "data" vector, $\mathbf{y}$. The smoothing matrix, $\mathbf{S}$, is usually an n'th order difference operator, and λ is a regularization parameter. Minimizing (3.9) is formally equivalent to solve for $\mathbf{x}$, the matrix equation

$$(\mathbf{A}^{\mathrm{T}}\mathbf{A} + \lambda \mathbf{S}^{\mathrm{T}}\mathbf{S})\mathbf{x} = \mathbf{A}^{\mathrm{T}}\mathbf{y}. \tag{3.10}$$

In the special case where $\mathbf{A} = \mathbf{I}$ is the unity matrix of a dimension equal to the dimension of $\mathbf{y}$, the "model", $\mathbf{x}$, becomes a smoothed version of of the unsmoothed "data" $\mathbf{y}$. Now, let $\mathbf{y} = \mathbf{L}$ be our excess phase-time series[1] and $\mathbf{x} = \tilde{\mathbf{L}}$ the desired smoothed version of the excess phase data. In this case (3.10) leads to the solution

$$\tilde{\mathbf{L}} = (\mathbf{I} + \lambda \mathbf{S}^{\mathrm{T}}\mathbf{S})^{-1}\mathbf{L}. \tag{3.11}$$

The matrix $\mathbf{S}$ is here chosen to be a third difference operator, i.e.,

$$\mathbf{S} = \begin{pmatrix} -1 & 3 & -3 & 1 & 0 & 0 & \cdots \\ 0 & -1 & 3 & -3 & 1 & 0 & \cdots \\ & & & \ddots & \ddots & & \\ & \cdots & 0 & -1 & 3 & -3 & 1 \end{pmatrix}, \tag{3.12}$$

[1]For convenience we shall here denote the *excess phase* by the symbol L, although in Section 1.5, L was used to denote the *phase path* (or optical path length). In this section only the excess phase is discussed, giving no cause for confusion.

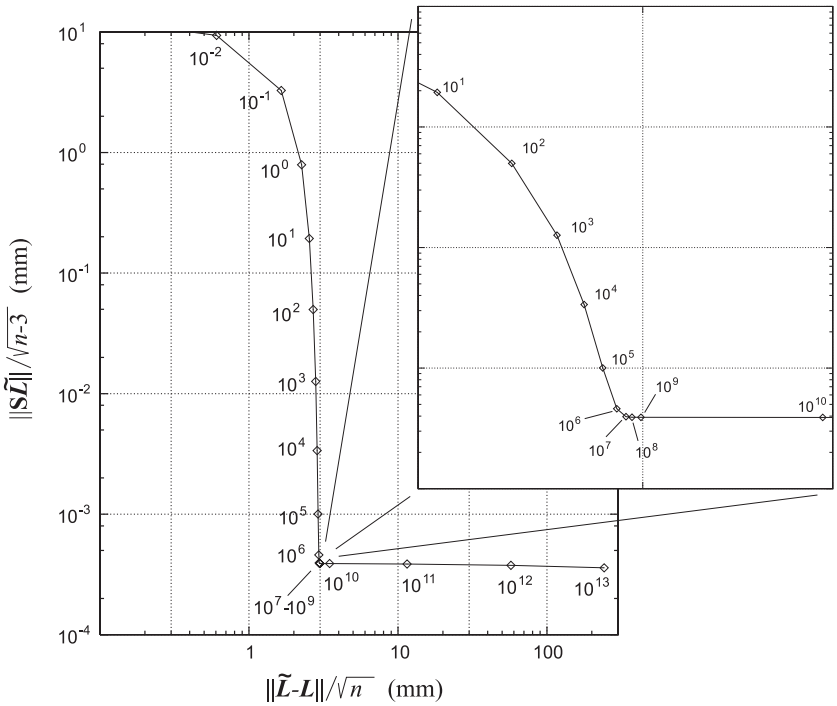

Figure 3.1 The L-curve for 50 Hz excess phase data contaminated with random, Gaussian-distributed noise with a standard deviation $\sigma_L = 3$ mm. Numbers by the curve refer to the value of λ. The inset shows the L-curve corner in greater detail.

an $(n-3) \times n$ matrix, where n is the dimension of $\mathbf{L}$, i.e. the number of data points. If $\lambda = 0$, then $\tilde{\mathbf{L}} = \mathbf{L}$, meaning no smoothing at all. On the other hand, as $\lambda \to \infty$ the second term in (3.9) dominates and the smoothed solution will approach that quadratic which gives the best fit to the unsmoothed data (probably not a very good fit). Thus, λ controls the degree of smoothing and it should not be too small, neither should it be too large. For a proper value of λ, the solution (3.11) is in some sense a solution that fits the original data well, and at the same time minimizes the sum of the third derivatives. The regularization parameter determines the relative weighting between these two quests.

Feng and Herman [1998] used a more general expression allowing for different degrees of smoothing in different regions of the data set. This might be useful because the refractivity at high altitudes decreases nearly exponentially—and so does the relative accuracy—and a lower standard deviation may be preferable at the expense of a coarser vertical resolution. In the lower part of the atmosphere the signal is subject to large bending and defocusing resulting in a lower signal-to-noise ratio, and the original excess phase data will therefore have a larger error at these altitudes, in principle suggesting more smoothing there also. However, as we shall see, the lower signal-to-noise ratio due to the defocusing is not the limiting error source in the troposphere, and it may therefore be preferable to have less smoothing to achieve the highest vertical resolution possible [*Melbourne et al.*, 1994].

Here we shall keep it simple, and apply a constant value of λ to the whole data set. In fact, for a particular data set, one may try to find an optimum value of λ based on the so-called L-curve [*Hansen*, 1998]. To demonstrate, the L-curve for a simulated excess phase data set containing $n = 3318$ samples (50 Hz), was constructed. The excess

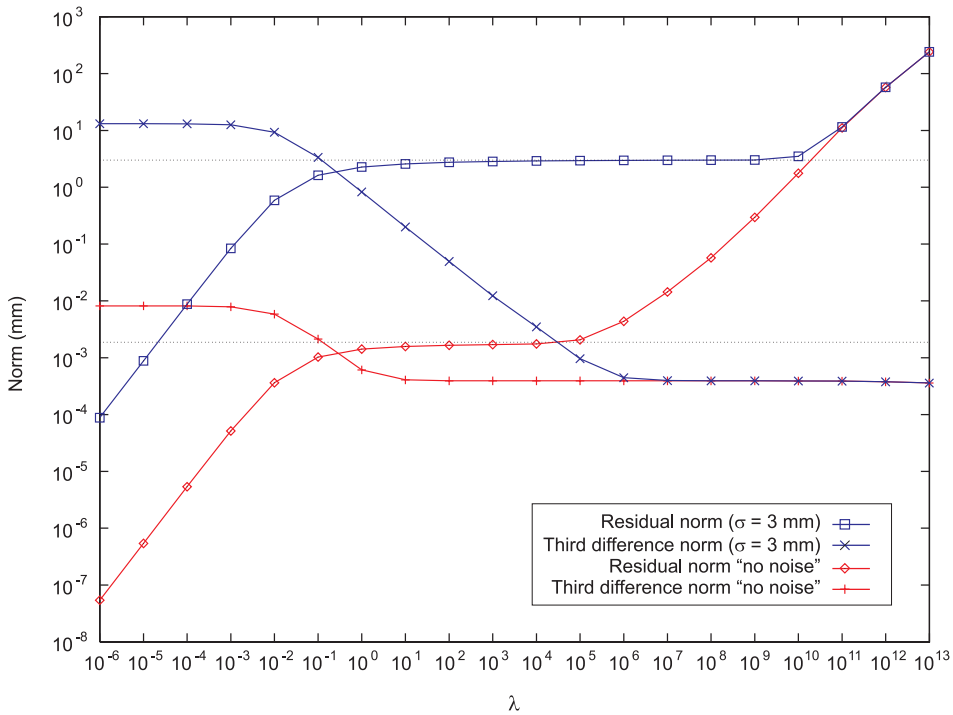

Figure 3.2 The residual norm and the third difference norm against λ for the case of $\sigma_L = 3$ mm, and the case of "no noise".

phase data were obtained using high accuracy ray-tracing through a smooth 1D model (independent of latitude and longitude) of the neutral atmosphere. Random, Gaussian-distributed noise with a standard deviation of 3 mm was then added to the synthetic excess phase data, and (3.11) was solved for different values of λ ranging 10^{-6}–10^{13}. Figure 3.1 displays the mean of the *third difference norm*, $\|\mathbf{S}\tilde{\mathbf{L}}\|/\sqrt{n-3}$, against the mean of the *residual norm*, $\|\tilde{\mathbf{L}} - \mathbf{L}\|/\sqrt{n}$, on a *log-log* scale.

On the vertical part of the L-curve increasing values of λ give smoother solutions while the residual remains less than the standard deviation (3 mm). The horizontal part of the L-curve corresponds to over-smoothing, since here the residual exceeds the standard deviation. Theoretically an optimum value of λ should be found at the corner of the L-curve [*Hansen*, 1998]. However, a wide range of λ-values lump together at the corner, and a unique corner value may be difficult to define. Looking at the inset of Figure 3.1 it becomes clear that a value close to 10^9 corresponds to the, in this case known, standard deviation. The exact value is not that important, however the value of λ here should not be chosen larger than $\sim 10^9$ to avoid over-smoothing. In general (for ill-posed inverse problems), the solution may become too smooth taking the optimum value and better results can often be obtained by taking a smaller value of λ [*Turchin and Nozik*, 1969]. Since we are here not even dealing with an ill-posed inverse problem, but merely try to reduce the high frequency noise in a data set, no real harm is done in choosing a smaller value of λ, we will just obtain a less smooth solution.

Another illustrative way to display the effect of different λ-values on the smoothed solution is to plot both norms ($\|\mathbf{S}\tilde{\mathbf{L}}\|/\sqrt{n-3}$ and $\|\tilde{\mathbf{L}} - \mathbf{L}\|/\sqrt{n}$) against λ. This is done in Figure 3.2, where also the case of "no noise" is plotted. For small values of λ ($< 10^{-2}$) the residual norm increases for increasing λ, while the third difference norm remains

almost constant at a high "noisy" value. At about $\lambda = 1$ (apparently independent of the noise level) the residual norm meets a plateau, corresponding to the standard deviation of the noise, and lasting several orders of magnitude until over-smoothing increases the residual norm again. The third difference norm for $\lambda > 10^{-2}$ falls to a plateau of about 0.5 μm, independent of the noise level. At very high values of λ (not shown) the third difference norm starts decreasing again. Figure 3.2 reveals that also the "no noise" case is contaminated with noise, although much less than the superimposed noise ($\sim$2 μm versus 3 mm). This small noise comes from numerical uncertainties in the computation of the synthetic phase data, and the curve gives, as a by-product, an indication of the ray-tracing precision (~ 2 μm).

It is obvious that the optimum value of λ depends on the noise level. For GPS/MET occultations the noise level in the high altitude end is of the order of a few millimeter, increasing at lower altitudes due to diffraction effects and a decreasing signal-to-noise ratio resulting from signal defocusing. In the following error propagation analysis we will assume, as a starting point, that the random error on the excess phase data is Gaussian-distributed, uncorrelated, and with a constant standard deviation of 3 mm. The error covariance matrix for the phase data is thus diagonal.

Handling matrices of dimension 3318$\times$3318 is very time consuming, even on a relatively fast work-station, and the analysis has therefore been carried out assuming 10 Hz data instead of 50 Hz data. Reducing the sampling rate from 50 Hz to 10 Hz (taking the mean of every 5 samples), obtaining a new uncorrelated time-series, allows for a reduction of the standard deviation by a factor of $\sqrt{5}$. Thus, the initial error covariance matrix for the phase data, $\mathbf{C}_L$, is a 663$\times$663 matrix with diagonal entries equal to 1.8 mm^2. The 663 samples of the phase data corresponds to altitudes from the Earth's surface and up to 109 km.

When the sample rate is reduced to 10 Hz the optimum value of λ is different, partly because we have reduced the standard deviation accordingly, and partly because the optimum value generally depends on the number of data samples. Figure 3.3 shows the L-curve corner for the 10 Hz data set ($n = 663$), and the optimum λ-value in this case is seen to be somewhere between 10^4 and 10^5. However, still it is no violation to choose a smaller value. For illustration, the following analysis is based on $\lambda = 10^4$ although this corresponds to a very coarse vertical resolution, and such a high degree of smoothing is not necessary in the lower part of the atmosphere. In the tropopause and the troposphere a value of 10 is more appropriate and is more concordant with the inherent limitation on the vertical resolution given by the first Fresnel diameter.

Introducing the linear filter operator,

$$\mathbf{F} = (\mathbf{I} + \lambda \mathbf{S}^{\mathrm{T}}\mathbf{S})^{-1} = \begin{pmatrix} F_{11} & F_{12} & \cdots & F_{1n} \\ F_{21} & & \cdots & F_{2n} \\ \vdots & & & \\ F_{n1} & & \cdots & F_{nn} \end{pmatrix}, \tag{3.13}$$

it follows directly from (3.11) that an error in the i'th data point of the smoothed solution, $\delta\tilde{L}_i$, may be written as

$$\delta\tilde{L}_i = \sum_{j=1}^{n} F_{ij}\delta L_j, \tag{3.14}$$

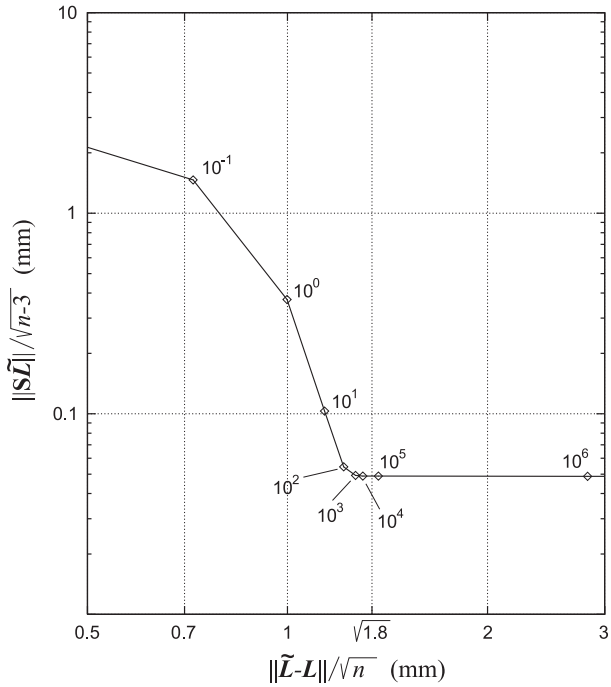

Figure 3.3 The corner of the L-curve for 10 Hz excess phase data contaminated with random, Gaussian-distributed noise with a standard deviation $\sigma_L = \sqrt{1.8}$ mm. The numbers by the curve refer to the value of the regularization parameter, λ.

where δL_j is the stochastic error at the j'th data point of the noisy excess phase-time series. Consequently the error covariance matrix for the smoothed data is given by

$$\mathbf{C}_{\tilde{L}} = \mathbf{F}\mathbf{C}_L\mathbf{F}^{\mathrm{T}}. \tag{3.15}$$

Figure 3.4 displays the correlation coefficient of one point in the smoothed data with the rest of the data set using the initial covariance matrix, $\mathbf{C}_L$, with parameters as described above ($n = 663$, $\sigma_L = \sqrt{1.8}$ mm ≈ 1.34 mm, $\lambda = 10^4$). The standard deviation of the smoothed data is equal to the square root of the diagonal elements of $\mathbf{C}_{\tilde{L}}$, found to be $\sigma_{\tilde{L}} \approx 0.33$ mm at most points except near the end points where it becomes larger.

The correlation scale of Figure 3.4 also gives an indication of the smearing or resolution, which corresponds to about 4 s. In the upper atmosphere, where only little bending occurs this maps into a vertical resolution of about 12 km depending on the descending rate of the tangent point, being about 3 km/s for a GPS/MET aft-looking occultation. In the troposphere the resolution becomes finer because of signal defocusing, and 4 s close to the surface corresponds to about 1.5 km. As mentioned above, this is much coarser than the first Fresnel diameter, and this high degree of smoothing is only used in this analysis for illustration. Using $\lambda = 10$ instead of $\lambda = 10^4$ for 10 Hz data, the vertical resolution improves by a factor of about 3, and the standard deviation becomes about 0.59 mm.

3.1.2 Excess Doppler

The second step is a numerical differentiation of the excess phase data to obtain the excess Doppler (having the dimension m/s). Here we shall use the three point finite

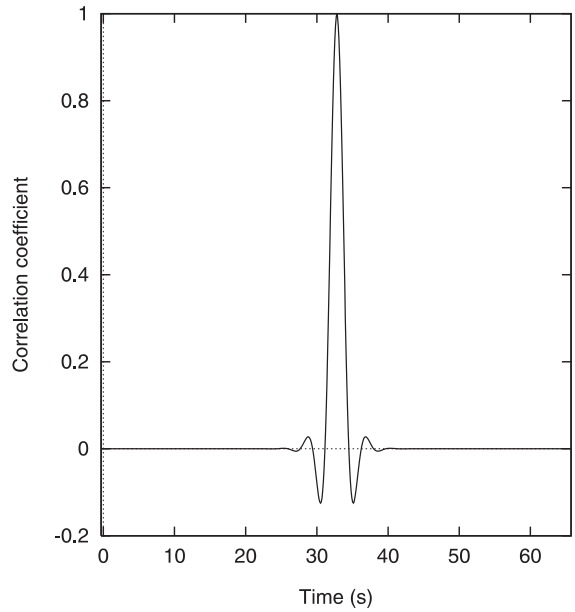

Figure 3.4 Excess phase correlation coefficient for a smoothed 10 Hz data set using $\lambda = 10^4$. Only the correlation between one point (where the correlation coefficient rises to one) and the remainder of the excess phase-time series is shown. A similar correlation exists around any other point in the data set, except at each end where end-point effects interfere.

difference scheme:

$$\dot{L}_i \approx \frac{\tilde{L}_{i+1} - \tilde{L}_{i-1}}{2\Delta t}, \tag{3.16}$$

where Δt is the sample time interval. Although such a scheme amplifies high frequency noise, there is no danger in using it here, since high frequency noise has already been eliminated, or greatly reduced, in the previous processing step. In fact, (3.16) is only a valid approximation as long as the discretization error, proportional to the third derivative of the excess phase, is small enough. This will generally not be the case in the high altitude end of the excess phase data (where the "true" excess phase becomes comparable to the noise level) if some kind of smoothing is not applied before or in concert with the Doppler calculation.

In matrix notation the derivative operator takes the form

$$\mathbf{D} = \frac{1}{2\Delta t} \begin{pmatrix} -2 & 2 & 0 & 0 & 0 & \cdots \\ -1 & 0 & 1 & 0 & 0 & \cdots \\ 0 & -1 & 0 & 1 & 0 & \cdots \\ & & \ddots & & \ddots & \\ & \cdots & 0 & -1 & 0 & 1 \\ & \cdots & 0 & 0 & -2 & 2 \end{pmatrix}, \tag{3.17}$$

where the two end-points has to be treated a little differently using an asymmetric two point difference scheme. The excess Doppler-time series is now given by

$$\dot{\mathbf{L}} = \mathbf{D}\tilde{\mathbf{L}}, \tag{3.18}$$

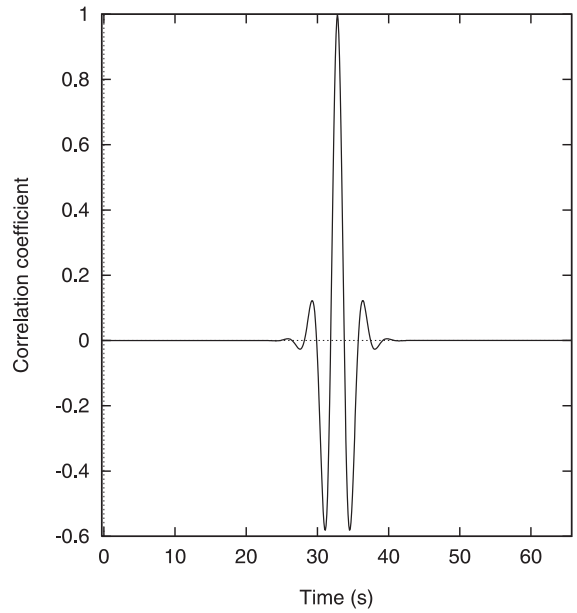

Figure 3.5 Excess Doppler correlation coefficient using the finite difference scheme (3.16). Only the correlation between one point (where the correlation coefficient rises to one) and the remainder of the Doppler-time series is shown. A similar correlation exists around any other point in the data set, except at each end where end-point effects interfere.

and since this is a linear operation, the error covariance matrix for the excess Doppler can be calculated as

$$\mathbf{C}_{\dot{L}} = \mathbf{D}\mathbf{C}_{\tilde{L}}\mathbf{D}^{\mathrm{T}}. \tag{3.19}$$

Figure 3.5 shows the correlation coefficient of one point in the excess Doppler data with the rest of the data set. We notice the enhancement of a negative correlation of near neighboring points due to the differentiation. The standard deviation of the excess Doppler extracted from the diagonal of the covariance matrix is almost constant at all points, $\sigma_{\dot{L}} \approx 0.39$ mm/s, except near the end points. If using $\lambda = 10$ instead of $\lambda = 10^4$ in the previous smoothing process, the standard deviation of the excess Doppler becomes about 2.1 mm/s. This relatively larger standard deviation (compared to the ratio between the σ_L values for $\lambda = 10$ vs $\lambda = 10^4$ in the previous subsection) is a consequence of the smaller error correlation between samples when using $\lambda = 10$.

3.1.3 Bending Angles

Calculation of bending angles from the excess Doppler as outlined in Section 1.5, involves an iterative process. Thus, the operation is mildly non-linear. However, assuming circular satellite orbits (which is a good assumption for the GPS satellites and for the MicroLab-1 satellite carrying the GPS/MET experiment) it is possible to come up with a simple linear relation between bending angle and excess Doppler which is accurate, also in the lower troposphere, to within 2% [*Melbourne et al.*, 1994]:

$$\alpha \approx -\left(\frac{da_0}{dt}\right)^{-1} \dot{L}, \tag{3.20}$$

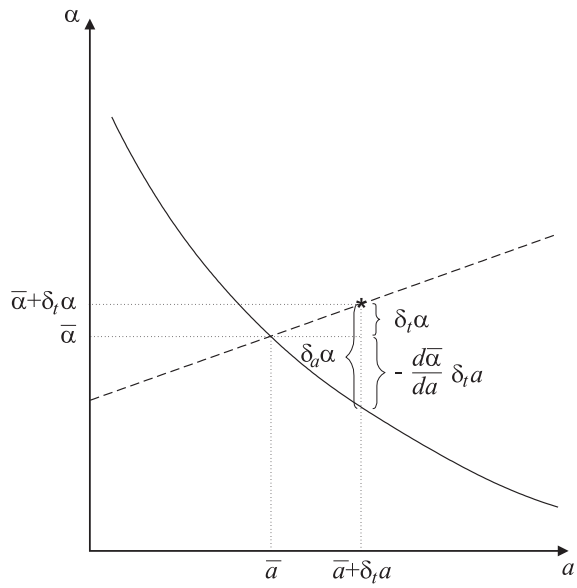

Figure 3.6 Illustration of the "true" atmospheric relation between bending angles and impact parameters (solid curve), and the relation for a measurement taken at a specific time where the bending angle and the impact parameter are connected via equation (3.22) (dashed curve). A given measurement, for a given time tag in the occultation, is denoted by the * on the dashed curve.

where a_0 is the *vacuum impact parameter*, i.e., the perpendicular distance from the center of refraction to the straight line connecting the GNSS- and LEO satellites. The rate, da_0/dt, which for a GPS/MET aft-looking occultation amounts to about 3 km/s, depends purely on the geometry of the occultation. Consequently an error in bending angle, resulting from an error in the excess Doppler, is given by

$$\delta_t \alpha \approx -\left(\frac{da_0}{dt}\right)^{-1} \delta_t \dot{L}. \tag{3.21}$$

The subscript, $_t$, is to emphasize that the errors are related to a specific time sample, which will be elaborated below. It has been assumed that there is no error in the determination of a_0 and its derivative, i.e., the satellite orbits are known with a very high accuracy.

Bending angle is normally expressed as a function of the impact parameter, a, not the time. In practice, a is also found from the excess Doppler using the formulas in Section 1.5. In the spherical symmetry assumption the bending angle and the impact parameter at a specific time (for given LEO- and GNSS positions) are connected via equation (1.12) repeated here:

$$\alpha = \Theta - \arccos\left(\frac{a}{R_{\mathrm{L}}}\right) - \arccos\left(\frac{a}{R_{\mathrm{G}}}\right). \tag{3.22}$$

Θ is the angle between the LEO- and GPS radial vectors having lengths R_{L} and R_{G}, respectively. So, not only the bending angles, but also the impact parameters will be contaminated with noise stemming originally from the phase data. We wish, however, to regard the impact parameter as an independent variable when later calculating the refractivity using the Abel transform (1.9). This can be done by "transmitting" the uncertainty in the impact parameter to an uncertainty in the bending angle using the

following argumentation and considering Figure 3.6. In Figure 3.6 the dashed curve corresponds to the relation (3.22), whereas the solid curve represents the "true" atmospheric bending angle as a function of the independent impact parameter. At a given time the calculated bending angle and connected impact parameter lies on the dashed curve. Let a measurement result in bending angle $\bar{\alpha}+\delta_t\alpha$ and impact parameter $\bar{a}+\delta_t a$, where the bar denotes the "true" mean values. The resulting error in the bending angle, $\delta_a\alpha$, when regarded as a function of the impact parameter, is then given by

$$\delta_a\alpha = \delta_t\alpha - \frac{d\bar{\alpha}}{da}\delta_t a, \tag{3.23}$$

where $d\bar{\alpha}/da$ is the derivative of the "true" curve. From equation (3.22) we get

$$\delta_t\alpha = \frac{1}{D}\delta_t a, \tag{3.24}$$

where

$$\frac{1}{D} = \frac{1}{\sqrt{R_{\mathrm{L}}^2 - \bar{a}^2}} + \frac{1}{\sqrt{R_{\mathrm{G}}^2 - \bar{a}^2}}. \tag{3.25}$$

The parameter D, will be referred to as the reduced distance, being about 2800 km for a LEO in a 750 km orbit, and varying only slightly during an occultation. Combining (3.21), (3.23), and (3.24) yields

$$\delta_a\alpha \approx -\left(\frac{da_0}{dt}\right)^{-1}\left(1 - D\frac{d\bar{\alpha}}{da}\right)\delta_t\dot{L}. \tag{3.26}$$

The additional factor on the right of (3.26) (compared to equation (3.21)) is the inverse of a defocusing factor [*Melbourne et al.*, 1994],

$$\zeta = \left(1 - D\frac{d\bar{\alpha}}{da}\right)^{-1}, \tag{3.27}$$

being only appreciably different from unity in the troposphere, where it will generally decrease downwards, to reach a value of the order of 0.1 close to the surface. In regions with sharp vertical refractivity gradients, primarily caused by water vapor fluctuations, the defocusing factor may vary irregularly with height in the lower troposphere [*Kursinski et al.*, 1997]. Since D is slowly varying we can write

$$\begin{aligned}\left(1 - D\frac{d\bar{\alpha}}{da}\right)\frac{d\bar{a}}{dt} &\approx \frac{d(\bar{a} - D\bar{\alpha})}{dt} \\ &\approx \frac{da_0}{dt},\end{aligned} \tag{3.28}$$

where, to obtain the second approximation, we have used (3.24) in the form $\bar{\alpha} - 0 \approx \frac{1}{D}(\bar{a} - a_0)$, which is valid to first order at any specific time sample. Thus, equation (3.26) can be reduced to

$$\delta_a\alpha \approx -\left(\frac{d\bar{a}}{dt}\right)^{-1}\delta_t\dot{L}. \tag{3.29}$$

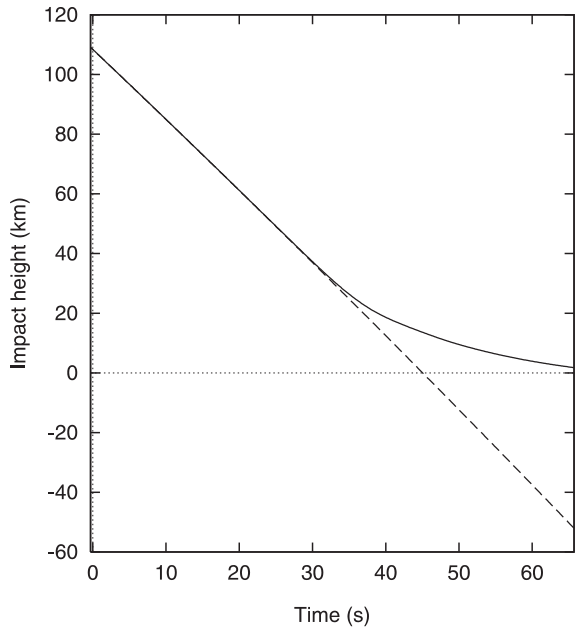

Figure 3.7 The impact parameter, $\bar{a}$, as a function of time during an occultation (solid curve). The dashed curve shows the "vacuum" impact parameter, a_0. The orbit ephemerides used are taken from occultation no. 1, day 173, 1995, which was a near aft-looking occultation.

Unlike the rate of the "vacuum" impact parameter, da_0/dt, which only depends on the occultation geometry, the rate of the "true" impact parameter, $d\bar{a}/dt$, also depends on the atmosphere, especially in the troposphere. Figure 3.7 shows the effect of the dense troposphere on the impact parameter as a function of time for a setting occultation. To calculate $a_0(t)$, orbit ephemerides were taken from a real GPS/MET occultation, and ray-tracing, through a dry atmosphere 1D-model, was used to obtain $\bar{a}(t)$.

Following our matrix notation, subscript $_i$ referring to a specific time sample of the original phase data, we have

$$\delta_a \alpha_i = \sum_{j=1}^{n} B_{ij} \delta_t \dot{L}_j, \tag{3.30}$$

with

$$B_{ij} = \begin{cases} 0 & , \quad j \neq i \\ -\left(\frac{d\bar{a}}{dt}\right)_i^{-1} & , \quad j = i \end{cases} .$$

The error covariance matrix for bending angles now becomes

$$\mathbf{C}_\alpha = \mathbf{B}\mathbf{C}_{\dot{L}}\mathbf{B}^{\mathrm{T}}. \tag{3.31}$$

Using the orbit ephemerides and the 1D-model as above to calculate the diagonal elements of $\mathbf{B}$, Figure 3.8a shows three examples (at 5, 20, and 60 km) of the correlation coefficient between one point in the atmosphere and the rest of the measured bending angles up to an impact parameter corresponding to an *impact height* (subtracting the Earth's radius) of 80 km. Due to the defocusing in the troposphere, the sampling interval (0.1 s) in the impact parameter domain becomes more narrow, giving a more narrow

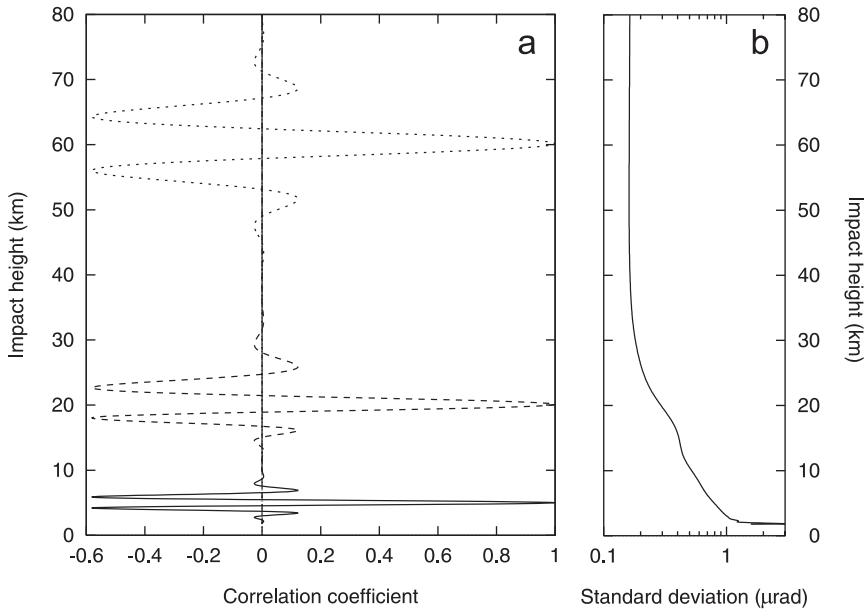

Figure 3.8 a) Bending angle correlation coefficient between three points in the atmosphere (5, 20, and 60 km) and the remainder of the bending angle profile. **b)** The standard deviation on bending angles as a function of the impact height. The few lowest data points show a relatively large standard deviation because of end-point effects.

correlation (and anti-correlation) of the bending angles at low altitudes than at high altitudes. The standard deviation (Figure 3.8b) increases at low altitudes because of the defocusing effect incorporated in the diagonal elements of $\mathbf{B}$. Close to the surface the standard deviation is about one order of magnitude larger than it is at high altitudes. If, in the smoothing process, a value of $\lambda = 10$ is used instead of $\lambda = 10^4$, the standard deviation on the bending angles becomes about 5.5 times larger at all altitudes.

3.1.4 Refractivity

The refractive index, μ, is obtained from the measured bending angles using the Abel transform (1.9). In the Earth's atmosphere the refractive index for L-band frequencies is close to 1, and the refractivity is therefore conveniently defined as $N = 10^6(\mu - 1)$. At most, the refractivity may reach a value of about 450 close to the surface. Thus, (1.9) may be linearized, relating refractivity and bending angle, without significant loss of accuracy in our error propagation estimates. Linearizing (1.9) gives

$$N(a) \approx \frac{1}{\pi} \int_a^\infty \frac{\alpha(x)dx}{\sqrt{x^2 - a^2}}, \tag{3.32}$$

where we, for now, shall regard the refractivity as a function of the impact parameter, a. The factor of 10^6 in the conventional definition of the refractivity has been disregarded in (3.32) for convenience, and henceforth we shall use the term refractivity for $N = \mu - 1$. Once having the refractivity as a function of the impact parameter, it may also be regarded as a function of r using the identity $a = \mu r$ (valid under the assumption of spherical symmetry), where r is the radial distance from the center of refraction to the tangent point height (tangent radius).

In Appendix A, equation (3.32) is discretized assuming bending angles to behave linearly between consecutive bending angle estimates. Using the result (A.7), refractivity and bending angle, in a discretized form—both regarded as a function of the independent impact parameter, a_i (or a_j)—are related as

$$\mathbf{N} = \mathbf{A}\boldsymbol{\alpha}, \tag{3.33}$$

with

$$A_{ij} = \begin{cases} 0 & , \quad j < i \\ -\frac{1}{\pi(a_{i+1}-a_i)}\left[\sqrt{a_{i+1}^2 - a_i^2} - a_{i+1}\ln\left(\frac{a_{i+1}+\sqrt{a_{i+1}^2-a_i^2}}{a_i}\right)\right] & , \quad j = i \\ \frac{1}{\pi}\left\{\frac{1}{a_j-a_{j-1}}\left[\sqrt{a_j^2 - a_i^2} - \sqrt{a_{j-1}^2 - a_i^2} - a_{j-1}\ln\left(\frac{a_j+\sqrt{a_j^2-a_i^2}}{a_{j-1}+\sqrt{a_{j-1}^2-a_i^2}}\right)\right]\right. & \\ \left. -\frac{1}{a_{j+1}-a_j}\left[\sqrt{a_{j+1}^2 - a_i^2} - \sqrt{a_j^2 - a_i^2} - a_{j+1}\ln\left(\frac{a_{j+1}+\sqrt{a_{j+1}^2-a_i^2}}{a_j+\sqrt{a_j^2-a_i^2}}\right)\right]\right\} & , \quad j > i \end{cases}$$

being the elements of an $n \times n$ upper triangular matrix $\mathbf{A}$, and $\mathbf{N}$ and $\boldsymbol{\alpha}$ being n-dimensional vectors of refractivities and bending angles, respectively. Due to the kernel, $(x^2 - a^2)^{-\frac{1}{2}}$, in (3.32), the diagonal elements in $\mathbf{A}$ are far the largest ones.

In practice the a_i's can be chosen arbitrarily, though sensibly distributed in the height range where bending angle information is available. Here we shall choose the impact parameters as the "true" ones resulting from a calculation with "no noise", and related to the time samples via the solid curve in Figure 3.7. The lowest impact parameter, a_1, corresponds to the lowest point close to the surface, while the uppermost impact parameter, a_n, corresponds to a height in the atmosphere near 109 km. An additional impact parameter, $a_{n+1} > a_n$, is defined, above which the bending angle is so small that it may be disregarded. The bending angles may not be known in practice at the chosen impact parameters, but can readily be found by linear interpolation. As long as there is a high correlation between consecutive bending angle estimates, resulting primarily from the smoothing process, interpolation will not affect the correlation nor the standard deviation noticeably.

Equation (3.33) principally gives the refractivity at various predefined impact parameters. For a given impact parameter, the tangent radius is then given by

$$r = \frac{a}{1 + N(a)}, \tag{3.34}$$

and thus the error in the tangent radius, $\delta_a r$, stemming from an error in retrieved refractivity, $\delta_a N$, at impact parameter a, is approximately given by

$$\delta_a r \approx -r\delta_a N. \tag{3.35}$$

Just as in the previous subsection where the errors in measured impact parameters were transferred to errors in the bending angles, we here transfer the tangent radius error to an error in the refractivity considering Figure 3.9. In this case the effect is a *reduction* in the refractivity error (contrary to an *enhancement* of the bending angle error in the previous subsection), and it is only appreciable in the lowest few kilometers of the atmosphere, where the refractivity gradient becomes very steep. For a dry model atmosphere (the one used here) the reduction in the standard deviation at the surface

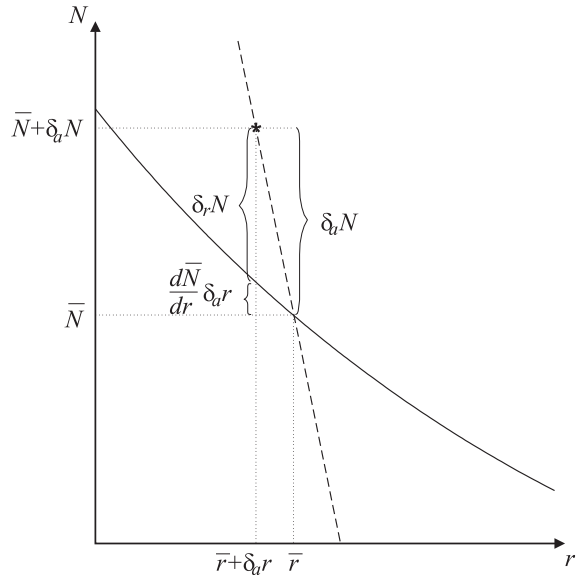

Figure 3.9 Illustration of the "true" atmospheric relation between the refractivity and the tangent radius (solid curve), and the relation $N = a/r - 1$ (from (3.34)) at a specific impact parameter (dashed curve). A given estimate of the refractivity, with corresponding tangent radius, is denoted by the * on the dashed curve.

is about 20%, but may be larger for a more realistic atmosphere with higher vertical refractivity gradients close to the surface. Following arguments similar to the ones for bending angles, the error in refractivity, $\delta_r N$, when regarded as a function of r, is given as

$$\delta_r N = \delta_a N - \frac{d\bar{N}}{dr}\delta_a r, \tag{3.36}$$

or, combined with equation (3.35),

$$\delta_r N \approx (1 + \bar{r}\frac{d\bar{N}}{dr})\delta_a N, \tag{3.37}$$

where the bar, as before, denotes "true" mean values.

Errors in refractivity, when regarded as a function of the impact parameter, are related (via equation (3.33)) to errors in bending angles as

$$\delta_a N_i = \sum_{j=1}^{n} A_{ij}\delta_a \alpha_j. \tag{3.38}$$

Thus from (3.37) and (3.38), when regarded as a function of the tangent radius, errors in refractivity are related to errors in bending angles as

$$\delta_r N_i = \sum_{j=1}^{n} R_{ij}\delta_a \alpha_j, \tag{3.39}$$

with

$$R_{ij} = \begin{cases} A_{ij} & , \quad j \neq i \\ [1 + \bar{r}_i \left(\frac{d\bar{N}}{dr}\right)_i] A_{ii} & , \quad j = i \end{cases}.$$

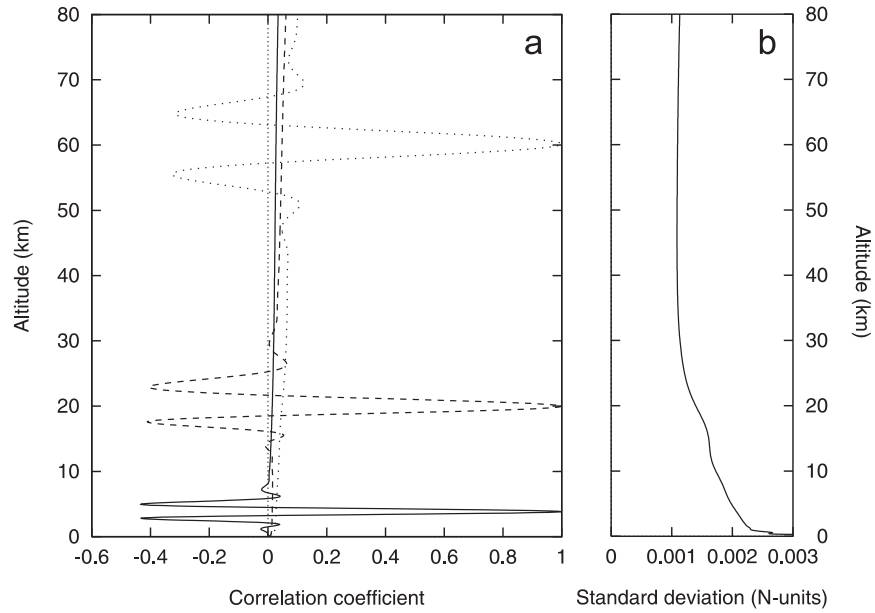

Figure 3.10 a) Refractivity correlation coefficient between three points in the atmosphere and the remainder of the refractivity profile. **b)** The standard deviation of the refractivity as a function of the altitude (1 N-unit = 10^{-6}).

Having the matrix $\mathbf{R}$ connecting bending angle and refractivity errors, the error covariance matrix, $\mathbf{C}_N$, for refractivity is found as

$$\mathbf{C}_N = \mathbf{R}\mathbf{C}_\alpha\mathbf{R}^{\mathrm{T}}. \tag{3.40}$$

Again, using the "no noise" case to obtain estimates of $\bar{N}$ and $\bar{r}$, Figure 3.10a shows three examples of the correlation between one point in the atmosphere and the rest of the profile up to an altitude of 80 km. The three examples are the same as in the previous subsection for bending angles (at impact heights 5, 20, and 60 km) but due to the effect of the tangent radius being a little lower than the corresponding impact parameter, especially at low altitudes, the lowest point is at about 3.8 km. Compared to the bending angle error correlation (Figure 3.8a), the refractivity error correlation is generally more positive, reflecting a vague accumulation of errors due to the Abel integration. In the upper atmosphere the standard deviation (Figure 3.10b) is almost constant and then it increases downwards in the troposphere. If using a value of $\lambda = 10$ in the smoothing process, the standard deviation becomes about 2.75 times larger at all altitudes.

To gain further understanding of the error propagation through the Abel transform step, it is interesting to compare with a hypothetical case where the bending angle measurements are assumed to be uncorrelated and with a constant standard deviation—say 1 μrad. Then the resulting refractivity errors look quite different (Figure 3.11). There is no negative correlation between near neighboring points and the correlation is generally much larger between points at very different altitudes. This is due to the accumulative nature of the operator, $\mathbf{A}$, making errors at higher altitudes propagate, at least to some extent, to lower altitudes. When bending angles are correlated with a negative correlation between near neighboring samples as in Figure 3.8a, errors add more destructively resulting in the correlations in Figure 3.10a. A similar behavior of

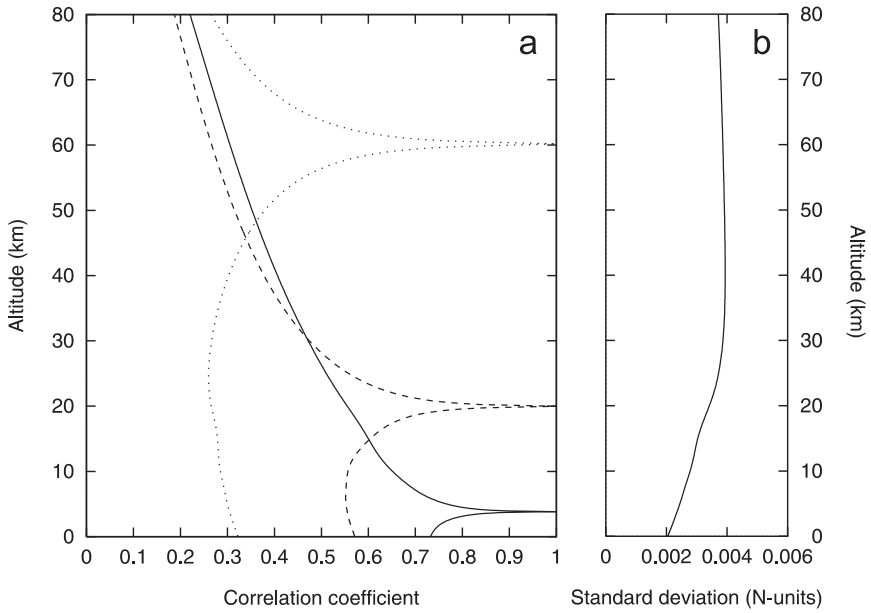

Figure 3.11 The same as Figure 3.10, but calculated from the assumption that the bending angle errors are uncorrelated with a standard deviation $\sigma_\alpha = 1\mu$rad.

the refractivity errors was found by *Kursinski et al.* [1997] using impulse responses to investigate the error propagation. Figure 3.11b presents the standard deviation in the uncorrelated bending angle case, showing that the effect of defocusing (really it is just the effect of choosing the impact parameters closer to each other in accordance with the defocusing) is in fact a net decrease in the standard deviation at lower altitudes. The minor increase in the troposphere seen in Figure 3.10b is merely due to the already larger standard deviation of the bending angles at these altitudes (cf Figure 3.8b).

3.1.5 Dry Pressure

Under dry atmospheric conditions refractivity is proportional to the density, so that pressure, and subsequently temperature, as a function of the altitude, h, can be found from the hydrostatic equilibrium assumption using (1.13). Assuming, only for the purpose of the error propagation estimates here, that the gravitational acceleration, g_0, has a constant value at all heights, equation (1.13) may be written as

$$p(h) \approx \frac{g_0}{k_1 R_\mathrm{d}} \int_h^\infty N(z)dz. \tag{3.41}$$

Using the Trapezoidal rule (approximating the refractivity by linear functions between successive r_i's in the atmosphere), (1.13) is easily discretized to obtain

$$\mathbf{p} = \mathbf{HN}, \tag{3.42}$$

with

$$H_{ij} = \begin{cases} 0 & , \quad j < i \\ \frac{g_0}{2k_1 R_\mathrm{d}}(h_{i+1} - h_i) & , \quad j = i \\ \frac{g_0}{2k_1 R_\mathrm{d}}(h_{j+1} - h_{j-1}) & , \quad j > i \end{cases}$$

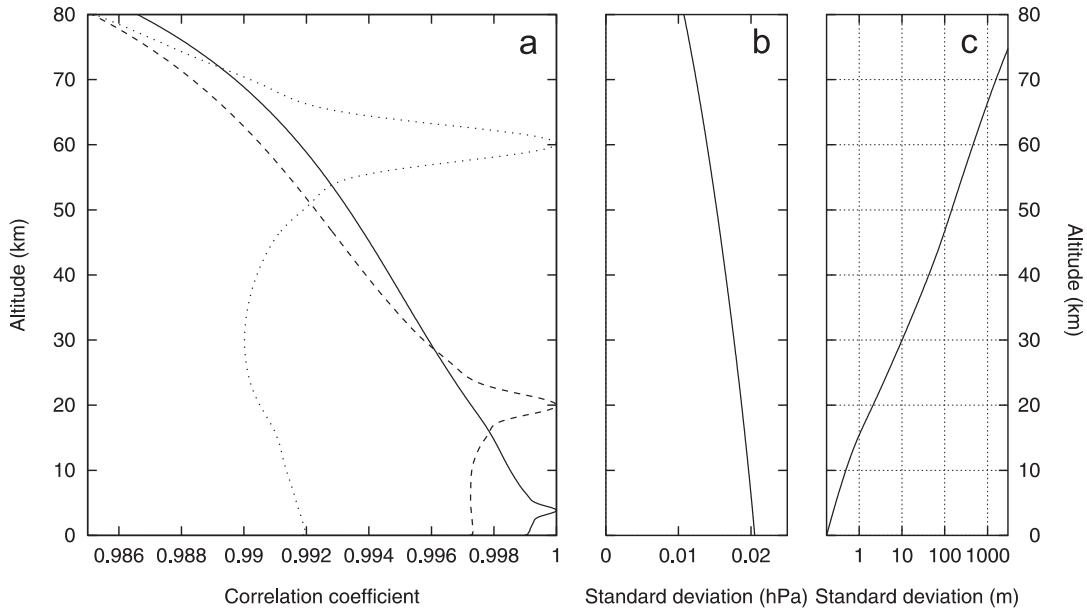

Figure 3.12 a) Pressure correlation coefficient between three points in the atmosphere and the remainder of the pressure profile. **b)** The standard deviation of the pressure as a function of the altitude. **c)** The standard deviation of the (geopotential) height as a function of the altitude.

being the elements of an $n \times n$ upper triangular matrix $\mathbf{H}$, and $\mathbf{p}$ being an n-dimensional vector of pressure estimates at the previous found r_i's. The h_i's are obtained from the r_i's simply by subtracting the radius of the Earth. In this case the error propagation is strictly linear according to (3.42), and the pressure error covariance matrix, $\mathbf{C}_p$, is given by

$$\mathbf{C}_p = \mathbf{H}\mathbf{C}_N\mathbf{H}^{\mathrm{T}}. \tag{3.43}$$

The resulting error correlation for the pressure profile between different points in the atmosphere below 80 km is shown in Figure 3.12a. It is seen that the hydrostatic integration results in a very high correlation even between points at very different altitudes. Unlike the Abel integration the hydrostatic integration does not have a very localized kernel to prevent "long distance" error correlation. The accumulation effect is also seen on the standard deviation (Figure 3.12b), gradually increasing as we go down through the atmosphere.

Often in meteorological applications the geopotential height, Z, associated with a pressure level is of interest more than the pressure as a function of the altitude. The geopotential height at pressure p, is defined as

$$Z(p) = \frac{1}{g_0}\int_0^{h(p)} g(z)dz. \tag{3.44}$$

For the purpose of error propagation estimates we may again disregard the height dependency of the gravitational acceleration, i.e., $g(z) = g_0$, and the geopotential height is then just the actual height, $h(p)$, i.e., the inverse function of $p(h)$. An error in the pressure, $\delta_h p$, at a specific altitude, is easily converted to an error in the altitude, $\delta_p h$,

at that pressure level:

$$\delta_p h = -\left(\frac{d\bar{p}}{dh}\right)^{-1} \delta_h p, \tag{3.45}$$

where the bar denotes the "true" mean value. The reasoning for (3.45) follows the reasoning in previous subsections, noting that (3.45) is just a special case of relations like (3.23) or (3.36). From (3.45) it follows that the error correlation for the (geopotential) height is the same as for pressure, but the standard deviation, σ_h, is related to the standard deviation of the pressure, σ_p, as

$$\sigma_h = \left|\frac{d\bar{p}}{dh}\right|^{-1} \sigma_p, \tag{3.46}$$

or, using the hydrostatic equilibrium assumption,

$$\sigma_h = \frac{k_1 R_\mathrm{d}}{g_0} \bar{N}^{-1} \sigma_p. \tag{3.47}$$

Figure 3.12c shows the standard deviation of the (geopotential) height as a function of the altitude.

For $\lambda = 10$ standard deviations become a factor of ~ 1.75 larger at all altitudes, for both pressure and height.

3.1.6 Dry Temperature

The errors in temperature are a combination of errors in refractivity and pressure, since for a dry atmosphere the temperature is obtained from the dry air refractivity equation (1.6) as

$$T(h) = k_1 \frac{p(h)}{N(h)}. \tag{3.48}$$

Alternatively we may combine (3.48) and (3.42) to express the temperatures, T_i (at altitudes h_i), related to the N_i's only:

$$T_i = k_1 \frac{1}{N_i} \sum_{j=1}^{n} H_{ij} N_j. \tag{3.49}$$

This is a non-linear relation and estimates of errors in temperature are obtained via a Taylor expansion to first order around the mean:

$$\begin{aligned} T_i &= \bar{T}_i + \delta T_i \\ &= \bar{T}_i + \sum_{k=1}^{n} \frac{dT_i}{dN_k} \delta N_k \\ &= \bar{T}_i + \frac{1}{\bar{N}_i} (k_1 \sum_{j=1}^{n} H_{ij} \delta N_j - \bar{T}_i \delta N_i) \end{aligned} \tag{3.50}$$

where the subscript on the δ's has been omitted for convenience, since errors are now always related to a specific altitude in the atmosphere. Equation (3.50) leads to

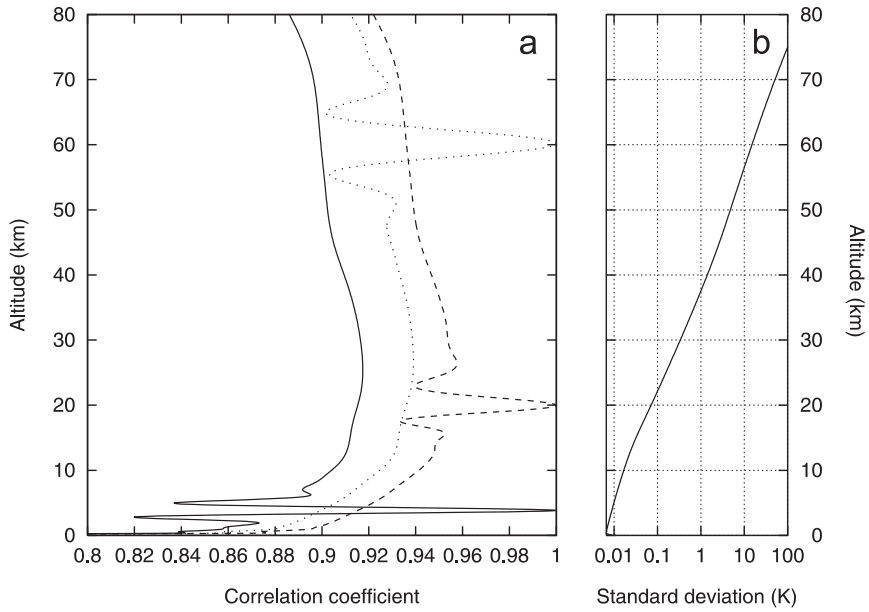

Figure 3.13 a) Temperature correlation coefficient between three points in the atmosphere and the remainder of the temperature profile. **b)** The standard deviation of the temperature as a function of the altitude.

$$\delta T_i = \sum_{j=1}^{n} Q_{ij} \delta N_j, \tag{3.51}$$

with

$$Q_{ij} = \begin{cases} \bar{N}_i^{-1} k_1 H_{ij} & , \quad j \neq i \\ \bar{N}_i^{-1}(k_1 H_{ii} - \bar{T}_i) & , \quad j = i \end{cases},$$

and the error covariance matrix, $\mathbf{C}_T$, for temperature is thus obtained as

$$\mathbf{C}_T = \mathbf{Q}\mathbf{C}_N\mathbf{Q}^{\mathrm{T}}, \tag{3.52}$$

where $\mathbf{Q}$ is an $n \times n$ upper triangular matrix with elements Q_{ij}. Due to the N_i^{-1} dependency of the Q_{ij}'s, errors in temperature become very large at high altitudes. Figure 3.13a shows the temperature error correlation between points in the atmosphere up to 80 km, and Figure 3.13b shows the standard deviation. The relatively high correlation between all altitudes is mostly a result of the hydrostatic integration, although the correlation is less than for pressure since here the pressure is divided by the more uncorrelated refractivity to obtain the temperature.

Finally, the temperature error correlation and standard deviation, using $\lambda = 10$ in the smoothing process, is presented in Figure 3.14, showing that the correlation becomes generally smaller and more narrow (by a factor of ~ 3) in the vicinity of the altitude in question, while the standard deviation becomes larger by a factor of ~ 2.

3.1.7 Discussion of Results

The error analysis above was based on a simple representation of the excess phase errors, having a constant standard deviation for the whole measurement. As already

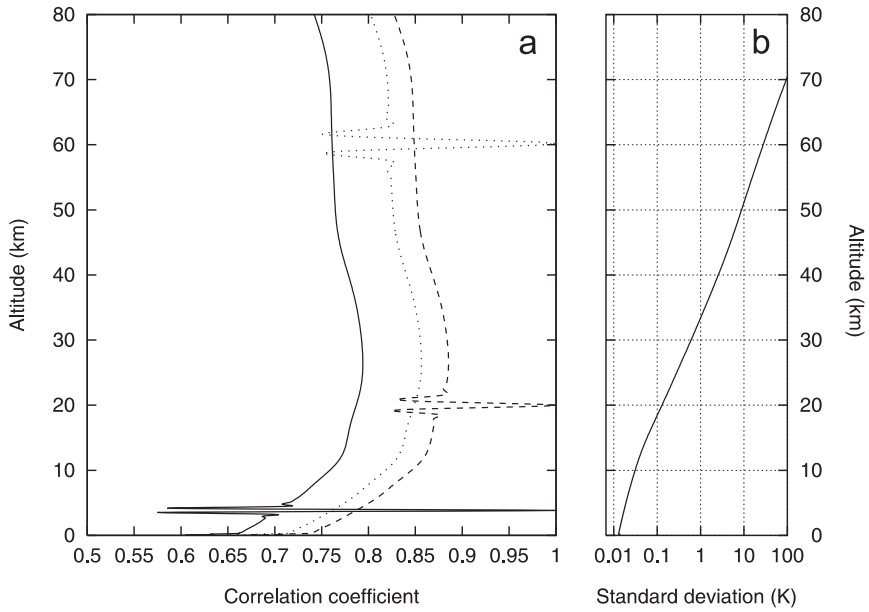

Figure 3.14 Same as Figure 3.13, but with $\lambda = 10$ instead of $\lambda = 10^4$.

mentioned, this does not hold for real measurements, and the results presented should be regarded as illustrative examples rather than quantitative realities. It does, however, give an understanding of how errors propagate in general, and how the pressure and temperature error correlation coefficient, due to the hydrostatic integration, will be relatively high over the whole measurement range when integration is performed from a high altitude and down. In reality the errors at the high altitude end are sought reduced by implementing statistical optimization techniques where a model bending angle profile gradually replaces the data profile above some specified altitude depending on the noise level [*Sokolovskiy and Hunt*, 1996; *Hocke*, 1997; *Gorbunov and Gurvich*, 1998a]. This reduces the overall standard deviation and vertical correlations of pressure and temperature, as will be shown in Section 3.2. Comparing the standard deviations for $\lambda = 10$ and $\lambda = 10^4$, we have also seen that the influence of the degree of smoothing is not linear down through the processing chain: A factor of about 5.5 in the standard deviations of the bending angles reduces to a factor of about 2.75 in the standard deviations of the refractivity and then further to a factor of 2 in the standard deviations of the temperature. This is a consequence of the different correlation scales for $\lambda = 10$ vs $\lambda = 10^4$. The large drop in the factor when going from bending angle to refractivity (5.5 to 2.75) indicates that the Abel integration mitigates the errors (relatively speaking) when correlations are narrow. In other words, when applying more smoothing of the excess phase, one does not gain much in terms of smaller errors in the refractivity, compared to the gain in terms of smaller errors in the bending angle.

When the standard deviation of the phase error varies throughout the occultation, as it does for a real measurement, it may be difficult to identify a distinct corner on the L-curve, and to define an "optimum" value of the regularization parameter, λ. For illustration, the L-curve, taking the 50 Hz data from a real GPS/MET occultation, is shown in Figure 3.15. To be on the "safe side" it is probably wise, in general, to choose a value closer to 10^5 than to 10^8 (for 50 Hz GPS/MET data).

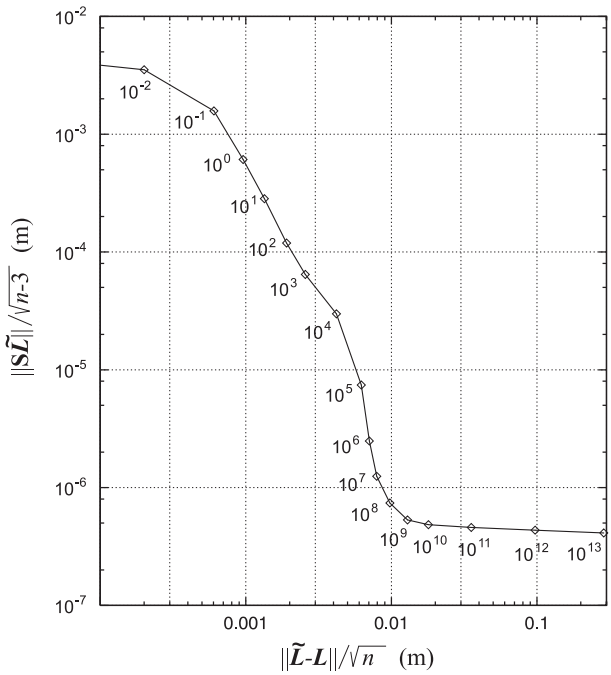

Figure 3.15 The L-curve for a real 50 Hz GPS/MET data set (L1, occ. 665, day 46, 1997, $n = 2950$). Numbers by the curve refer to the value of the regularization parameter.

Other methods of smoothing may be applied, for example using statistical regularization, assuming error covariance matrices for the "unknown" Doppler, as well as for the phase measurement [*Gorbunov et al.*, 1996a; *Gorbunov and Gurvich*, 1998a], or using a low pass filter with a cutoff frequency corresponding roughly to the inherent vertical resolution limit given by the first Fresnel diameter [*Kursinski et al.*, 1997]. In general, the detailed numerical procedure at different levels of processing, as well as the number of data points included in the retrieval will affect the errors and the correlations. Also the geometry has influence. For example, a slow descending tangent point, indicating a more side-looking occultation, gives more data points throughout a specific height range, resulting in a more dense set of data points affecting both the standard deviation and the correlation.

The transmission of errors from the impact parameter domain to the bending angle domain only holds for small impact parameter errors compared to the vertical scale over which the "true" bending angle variations may be regarded as linear. The same goes for errors in tangent radius and pressure level when transmitted to errors in refractivity and height, respectively. Other authors [*Lipa and Tyler*, 1979; *Feng and Herman*, 1998] handle the uncertainty in the impact parameter by regarding it as a dependent variable, like the bending angle, and operates (at least in principle) with error covariances for both of them, and for the correlation between them. However, in practice, when solving the Abel integral, the impact parameter should be regarded as an *independent* variable as it is here, and the "transmission" procedure seems therefore to be the most appropriate.

In the troposphere where diffraction and atmospheric multi-path may become appreciable, the quantitative error and correlation estimates are questionable. In fact the whole theory of the excess Doppler being directly related to bending angles, in principle breaks down [*Gorbunov and Gurvich*, 1998a].

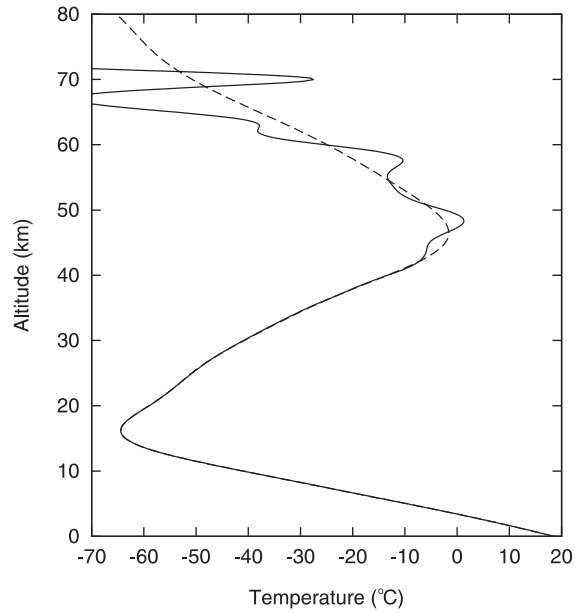

Figure 3.16 Retrieved model temperature profiles as a function of altitude. The solid curve is obtained from synthetic phase data, superimposed with random, Gaussian-distributed noise ($\sigma_L = 3$ mm), reduced to 10 Hz, and subsequently smoothed with $\lambda = 10^4$. The dashed curve is a "no noise" retrieval.

It should also be remembered that the Abel transform solution is based on the spherical symmetry assumption. This means that systematic errors due to large scale along-track horizontal variations in refractivity will dominate in the lower atmosphere [*Kursinski et al.*, 1997], and hence, the statistical error and correlation estimates should not be regarded as representative for retrieved atmospheric profiles in general. Vertically localized horizontal perturbations (like a "blob" of extra density) in the refractivity will map into the bending angles and derived refractivity profiles as large localized errors [*Ahmad and Tyler*, 1998a]. The error correlation between different altitudes in the atmosphere due to such errors will depend on the extent and location (relative to the tangent point) of the atmospheric perturbations.

When water vapor is present in the troposphere, the pressure and especially the temperature as derived under the dry air assumption, may be far from the truth. However, the error in the "dry pressure" and the "dry temperature" can be regarded as an indication of how accurate water vapor potentially may be retrieved using auxiliary precise temperature information or vice versa.

Cycle slips in the phase measurements, and maybe subsequent loss of track, which predominantly occurs in the lowest part of the troposphere, will appear as large spikes and irregularities in the Doppler so that the basis for the error analysis (assumption of small errors) is generally violated if such outliers are not removed.

For more accurate retrievals the detailed processing is different from the one outlined above, especially when solving the Abel integral. In the software developed and implemented as a part of this study, a change of variable is applied so that the limits in the Abel integral is both finite and there is no singularities. The influence on the resulting standard deviations and correlations when using such a change of variable, and other numerical particularities when solving the hydrostatic integral, is difficult to asses, but simulations (below) show that the resulting effect on the dry temperature error is small.

Finally it is very illustrative at this point to present the temperature results obtained with noise and without noise. Figure 3.16 shows the retrieved temperature for the 1D-model, using $\lambda = 10^4$. Large oscillations at, and above the stratopause are due to the noise on the phase data ($\sigma_L = 3$ mm), and similar oscillations should be expected in retrievals of real temperature profiles. Thus, such observed oscillations must not be confused with wave-like structures generated by, e.g., gravity waves in the real atmosphere, and care in interpretations should be taken in particular when the characteristic scale of the oscillations is of the same order as the vertical resolution due to the smoothing process. In Figure 3.16 the oscillations are nicely distributed around the "no noise" profile representing the truth, but often there is an apparent bias to one of the sides, in accordance with the high vertical correlation seen in figure 3.13.

The results in Figure 3.16 have been obtained via the linearized procedure as described above, whereas most other retrieval results in this thesis are obtained using more advanced algorithms, taking into account—among other things—the more accurate relationship between excess Doppler and bending angles, the variation of the gravitational acceleration, the Earth's oblateness, ionosphere calibration, and a priori constraints (e.g., statistical optimization) at the high altitude end to reduce the apparent bias (i.e vertical correlations) and random oscillations in individual temperature retrievals.

3.2 Simulation of Temperature Errors and Correlations

Simulations have been carried out to further investigate and validate the random error propagation. Synthetic phase data were produced using real orbit ephemerides and high accuracy ray-tracing through the 1D model of the neutral atmosphere. Random, Gaussian-distributed noise was then added to the synthetic excess phase data, and the data were subsequently smoothed and inverted using advanced algorithms to retrieve the temperature profile. For each of the cases below, a total of $n = 100$ runs have been carried out to calculate the statistics in the form of standard deviations, while $n = 1000$ runs were carried out for the calculation of the correlations. The standard deviation on the temperature was calculated as

$$\sigma_T = \frac{1}{\sqrt{n-1}} \sqrt{\sum_{k=1}^{n} (T_k - \bar{T})^2}, \tag{3.53}$$

where $\bar{T}$ is the sample mean at the altitude in question, while the covariance between temperatures at two different altitudes, h_i and h_j, was calculated as

$$C_T(h_i, h_j) = \frac{1}{n-1} \sum_{k=1}^{n} \Big(T_k(h_i) - \bar{T}(h_i)\Big)\Big(T_k(h_j) - \bar{T}(h_j)\Big). \tag{3.54}$$

The intermediate products: bending angles, refractivity, and pressure profiles—although interesting enough—have for the reason of brevity not been considered. However, the influence on these products when using different degrees of smoothing and noise levels, can, at least qualitatively, be deduced from the influence on the temperature profiles and the results in the previous section regarding the theoretical analysis.

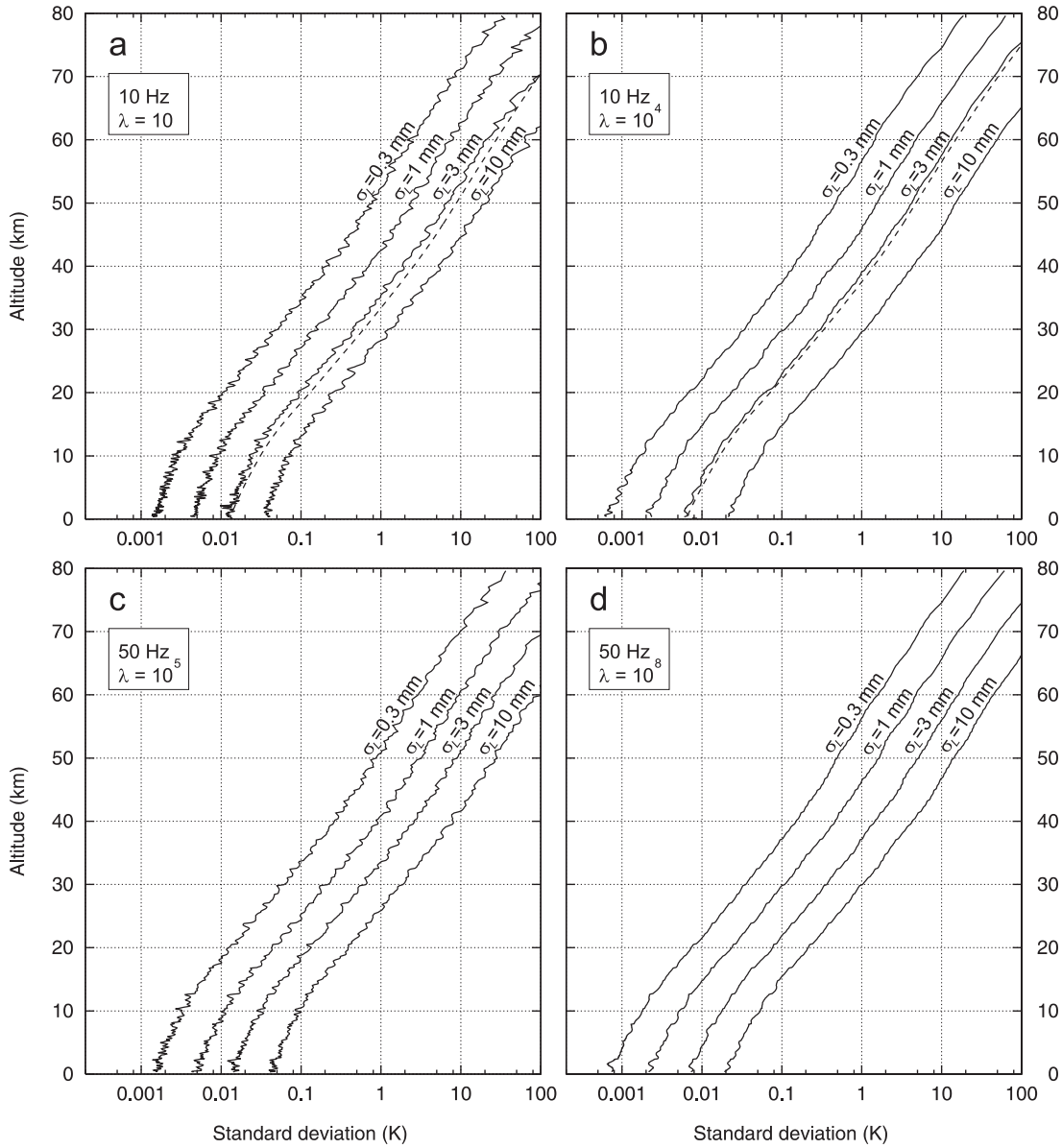

Figure 3.17 Relations between standard deviations of excess phases (values of noise levels by the curves are related to 50 Hz data in all cases) and standard deviations of retrieved temperatures. **a)** 10 Hz, $\lambda = 10$. **b)** 10 Hz, $\lambda = 10^4$. **c)** 50 Hz, $\lambda = 10^5$. **d)** 50 Hz, $\lambda = 10^8$. The results from the theoretical analysis are shown as dashed curves.

3.2.1 Results

Both 10 Hz data and 50 Hz data has been simulated. Four different values of the standard deviation of the phase noise (0.3 mm, 1 mm, 3 mm, 10 mm) on the 50 Hz data has been considered, together with corresponding levels on the 10 Hz data (reducing the standard deviations by a factor of $\sqrt{5}$). The results of the 10 Hz simulations allow for direct comparison with the results of the theoretical analysis.

Two different degrees of smoothing have been applied in the simulations. For 10 Hz data, values of the regularization parameter was set to $\lambda = 10$ and $\lambda = 10^4$, and for 50 Hz data it was found, empirically, that corresponding values, in terms of resulting

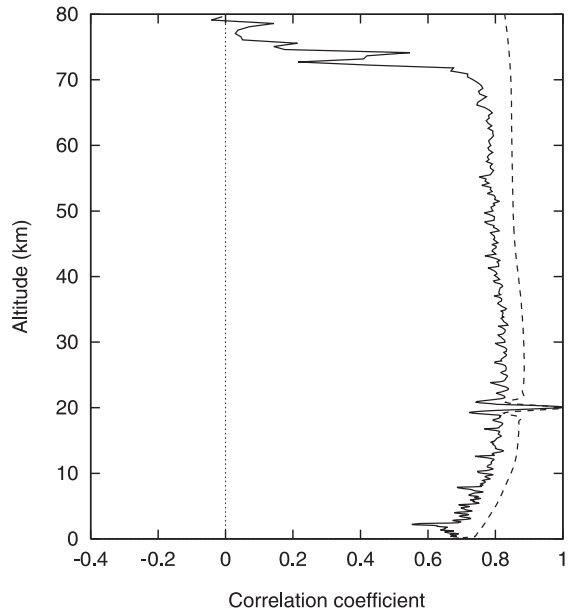

Figure 3.18 Temperature correlation coefficient between one point in the atmosphere and the remainder of the temperature profile (50 Hz, $\lambda = 10^5$, $\sigma_L = 3$ mm). As a reference the correlation coefficient from the theoretical analysis (10 Hz, $\lambda = 10$) is shown as the dashed curve.

vertical resolutions, should be set to approximately $\lambda = 10^5$ and $\lambda = 10^8$, respectively.

Figure 3.17 shows the standard deviation of the temperature for 10 Hz and 50 Hz simulations, using coarse or finer smoothing, and for the four different noise levels as indicated. For comparison, the results from the theoretical analysis is also shown in the two "10 Hz/3 mm" cases. The simulations with the larger values of λ (10^4 for 10 Hz, 10^8 for 50 Hz), which are close to the "optimum" values from the theoretical analysis, gives very alike standard deviations for the same noise levels. It was also verified (not shown) that the vertical correlations, for both 10 Hz and 50 Hz data, were much the same as the correlations found in the theoretical analysis assuming 10 Hz data. Furthermore it was found that the vertical correlations are more or less independent of the noise level. For the smaller values of λ (10 for 10 Hz, 10^5 for 50 Hz) the 10 Hz simulations give standard deviations and vertical correlations a bit smaller than the 50 Hz simulations. The "10 Hz/3 mm" simulation is also a bit smaller than the theoretical curve (Figure 3.17a). This latter finding may be attributed to the more advanced way of processing, in particular the way of handling the upper boundary when solving the Abel integral.

As an example of simulated vertical correlations—for 50 Hz data, $\lambda = 10^5$, and $\sigma_L = 3$ mm—the temperature correlation coefficient between one point in the atmosphere (at 20 km) and the rest of the profile is shown in Figure 3.18. As seen, the vertical temperature correlation below ~ 70 km is only slightly smaller than the results from the theoretical analysis. The large discrepancy above ~ 70 km where the simulated correlation drops to near zero, is due to the very large random temperature errors at these altitudes resulting in sometimes negative temperatures ($< -273°$C). Thus, the linearization in the theoretical analysis, when treating the error propagation from refractivity to temperature, was not valid at these altitudes where errors in refractivity become comparable with the absolute refractivity value. Note that the vertical corre-

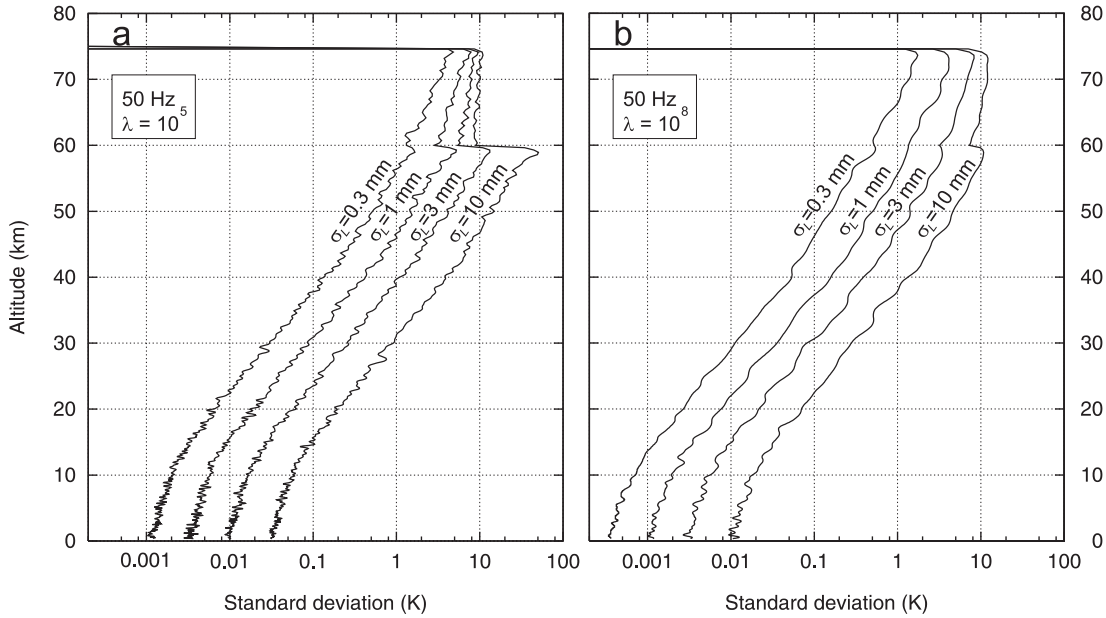

Figure 3.19 Relations between standard deviations of excess phases and standard deviations of retrieved temperatures when statistical optimization is applied between 60 km and 75 km (50 Hz data). **a)** $\lambda = 10^5$. **b)** $\lambda = 10^8$.

lations (and standard deviations) derived in the theoretical analysis is wrong only for the temperature, and only at the high altitude end. The operations leading to bending angles, refractivity and pressure are all linear—or almost linear—operations.

The simulation results above were obtained using the calculated bending angle data up to an altitude of 109 km. When solving the Abel integral the bending angles were extrapolated beyond 109 km using a 1D model of bending angles corresponding to the 1D refractivity model used in the forward ray-tracing calculations. In reality, ionosphere residuals in terms of a bias (cf Section 4.1), do not allow sensible use of real data to altitudes higher than $\sim$ 70–75 km, and a climatological extrapolation (or other means of dealing with the high altitude boundary of the Abel integration) has to be applied already at, or below, this altitude. Further, statistical optimization may be applied to reduce random errors at the high altitude end [*Sokolovskiy and Hunt*, 1996; *Hocke*, 1997; *Gorbunov and Gurvich*, 1998a]. To investigate the effect of random errors on the temperature retrievals when applying statistical optimization, simulations was carried out using the approach of *Hocke* [1997] between 60 km and 75 km. As climatology the 1D model of bending angles was used. Above 75 km bending angles was set to be identical to the bending angles of the model. Figure 3.19 shows the results for 50 Hz data. It is seen that the statistical optimization not only reduces the standard deviation above 60 km but also below. This is primarily due to the hydrostatic integration, propagating errors downwards. Of course, the use of wrong statistics/climatology may in practice introduce an additional bias not intended.

Simulations also show that the overall vertical correlation is reduced appreciably when applying the statistical optimization (Figure 3.20). The overall correlation coefficient in the altitude range from surface to near 60 km is reduced from ~ 0.8 to less than 0.2. Above 60 km the temperature is virtually uncorrelated with temperatures at 20 km. Again, the hydrostatic integration is the main reason for this effect, not accumulating

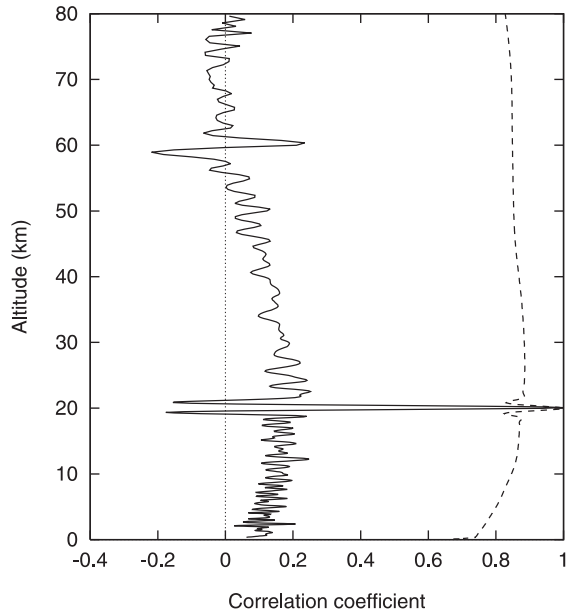

Figure 3.20 The same as Figure 3.18, but with statistical optimization applied between 60 km and 75 km.

errors all the way from 109 km and down, but only from 75 km, and with artificially reduced bending angle errors between 75 km and 60 km.

Reducing the lower limit of the statistical optimization range to 45 km, it was found that the vertical correlation virtually disappears, except—of course—between neighboring altitudes corresponding to the vertical resolution. The standard deviation below 45 km was not affected by the lower limit of the statistical optimization range being either 45 km or 60 km. Only in the range between 45 km and 60 km a noticeable reduction of the standard deviation was seen, indicating that the main reason for the overall reduction of the standard deviation (comparing Figures 3.17c,d and 3.19a,b) is mostly due to the data "cut off" at 75 km and extrapolation with a model profile beyond this altitude.

3.2.2 Empirical Relation Between Phase and Temperature Errors

All simulation results suggest a near log-linear relationship between the temperature standard deviation and the standard deviation of excess phases, at least if we are concentrating on altitudes below the altitude where we chose to set in with statistical optimization. Also, because of the near exponential decrease of the refractivety with height, h, we may approximate the height dependence of the temperature standard deviation with a simple exponential function above 10 km altitude. Thus, a simple empirical relation can be derived, in the height range 10–40 km, by a least squares fit to the results shown in Figures 3.17 and 3.19. Such an approximate relation will have the form

$$\sigma_T = \sigma_L^q \exp\left(\frac{h - h_0}{H_\mathrm{s}}\right) \tag{3.55}$$

where H_s is a mean scale height, h_0 is a reference altitude, and q is expressing the non-linearity between phase and temperature errors. In Table 3.1 these parameters are listed for each of the six cases in Figures 3.17 and 3.19. These numbers assume that σ_L

Sampling rate	smoothing degree	stat. opt. applied	q	h_0	H_s
10 Hz	low	no	0.92	42.6	6.76
50 Hz	low	no	0.97	40.7	6.66
10 Hz	high	no	0.99	45.2	6.71
50 Hz	high	no	0.97	44.7	6.70
50 Hz	low	yes	0.96	46.4	7.00
50 Hz	high	yes	0.92	53.0	6.91
10 Hz	high/weighted	–	0.60	43.5[a]	6.85

[a]The value is not identical to the one cited in [*DMI and TERMA*, 1998] because the σ_L in that work was related to a 10 Hz sampling rate. Here the value has been recalculated in order to relate the σ_L to a 50 Hz sampling rate.

Table 3.1 Outcome of a least squares fit to the simulation results using the functional form (3.55). The last row shows the results from an earlier work [*DMI and TERMA*, 1998].

(related to 50 Hz data) is expressed in millimeter and σ_T in Kelvin. In a contractual work for the European Space Agency [*DMI and TERMA*, 1998], another smoothing approach[2] than the one used here was applied, and a similar least squares fit, also based on simulation results, led to the values given in the last row of Table 3.1.

From the fourth column of the table it is clear that the relation is approximately linear ($q \approx 1$) with respect to the noise level, when the regularization parameter is held at a constant value. In the earlier result (last row) the smoothing degree was dependent on the noise level, which is the reason for the somewhat lower value of q. The reference altitude, h_0, in the fifth column, is the altitude at which the temperature standard deviation reaches a value of 1 K for an excess phase noise of 1 mm. Thus, the value of h_0 could be regarded as a quality measure of the retrieval method applied: the higher the value, the better. Of course it only says something about the standard deviation, nothing about vertical resolution or correlation.

The GPS/MET temperature profiles obtained in the paper in Appendix C.3 have been processed with $\lambda = 3 \cdot 10^5$ (50 Hz data) and statistical optimization starting at 45 km based on the approach of *Hocke* [1997].

[2]The approach was empirical and substantially different from the regularization approach used here. The smoothing degree was very high and varied with altitude and noise level. At $\sim$ 60 km and above bending angles were very close to an exponential fit to the data, resembling something like statistical optimization.

Chapter 4

Systematic Error Assessments and Improvements

4.1 Ionosphere Calibration (extended abstract to the paper in Appendix C.1)

Elimination of the ionospheric contribution to atmospheric delays in GPS radio occultation measurements is a key issue in the retrieval of accurate pressure and temperature profiles above the tropopause. The traditional so-called "ionosphere-free" combination of the L1 and L2 phase paths given by (1.10), eliminating the first order ionospheric effects, is not sufficient because of the non-negligible bending of the two ray paths. Due to the dispersive nature of the ionosphere the L1 and L2 signals will follow slightly different paths giving rise to an ionospheric residual, here referred to as the "dispersion" residual. Also higher order ionospheric terms contribute to the total residual, but the dispersion residual is the most dominant. *Vorob'ev and Krasil'nikova* [1994] proposed a linear combination of the L1 and L2 bending angles, α_1 and α_2, at a common impact parameter, a:

$$\alpha_{\mathrm{C}}(a) = \frac{f_1^2\alpha_1(a) - f_2^2\alpha_2(a)}{f_1^2 - f_2^2}. \tag{4.1}$$

This approach gives better results in most cases, but still suffers from various approximations, one of them being the assumption of spherical symmetry in the ionosphere.

In the paper in Appendix C.1 an improved phase path correction method is presented, dealing with the problem of L1 and L2 ray path separation due to dispersion. Using Taylor expansions, formulas are derived showing how both the dispersion and the second order ionospheric residuals can be evaluated using measurements of the Satellite-to-Satellite Total Electron Content (S–S TEC). Ignoring the influence from the geomagnetic field, the resulting improved phase path correction method is given by

$$\begin{aligned} L_{\mathrm{C}} = {} & \frac{f_1^2 L_1 - f_2^2 L_2}{f_1^2 - f_2^2} - \frac{1}{2}\frac{C^2}{f_1^2 f_2^2}\left[D\zeta\left(\frac{d}{da}\int_{\mathrm{F}} N_{\mathrm{e}} ds\right)^2 + a\frac{d}{da}\int_{\mathrm{F}} N_{\mathrm{e}}^2 ds\right] \\ & - \frac{1}{2}\frac{C^3}{f_1^2 f_2^2}\left(\frac{1}{f_1^2} + \frac{1}{f_2^2}\right)(D\zeta)^2\left(\frac{d}{da}\int_{\mathrm{F}} N_{\mathrm{e}} ds\right)^2 \frac{d^2}{da^2}\int_{\mathrm{F}} N_{\mathrm{e}} ds, \end{aligned} \tag{4.2}$$

where N_{e} is the electron density, C is the constant given in Section 1.3, and D and ζ are the reduced distance (3.25) and the defocusing factor (3.27), respectively. The

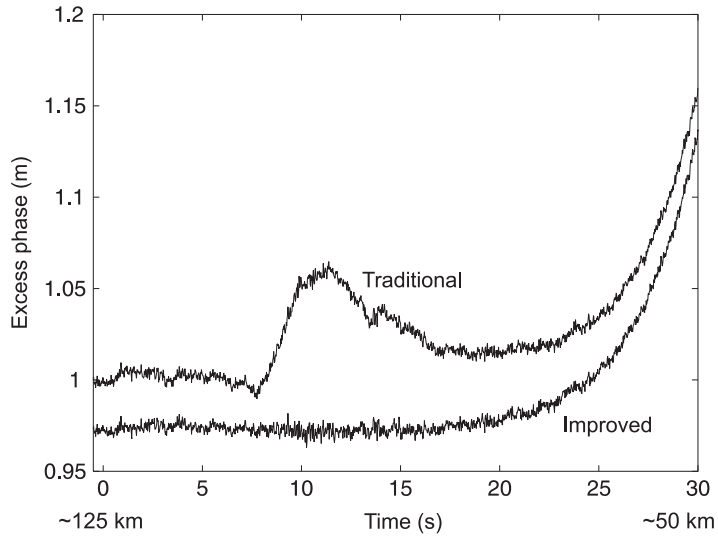

Figure 4.1 Ionosphere corrected excess phases as a function of time, using either the traditional phase path correction method or the improved method. The data are taken from the GPS/MET experiment (UCAR data, occ. no. 259, day 35, 1997) [*Syndergaard*, 1999b].

subscript, $_{\mathrm{F}}$, indicates that integrals are to be evaluated along the path that the signal would have followed in the absence of the ionosphere.

Also this method relies on the spherical symmetry assumption and its validity in general is discussed in the paper. It is also shown that the main difference resulting from using (4.1) or (4.2) comes from the second term in the square brackets of (4.2) being connected to the integration of the squared electron density, $\int_{\mathrm{F}} N_{\mathrm{e}}^2 ds$, between the satellites. Figure 4.1 shows the improved phase path correction applied to the excess phases of a GPS/MET occultation. It is seen how the bulge resulting from the traditional method (1.10) is removed using the improved method.

The GPS/MET data are from a period of low solar activity, and therefore the residual bulge in the above example, resulting from the traditional phase path correction, is only moderate. In a period of high solar activity, not yet experienced by the GPS/MET experiment, much larger dispersion residuals are expected. Simulations representative of day-time conditions, during solar maximum, show that the dispersion residual may become larger than 30 cm. Using the improved phase path correction method or an improved bending angle correction method, most of this residual can be eliminated, but still, ionosphere asymmetry conditions may limit the accuracy in bending angles to about 10^{-7} rad.

With a third frequency a triplex-frequency phase path combination would eliminate the first order dispersion residual and give results practically insensitive to ionospheric asymmetry conditions.

4.2 The Spherical Symmetry Assumption

Without any prior knowledge about the atmospheric horizontal structure, the best one can do in the inversion of a single set of radio occultation data, is to apply the assumption of spherical symmetry. Both the processing of bending angles as a function of the impact parameter, and the inversion using the Abel transform to obtain refractivity, is based

on the spherical symmetry assumption.

It is indeed possible to generalize the inversion to non-spherical geometry using non-spherical layers in the "onion skin" model [*Melbourne et al.*, 1994]. However, it still requires a priori knowledge to specify any departure from sphericity of the layers. Also *Ilyushin and Terekhova* [1998] have presented an approach, generalizing the retrieval to take into account the along-ray dimension, and requiring only limited a priori knowledge. Derivations of a 2D resolution kernel have been provided by *Gorbunov* [1990] and *Ahmad and Tyler* [1998a].

Using the spherical symmetry assumption, the systematic errors arising from large-scale horizontal gradients have been studied in detail by *Ahmad and Tyler* [1998b]. They find that for the Earth's atmosphere, gradients may in extreme cases produce temperature errors of several Kelvin, depending on the occultation geometry. Simulations by *Kursinski et al.* [1997] show errors in the lower atmosphere of about 0.5 K under nominal conditions. *Gurvich and Sokolovskiy* [1985] investigated the errors in the retrieved pressure when simulating an anti-cyclone or a cyclone. They found relative pressure errors of no more than 0.3 %. The effects of medium-scale structures have been investigated by *Ahmad and Tyler* [1998a] using the 2D resolution kernel, finding that vertically localized horizontal perturbations (like a "blob" of extra density) in the refractivity will map into derived refractivity profiles as large localized errors of several percent. The effects of gravity waves have been studied by *Belloul and Hauchcorne* [1997], finding that errors of several Kelvin may occur in the stratosphere.

Two subjects have been studied in greater detail in this thesis. One is the effects of the atmospheric horizontal structure following the Earth's ellipsoidal shape rather than that of a sphere, and the other has been to investigate the effects on temperature in the worst possible case of a very sharp weather front.

4.2.1 Impact of Earth's Oblateness (extended abstract to the paper in Appendix C.2)

Utilizing real orbit ephemerides from the GPS/MET experiment, radio occultations have been simulated using a 3D ray-tracing code, taking into account the non-spherical shape of the atmosphere due to the oblateness of the Earth. Subsequent inversion of the synthetic data shows that neglect of the Earth's oblateness in the retrieval of temperature profiles may cause a bias at altitudes below 40 km. From this altitude the temperature bias increases downwards, and can, in extreme cases, become as large as 3 K at 10 km altitude and 6 K at the ground (Figure 4.2a). The size of the bias depends on the occultation geometry and the geographical latitude of the limb zone. The origin of the biases seen in Figure 4.2a comes from the incorrect assumption of spherical symmetry with respect to the Earth's center. Since the Earth's center is not generally the same as the local center of refraction, both bending angles and impact parameters will consequently be wrong. Figure 4.3 shows the situation when the occultation plane is coincident with a meridian plane. In this case the angle, φ, between the ray direction and the LEO satellite velocity is uniquely determined from the measured phase (or excess Doppler), and simple geometry shows that an estimate of the bending angles and impact parameters will result in wrong values.

In the paper in Appendix C.2 a method to correct for the bias is proposed using an assumption of local spherical symmetry tangential to the ellipsoid (Figure 4.3). After a simple correction, dry temperature profiles are retrieved within 0.25 K ($\sim$ 0.1%)

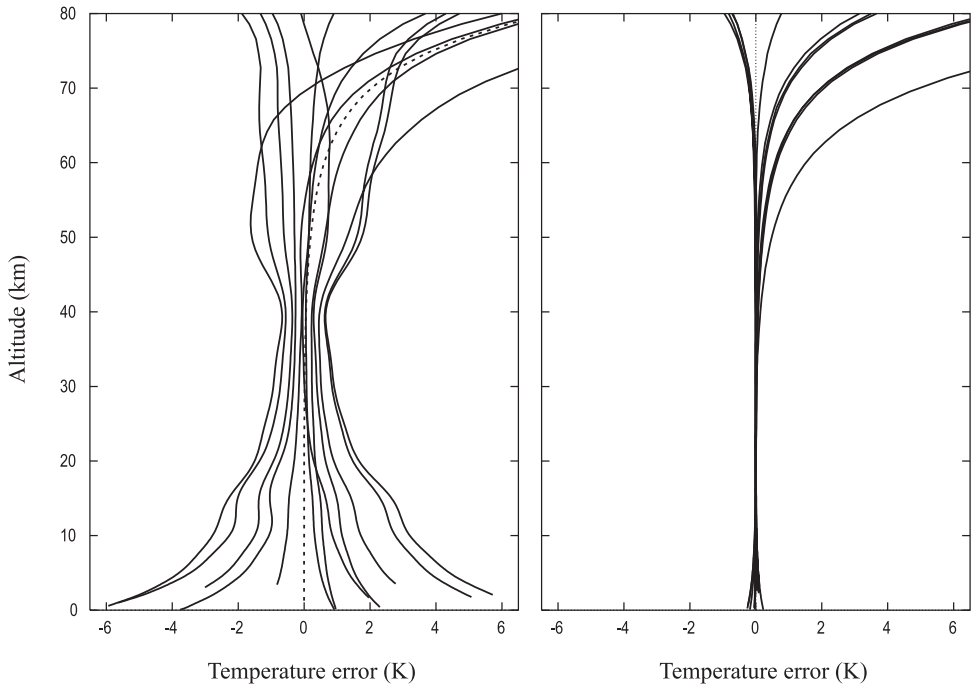

Figure 4.2 a) The retrieved temperature errors as a function of altitude for different simulated occultations. All retrievals assumed global spherical symmetry. The broken curve is a retrieval of synthetic data where the Earth was spherical in the forward modeling, and the solid curves are retrievals of synthetic data where the Earth's shape was an ellipsoid in the forward modeling. **b)** Retrieval errors for the same simulated occultations, but the temperatures are retrieved after correction of bending angles and impact parameters [*Syndergaard*, 1998].

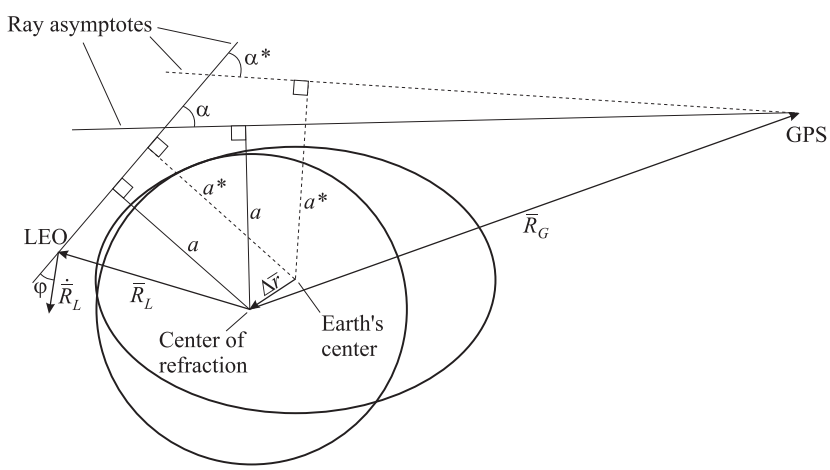

Figure 4.3 Cross section, in a meridian plane, of the oblate Earth and a tangential sphere (exaggerated). The origin of the sphere is a better approximation to the local center of refraction than the Earth's center. Using the Earth's center as the center of refraction in the retrieval will generally result in a wrong bending angle, $\alpha*$ and impact parameter $a*$ [*Syndergaard*, 1998].

accuracy at the ground (Figure 4.2b).

It is also shown in the paper that the orientation of the occultation plane has to be taken into account in the correction procedure if pressure profiles are to be retrieved to better than 0.4% accuracy.

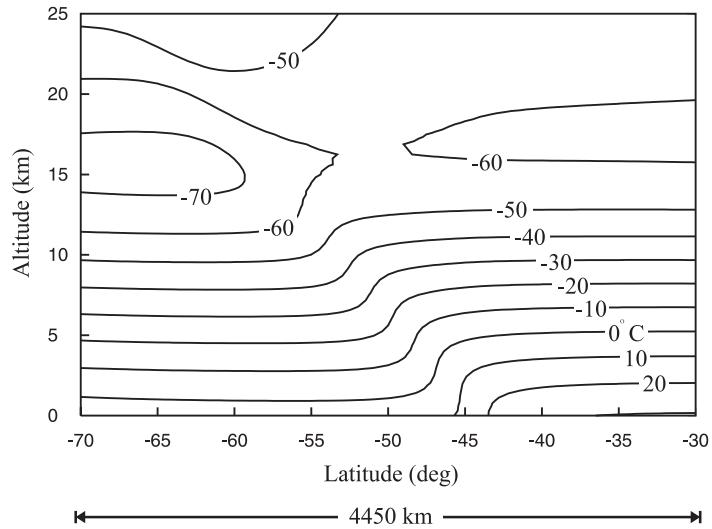

Figure 4.4 Cross section of a model temperature field of a severe frontal system. The slope of the front is 1 %, and the maximum gradient at the surface is 5 °C/100 km. Isotherms are in °C [*Syndergaard*, 1999a].

4.2.2 Atmospheric Frontal System (extension of section 5 in the paper in Appendix C.3)

To test the spherical symmetry assumption, simulations have been performed using 3D ray-tracing through a model of a severe frontal system. The model has been constructed from basic meteorological relations like Poisson's equation and the hydrostatic equilibrium assumption. In Appendix B the refractivity structure across the frontal zone is derived. The temperature field related to the front is shown in Figure 4.4. For simplicity, in the simulations the front is directed so that the temperature gradient lies in a meridian plane. To simulate a worst case scenario, the difference between the warm and the cold sides of the front at the surface has been set to about 25 °C. Such differences might be found at mid latitudes over continents during the winter [*Hardy et al.*, 1994]. The model is based on calculations excluding the water vapor contribution. *Hardy et al.* [1994] performed a similar case study using a more realistic model including the water vapor, but only presenting a single result. Here we shall go a bit further and look at different cases. Excluding the water vapor is no serious violation in favor of the method. On the contrary, in a real frontal system the refractivity may not vary much across the front because the dry and the moist refractivity terms tend to cancel, understood in the way that the cold side is denser but contains less water vapor than the warm side [*Hardy et al.*, 1994]. In Figure 4.4 the temperature gradients are produced solely by the dry refractivity term (1.6).

In the forward ray-tracing modeling, three different cases of occultations going through the frontal system have been simulated, aligning the rays approximately along the meridian: Case 1, where the base of the front has been placed right in front of the tangent points. Case 2, where the base of the front has been placed 5 degrees north of the tangent points. Case 3, where the base of the front has been placed 10 degrees north of the tangent points. In Figure 4.5 the placement of the front in each of these three cases is illustrated. The left figure shows the ray paths and the frontal bases in a longitude-latitude plot. The three figures at the right show the situations in latitude-

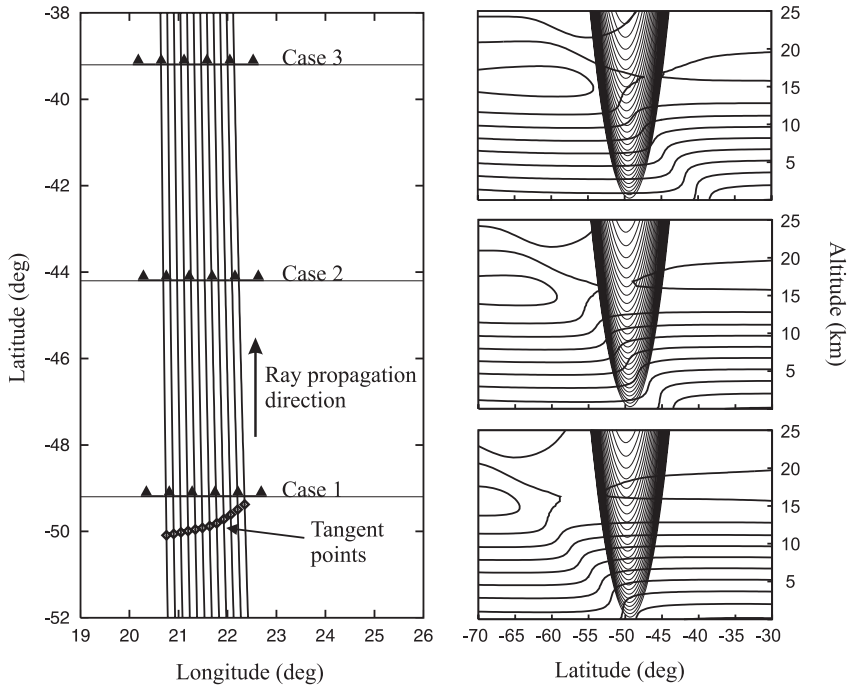

Figure 4.5 Left) Ray paths in a longitude-latitude plot. The simulation of rays are based on a real set of GPS/MET orbit ephemerides. Only a few rays out of about 3000 are shown. The left most ray corresponds to a ray tangent altitude of about 100 km, and the right most ray has its tangent point close to the surface. The drift of the tangent points are shown as diamonds. The three cases of placing the base of the front are indicated as lines with triangles. Right) Each of the three cases in a latitude-height plot, with rays (every 50th ray) superimposed on the temperature fields [*Syndergaard*, 1999a].

height plots. Because of the Earth's curvature, the almost straight rays (the bending angle close to the surface is about 1 degree and bending towards the Earth) become convex curves in the three small panels to the right in Figure 4.5. Such figures are also an excellent illustration of the spatial resolution of the method. In principle, the horizontal resolution defined by (2.3) corresponds to twice the horizontal distance between the lowest point on a ray and the neighboring ray, except that the vertical distance between rays in Figure 4.5 is not exactly the same as the first Fresnel diameter (see also [*Kursinski et al.*, 1997]).

For each of the three cases, about 3000 samples of synthetic phase data (50 Hz sampling rate) where calculated, covering the altitude range 0–100 km. Bending angles and the corresponding impact parameters were obtained, and the procedure outlined in Section 1.5 was then used to calculate a retrieved temperature profile. A model temperature profile was extracted from the corresponding model field of Figure 4.5. The location of the model profile was taken as the latitude and longitude of the point closest to the Earth's center on that line connecting the GPS- and the LEO satellite which was tangent to the Earth's surface. This gives a profile close to the set of tangent points shown in the left part of Figure 4.5. Figure 4.6 shows the retrieved profile and the corresponding "true" model profile for case 2. The signature of the front is seen as a decrease in temperature lapse rate around 6 km altitude, and generally the whole profile shifts from being "warm" above 16 km to become "cold" close to the surface. The retrieved temperature profile follows the "true" one remarkably well, but underestimates slightly

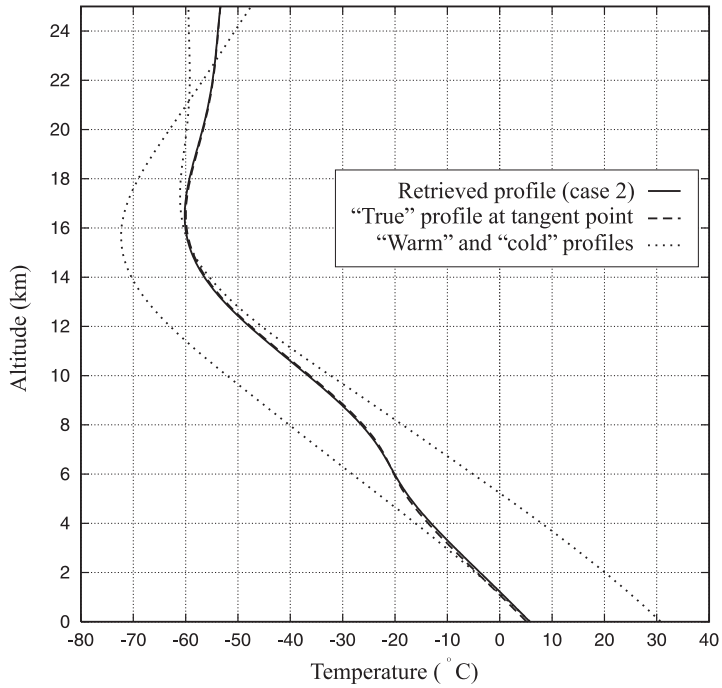

Figure 4.6 Retrieved (solid) and "true" (dashed) temperature profiles as a function of the altitude in the front (case 2). Also shown for comparison are the "true" profiles at the warm and the cold sides of the front far from the tangent points.

the change in lapse rate around 6 km. Consequently the temperature is overestimated above and underestimated below this altitude. However, Figure 4.6 gives a good picture of the strength of the method, even in cases where the spherical symmetry assumption is seriously violated. For comparison the profiles at the warm and the cold sides of the front are also shown in Figure 4.6. The reason why it works so well can be better understood when looking at Figure 4.5 (right). Because of the Earth's sphericity, the rays do not penetrate much of the horizontal structure in the lower atmosphere on either side of the profile location. The rays sort of dip down like the point of a knife and "taste" the atmosphere in the vicinity of the tangent points. On top of that, for a given ray, the majority of the measured effect comes from the atmosphere at the perigee of the ray. A very strong signature of an upper-level front in the GPS/MET data has been investigated in detail by *Kuo et al.* [1998].

To get a better picture of the errors, the difference between the retrieved temperature profile and the model temperature profile in each of the three cases are plotted in Figure 4.7. It is seen that the errors are of the order of 0.5 °C, and in the worst case, which turned out to be case 1, the error is still less than 2 °C.

The retrieved temperature profiles were also compared with profiles extracted from the model field at the exact positions of the tangent points. The observed differences were of the same order as those shown in Figure 4.7, although case 2 showed an error as large as case 1, being about 1.5 °C. In the above numerical experiments the frontal slope was 1 % which is a typical value in the real atmosphere. However, close to the surface the slope may become larger [*Gurvich and Sokolovskiy*, 1985]. Increasing the frontal slope to 5 % in case 1, resulted in somewhat larger errors (mostly above 4 km, though still less than 2 °C), confirming similar results by *Gurvich and Sokolovskiy* [1985] and

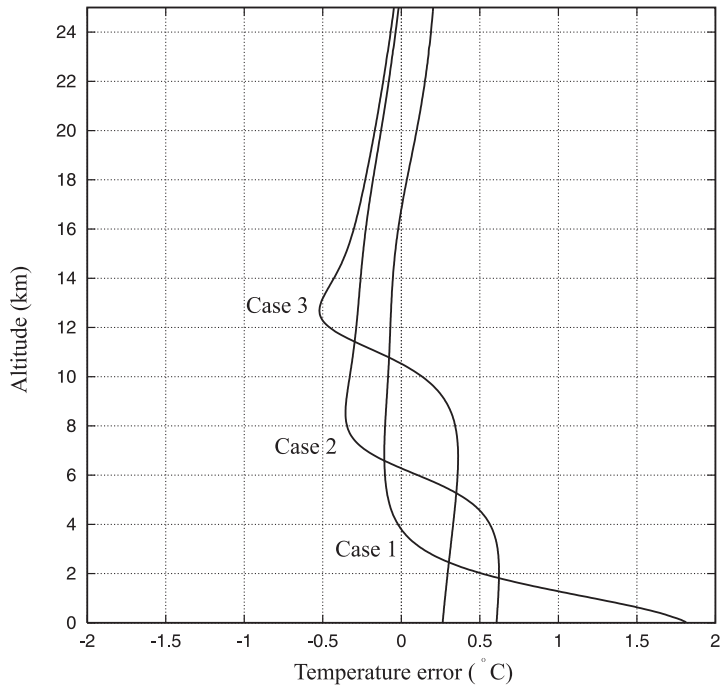

Figure 4.7 Retrieval errors for each of the three cases as described in the text [*Syndergaard*, 1999a].

Høeg et al. [1998].

Since the temperature profiles are derived via the hydrostatic integration of the refractivity, errors in refractivity, pressure, and temperature does not map as a one to one relationship. There will be differences in the error behavior as a function of height. Also, in a weather front the strict assumption of hydrostatic equilibrium may be questionable. Here we have only concentrated on the temperature errors, though pressure and refractivity errors may be of equal relevance. The order of magnitude of the relative errors, however, is generally the same.

Chapter 5

Conclusions and Prospects

The GNSS radio occultation technique for the retrieval of terrestrial atmospheric parameters is rather new. So far the only proof-of-concept experiment has been the GPS/MET which was launch in 1995. Consequently, work on assessing errors and improving the retrieval algorithms is still ongoing.

In this work, different subjects connected to the retrieval of atmospheric parameters from single occultations were studied. Four subjects were addressed in detail: Random error propagation, ionosphere calibration, impact of Earth's oblateness, and assessment of errors due to sharp horizontal gradients like a weather front. Below follow the conclusions from each of these studies, and at the end a few remarks about the prospects of the GNSS radio occultation technique are given.

5.1 Conclusions

5.1.1 Random Error Propagation

Propagation of random, Gaussian-distributed errors through the retrieval procedure from measured phases to dry temperature profiles, has been carried out both analytically and by simulations. Using covariance analysis, the analytical study showed, step by step, how standard deviations and vertical (time-tagged) error correlations come out for the smoothed excess phase, excess Doppler, bending angle, refractivity, dry pressure, and dry temperature, when assuming a constant initial standard deviation of 3 mm on the raw 50 Hz phase measurements.

Care has to be taken in the steps, excess Doppler $\rightarrow$ bending angle and bending angle $\rightarrow$ refractivity. These steps include a change in the independent variable (time $\rightarrow$ impact parameter and impact parameter $\rightarrow$ tangent radius, respectively) which, due to bending, is not linear in the lower atmosphere. Most influence has the former step. In this step, the error in impact parameter is "transmitted" to an additional error in bending angle. This seems appropriate since the impact parameter is regarded as an independent variable in the Abel integration when solving for the refractivity. The effect on the bending angle profile, and subsequently the refractivity profile, is an increase in standard deviation at lower altitudes compared to higher altitudes. For the bending angle profile, the standard deviation is about one order of magnitude larger close to the surface than at high altitudes. The effect on refractivity is smaller, since the defocusing effect counteracts in the Abel integration giving a net decrease in the standard deviation at low altitudes.

The smoothing step and especially the differentiation step results in negative error correlations between near neighboring points (heights), but no error correlation over far vertical distances larger than the vertical resolution. These characteristics are carried on to the bending angle and the refractivity. Only very small error correlations over far vertical distances are seen in the refractivity. However, if one, erroneously, assume the bending angle errors to be uncorrelated in the vertical, the resulting error correlation in retrieved refractivity has a totally different character showing relatively large positive far-distance vertical error correlations. This is due to the accumulative nature of the Abel integration, making errors at higher altitudes propagate to lower altitudes. When bending angles are correlated with a negative correlation between near neighboring heights, errors add more destructively resulting in only small far-distance vertical error correlations.

Applying less smoothing to the excess phase gives a better vertical resolution manifested in a more narrow vertical error correlation between near neighboring heights. The error propagation through the Abel integration depends highly on this vertical resolution: When applying more smoothing to the excess phase, one does not gain much in terms of smaller errors in the refractivity, compared to the gain in terms of smaller errors in the bending angle.

The hydrostatic integration results in very large vertical error correlations in the pressure and temperature over the whole vertical range 0–80 km. However, for temperature, this is only true when the hydrostatic integration is performed from a very high altitude (110 km). In reality, this is not possible, and use of a model bending angle at high altitudes and perhaps applying statistical optimization is necessary. Applying statistical optimization above 60 km, results in only small far-distance vertical error correlations in the temperature.

Because the refractivity *decreases* almost exponentially with altitude, the standard deviation of the temperature *increases* almost exponentially with altitude. At a given altitude, a simple relationship between standard deviations of the excess phase and the temperature was found numerically. This was expressed in an empirical formula relating the standard deviation of the excess phase and the standard deviation of the temperature as a function of altitude. The relationship depends on the smoothing applied to the excess phase and whether statistical optimization of bending angles is applied. The best results are obtained using a high degree of smoothing together with a statistical optimization approach. However, in order to preserve the highest vertical resolution possible, less smoothing of the excess phase is desirable at low altitudes, where the influence of random errors is small. The best thing to do is probably to use a low degree of smoothing at low altitudes (e.g., below 30 km) and a high degree of smoothing at higher altitudes.

Finally, it should be emphasized that the results obtained are based on several assumptions: 1) A constant standard deviation of the excess phase error. Real data will have larger errors at lower altitudes than at higher altitudes. 2) A constant degree of smoothing at all heights. Other smoothing approaches than the one discussed here may be applied. 3) Effects of the ionosphere calibration have been disregarded. This will result in an amplification of uncorrelated errors by a factor of about three, but also residual ionospheric effects in terms of a bias may remain and influence the accuracy and error correlation above the tropopause. 4) The retrieval is done within the geometrical optics approximation. Applying the diffraction correction/back propagation method [*Karayel and Hinson*, 1997; *Gorbunov and Gurvich*, 1998b] or the Fresnel

diffraction theory [*Melbourne et al.*, 1994; *Mortensen and Høeg*, 1998] is a different story involving also the amplitude of the signal. 5) Random errors are assumed not to be too large so that the propagation analysis can be linearized. Especially the "transmission" procedure of impact parameter errors in the troposphere and the final step to obtain the temperature errors, relies on this assumption. 6) Water vapor pressure is assumed to be negligible. However, the temperature results still give a good indication of the relative accuracy obtainable in the lower troposphere, even in the presence of water vapor. The bending angle and refractivity results are not affected by the violation of this assumption. 7) Systematic errors are eliminated. This assumption is violated for sure, especially in the lower atmosphere where horizontal inhomogeneities leak into the retrieval in terms of a bias due to the violation of the spherical symmetry assumption. Generally, error covariance matrices are relevant for assimilation of measurements into NWP models, but the error covariance matrices obtained here do not represent the real error covariance in the lower atmosphere because of this violation.

5.1.2 Ionosphere Calibration

[1] The results presented in the paper do not represent the first attempt in the literature to estimate the dispersion effects on the phase path observables in GPS occultation measurements. However, it has not previously been shown that the first order dispersion residual from the traditional dual-frequency combination is made up of two parts, a "major" and a "minor", of which the "major" part is directly related to the vertical gradients of the Satellite–Satellite Total Electron Content (S–S TEC), being available from the occultation measurements themselves. It is also the first time that an estimate of the second order dispersion effects has been derived and quantified.

The theoretical work here focused on expressing both the L1 and L2 phase paths along the imaginary LF path, using a transformation into the radial domain, assuming spherical symmetry. The results provide a mean to correct the residuals from the traditional dual-frequency combination, thereby obtaining an improved dual-frequency phase path correction method taking into account the dispersion effects as well as the second order effect from the Earth's magnetic field.

Within the limits of geometrical optics, this improved phase path correction method is at least as good as the existing, and widely used, bending angle correction method. The main difference between the two methods lies in the "minor" dispersion term, which contributes to an almost linear phase path trend below the E-layer. This trend, if not accounted for, maps into a bending angle residual which is in fact equivalent to the main residual obtained with the bending angle correction method.

Unfortunately, estimation of the "minor" dispersion term needs auxiliary information of, e.g., the vertical TEC above the occultation site. Having that, the "minor" dispersion term may be evaluated and removed to a large extent. However, this is only true under spherical symmetry conditions. In general, horizontal gradients in the ionosphere limits the correction accuracy, and if the occultation happens to be in a day-night transition zone, residuals of the order of a few centimeter may still remain using the improved phase path correction method. Such residuals map into bending angle residuals of the order of 10^{-7}rad. Occultations cutting through regions having other sharp horizontal gradients, like the equatorial anomaly or the auroral zone, can give similar residuals.

Numerical estimates, although based on simple modeling, indicate that the second

[1] This subsection follows the conclusion of the paper in Appendix C.1.

order residual stemming from the Earth's magnetic field, has very little influence on the bending angles. Compared to the phase path trend from the "minor" dispersion term and residual biases arising because of the violation of the spherical symmetry assumption, the influence from the geomagnetic field may probably be ignored in all cases.

A third frequency would enable a triplex-frequency phase path combination being almost insensitive to ionospheric asymmetry conditions. Below the bottom of the ionosphere, such a combination would reduce phase path residuals to the millimeter level, and bending angle biases would practically be eliminated. Actually, the "magnetic" term could then become the limiting systematic error, if not accounted for. The third frequency should be situated far from the existing L1 and L2 frequencies to avoid too much amplification of uncorrelated statistical errors.

Sharp vertical gradients at the bottom of the ionosphere attributed to sporadic E-layers occur frequently, and will cause scintillations in the phase and amplitude occultation data [*Hajj and Romans*, 1998]. Such scintillations, caused by diffraction and multi-path propagation, and thus violating the geometrical optics assumption, will produce large errors in the ionosphere corrected phase path. Such effects could be reduced or eliminated using the diffraction correction/back-propagation method applied to the ionosphere (M. E. Gorbunov, presented at GNSS workshop in Hamburg, 1998), but usually the influence of these disturbances is at such high altitudes that this part of the data may be disregarded for the retrieval of neutral atmospheric parameters.

It should be emphasized that the method of diffraction correction/back-propagation [*Karayel and Hinson*, 1997; *Gorbunov and Gurvich*, 1998b] cannot be used in conjunction with an ionosphere phase path correction method, since diffraction corrected bending angles for each of the GPS signals are estimated before ionosphere correction is performed, then using the bending angle correction method.

For any ionosphere correction method, the mapping of residual bending angle errors into retrieved refractivity, pressure, and temperature, highly depends on the technique used for further data processing. Theoretically, the bending angle profile to infinity altitude is required in the integration of bending angles to obtain the refractivity profile. Obviously this is not available, and in practice extrapolation and/or use of model bending angles above some altitude is necessary in order to get accurate and useful refractivities at the highest altitudes.

Measurement noise is yet another obstacle in practice, and indeed a serious one. Some kind of filtering of the phase-time series is needed before further processing into Doppler shifts and bending angles. Still, bending angles will inevitably have random fluctuations which blow up the relative error at some high altitude and above. This calls for statistical optimization techniques where a model bending angle profile gradually replaces the data profile above some specified altitude depending on the noise level. For the data available from the GPS/MET experiment an altitude of 40–50 km seems to be appropriate [*Hocke*, 1997; *Gorbunov and Gurvich*, 1998a]—an altitude much lower than the altitude where ionosphere residuals become significant. However, future instrumentation will probably supply data of a better quality and reduced noise level [*Kursinski et al.*, 1997], allowing the statistical optimization level to be raised into the height region where ionosphere residuals may become the limiting error source.

5.1.3 Impact of Earth's Oblateness

[2] The planetary oblateness of the Earth, if not accounted for, may cause a bias in retrieved atmospheric profiles obtained from terrestrial radio occultation measurements. The bias is dependent on the geometry of the specific occultation and the geographic latitude of the limb. Other minor dependencies are the relative velocity of the satellites and the features on the temperature profile itself. It was also found that the bias was sensitive to the choice/calculation of the exact latitude of the profile location.

Numerical simulations show a minimum in the temperature bias at about 40 km altitude. Below this altitude the bias increases, and may, at or around mid-latitudes, be as large as 3 K at 10 km altitude and 6 K at the ground. The sign of the bias depends on the ray direction at the profile location: rays traveling towards higher latitudes result in a positive bias, and vice versa. The origin of the bias is a wrong estimate of bending angles and impact parameters due to an incorrect assumption of global spherical symmetry with respect to Earth's center.

A way of correcting for the Earth's oblateness in the retrieval is performed by referring all satellite positions to a local center of refraction, defined by the origin of a sphere, tangential to the ellipsoid, at the profile location. The orientation of the occultation plane has to be taken into account, defining the radius of the sphere, in order to retrieve accurate refractivity and pressure profiles. The temperature retrievals obtained with the correct method showed only small errors, less than 0.1 K at the ground, while the fractional errors in refractivity and pressure were less than 0.05 %.

5.1.4 Atmospheric Frontal System

Even though the retrieval of atmospheric parameters of GNSS occultation data is based on the spherical symmetry assumption, errors in retrieved temperature in a region of a sharp front is not very large. Ray-tracing simulations through model of the refractivity field across a frontal zone, show that even under severe conditions retrieved errors do not exceed 2 °C. This result was obtained with a front having a difference of about 25 °C between the cold and the warm side. Although based on a simplified theory, excluding the contribution from water vapor, the magnitude of the resulting refractivity gradients may be considered as being representative of expected gradients in a severe frontal system.

One of the reasons for the relatively small errors compared to the temperature difference between the two sides, is that the occultation rays, because of the sphericity of the Earth, does not penetrate regions far from the tangent point. To this comes that for a given ray, the majority of the measured effect is concentrated around the ray perigee. The results demonstrate the strength and the potentials of the GNSS radio occultation method, even when the spherical symmetry assumption is seriously violated in the retrieval of individual temperature profiles.

5.2 Prospects

The GNSS radio occultation technique has proven its worth with the GPS/MET experiment. With the limited amount of data available from the GPS/MET experiment it is not possible in general to combine multiple occultation events. Events have to

[2] This subsection follows the conclusion of the paper in Appendix C.2.

be treated separately. However, in the near future, GPS receivers will be flown on a multitude of Earth observation satellites. This opens up for the possibility of combining measurements into a larger scheme. *Gorbunov et al.* [1996b] have already analyzed the potential of having 100 LEO satellites receiving signals from 18 GNSS satellites in 3 polar orbits. Taking into account large-scale horizontal variations, they show that it is possible to solve for the global refractivity field with a spatial and temporal resolution comparable to the resolution of NWP models.

The ultimate use, though, is probably to assimilate measurements into NWP models taking into account other data sources as well as the background model field. For this project, one of the most challenging tasks is to give a good description of the errors and correlations of the retrieved data. At present, considerable efforts are made in the area, and discussions of whether to assimilate refractivity or bending angles are still ongoing [*Eyre and Offiler*, 1998; *Zou et al.*, 1998a, b].

Also for monitoring of climate change, radio occultation data can become valuable. *Yuan et al.* [1993] simulated the change in propagation delay on GPS occultation links, as a result of global warming. The potentials have also been discussed in detail by *Kursinski et al.* [1997].

Finally it should be mentioned that the GNSS occultation technique also has a great potential within the area of ionospheric tomography. Combining data with ground based measurements, it is possible to obtain a much better vertical resolution in tomographic models than using only the ground based data [*Hajj et al.*, 1994; *Leitinger et al.*, 1997; *Rius et al.*, 1997, 1998].

Acknowledgments

I would like to acknowledge my three advisors Per Høeg, Danish Meteorological Institute (DMI), Carl Christian Tscherning, and Klaus Mosegaard, Niels Bohr Institute for Astronomy, Physics and Geophysics, Geophysical Department, University of Copenhagen (NBIfAFG), for their support and advice.

Part of the research was carried out at the University of Arizona, Tucson, Arizona, and I would like to express my gratitude to Dr. Benjamin Herman at the Department of Atmospheric Sciences for inviting me to come to Tucson, for his hospitality, and for his advice. I also gratefully acknowledge Nancy Emptage and Sherry Rollins for their help with many practical affairs. I honestly want to thank all the people that I came to know in Tucson, for their help and their friendship. A very sincere thank goes to Cynthia Malbrough and her family.

I am most grateful to Georg B. Larsen, DMI, for many fruitful discussions during the work and for useful comments to the manuscript. I thank Bjarne Amstrup, DMI, for his thorough reading and list of corrections to the grammar and misprints in the first version of the thesis. Also many thanks to my other colleagues at DMI for help and cooperation. The administrative staff at the research department at DMI is greatly acknowledged for their help with numerous things.

A very special thank is due to my dearest friend Helle Wagner for her encouragements and for listening to my complaints in moments of despair.

I also wish to thank the people in the GPS/MET team at UCAR, Boulder, Colorado, for providing the occultation data as well as the correlative radiosonde- and numerical weather analyses data used in this work.

The research was funded by a grant from the Danish Space Board, and I would like to express my appreciation to Per Høeg for his help in raising the funding.

References

Ahmad, B., and G. L. Tyler, The two-dimensional resolution kernel associated with retrieval of ionospheric and atmospheric refractivity profiles by Abelian inversion of radio occultation phase data, *Radio Science*, *33*, 129–142, 1998a.

Ahmad, B., and G. L. Tyler, Systematic errors in atmospheric profiles obtained from Abelian inversion of radio occultation data: Effects of large-scale horizontal gradients, *Journal of Geophysical Research - Atmospheres*, 1998b, submitted.

Aki, K., and P. G. Richards, *Quantitative Seismology*, vol. II, W. H. Freeman and Company, San Francisco, 1980.

Antikidis, J.-P., D. Fournier, and L. Gaillard, Instrument catalogue, CNES web site, http://sads.cnes.fr/ceos/cdrom-98/ceos1/instrum/instr31.htm, 1998.

Belloul, M. B., and A. Hauchcorne, Effect of periodic horizontal gradients on the retrieval of atmospheric profiles from occultation measurements, *Radio Science*, *32*, 469–478, 1997.

Bertiger, W., and S.-C. Wu, Single frequency GPS orbit determination for low earth orbiters, Paper presented at the National Technical Meeting, Institute of Navigation, Jan. 22-24, 1996, Santa Monica, CA, 1996.

Bertiger, W., L. Romans, R. Muellerschoen, S. Wu, G. Hajj, R. Kursinski, S. Leroy, and T. Schofield, A calibration system for GPS radio occultation experiments, Presented at the Second URSI international Workshop for Working Group AFG1, Feb. 22-23, 1996, Tucson, AZ, 1996.

Bevis, M., S. Businger, S. Chiswell, T. A. Herring, R. A. Anthes, C. Rocken, and R. H. Ware, GPS meteorology: Mapping zenith wet delays onto precipitable water, *Journal of Applied Meteorology*, *33*, 379–386, 1994.

Budden, K. G., *The propagation of radio waves*, Cambridge University Press, Cambridge, 1985.

DMI, and TERMA, Atmospheric sounding with GNSS occultation: Detailed definition and revision of instrument requirement specifications, *Technical note under ESA/ESTEC Contract No. 11818/96/NL/CN, Internal No. CRI/ATMSOU/TN/1*, TERMA Elektronik AS, Birkerød, Denmark, 1998.

Eyre, J. R., and D. Offiler, GNSS for operational meteorology and climatology: Radio occultation measurements in operational meteorology, *Report under ESA/ESTEC*

Contract No. 11930/96/NL/CN, Internal No. OMC-UKMO-TN1, Meteorological Office, Bracknell, UK, 1998.

Feng, D., B. Herman, M. Exner, W. Schreiner, R. McCloskey, and D. Hunt, Preliminary results from the GPS/MET atmospheric remote sensing experiment, in *GPS Trends in Precise Terrestrial, Airborne, and Spaceborne Applications*, vol. 115 of *International Association of Geodesy Symposia*, pp. 139–143, Springer-Verlag, 1995.

Feng, D. D., and B. M. Herman, Remotely sensing the Earth's atmosphere using the Global Positioning System (GPS)—the GPS/MET data analysis, *Journal of Atmospheric and Oceanic Technology*, 1998, in press.

Fischbach, F. F., A satellite method for pressure and temperature below 24 km, *Bulletin of American Meteorological Society*, *46*, 528–532, 1965.

Fishbein, E. F., R. E. Cofield, L. Froidevaux, R. F. Jarnot, T. Lungu, W. G. Read, Z. Shippony, J. W. Waters, I. S. McDermid, T. J. McGee, U. Singh, M. Gross, A. Hauchcorne, P. Keckhut, M. E. Gelman, and R. M. Nagatani, Validation of UARS Microwave Limb Sounder temperature and pressure measurements, *Journal of Geophysical Research*, *101*, 9983–10,016, 1996.

Fjeldbo, G., A. J. Kliore, and V. R. Eshleman, The neutral atmosphere of Venus as studied with the Mariner V radio occultation experiments, *The Astronomical Journal*, *76*, 123–140, 1971.

Fjeldbo, G., A. Kliore, B. Seidel, D. Sweetnam, and P. Woiceshyn, The Pioneer 11 radio occultation measurements of the Jovian ionosphere, in *Jupiter: Studies of the Interior, Atmosphere, Magnetosphere and Satellites*, edited by T. Gehrels, pp. 238–246, University of Arizona Press, Tucson, Arizona, 1976.

Gorbunov, M. E., and A. S. Gurvich, Algorithms of inversion of Microlab-1 satellite data including effects of multipath propagation, *International Journal of Remote Sensing*, *19*, 2283–2300, 1998a.

Gorbunov, M. E., and A. S. Gurvich, Microlab-1 experiment: Multipath effects in the lower troposphere, *Journal of Geophysical Research*, *103*, 13,819–13,826, 1998b.

Gorbunov, M. E., A. S. Gurvich, and L. Bengtson, Advanced algorithms of inversion of GPS/MET satellite data and their application to reconstruction of temperature and humidity, *Report No. 211*, Max-Planck-Institute for Meteorology, Hamburg, Germany, 1996a.

Gorbunov, M. E., S. V. Sokolovsky, and L. Bengtsson, Space refractive tomography of the atmosphere: Modeling of direct and inverse problems, *Report No. 210*, Max-Planck-Institute for Meteorology, Hamburg, Germany, 1996b.

Gorbunov, M. Y., Solution of inverse problems of remote atmospheric refractometry on limb paths, *Izvestia, Atmospheric and Oceanic Physics*, *26*, 86–91, 1990.

Gurvich, A. S., and S. V. Sokolovskiy, Reconstruction of a pressure field by remote refractometry from space, *Izvestiya, Atmospheric and Oceanic Physics*, *21*, 7–13, 1985.

Hajj, G. A., and L. J. Romans, Ionospheric electron density profiles obtained with the Global Positioning System: Results from the GPS/MET experiment, *Radio Science*, *33*, 175–190, 1998.

Hajj, G. A., R. Ibañez-Meier, E. R. Kursinski, and L. J. Romans, Imaging the ionosphere with the global positioning system, *International Journal of Imaging Systems and Technology*, *5*, 174–184, 1994.

Hajj, G. A., E. R. Kursinski, W. I. Bertiger, S. S. Leroy, T. K. Meehan, L. J. Romans, and J. T. Schofield, Initial results of GPS-LEO occultation measurements of Earth's atmosphere obtained with the GPS/MET experiment, in *GPS Trends in Precise Terrestrial, Airborne, and Spaceborne Applications*, vol. 115 of *International Association of Geodesy Symposia*, pp. 144–153, Springer-Verlag, 1995.

Haltiner, G. J., and F. L. Martin, *Dynamical and Physical Meteorology*, McGraw Hill, New York, 1957.

Han, S., and C. Rizos, Comparing GPS ambiguity resolution techniques, *GPS World*, *8*, 54–60, 1997.

Hansen, P. C., *Rank-Deficient and Discrete Ill-Posed Problems: Numerical Aspects of Linear Inversion*, SIAM monographs on mathematical modeling and computation, SIAM, Philadelphia, 1998.

Hardy, K. R., G. A. Hajj, and E. R. Kursinski, Accuracies of atmospheric profiles obtained from GPS occultations, *International Journal of Satellite Communications*, *12*, 463–473, 1994.

Haskell, B. J., and C. S. Mikkelsen, GOES-I/M Sounder: Products, resolution, and accuracy, NASA/GOES web site, http://goes1.gsfc.nasa.gov/instrume.htm, 1999.

Hervig, M. E., J. M. Russell III, L. L. Gordley, S. R. Drayson, K. Stone, R. E. Thompson, M. E. Gelman, I. S. McDermid, A. Hauchecorne, P. Keckhut, T. J. McGee, U. N. Singh, and M. R. Gross, Validation of temperature measurements from the Halogen Occultation Experiment, *Journal of Geophysical Research*, *101*, 10,277–10,285, 1996.

Hocke, K., Inversion of GPS meteorology data, *Annales Geophysicae*, *15*, 443–450, 1997.

Høeg, P., A. Hauchcorne, G. Kirchengast, S. Syndergaard, B. Belloul, R. Leitinger, and W. Rothleitner, Derivation of atmospheric properties using a radio occultation technique, *Scientific Report 95-4*, Danish Meteorological Institute, Copenhagen, Denmark, 1996.

Høeg, P., G. B. Larsen, H.-H. Benzon, J. Grove-Rasmussen, S. Syndergaard, M. D. Mortensen, J. Christensen, and K. Schultz, GPS atmosphere profiling methods and error assessments, *Scientific Report 98-7*, Danish Meteorological Institute, Copenhagen, Denmark, 1998.

Holton, J. R., *An Introduction to Dynamic Meteorology*, 3rd ed., Academic Press, Inc., San Diego, CA, 1992.

Hopkins, E. J., Radiosondes as upper air probes, Ross Computational Resources web site, http://earthlab.meteor.wisc.edu/~hopkins/rockets/raob.htm, 1996.

Ilyushin, Y. A., and O. A. Terekhova, Approximate technique for limb sounding data interpretation, Paper presented at the EGS XXIII General Assembly, 20-24 April, Nice, France, 1998.

Karayel, E. T., and D. P. Hinson, Sub-Fresnel-scale vertical resolution in atmospheric profiles from radio occultation, *Radio Science*, *32*, 411–423, 1997.

Kirchengast, G., Orbit quality requirements for spaceborne atmospheric sounding using GNSS, Presented at the EGS XXIII General Assembly, 20-24 April, Nice, France, 1998.

Kliore, A., D. L. Cain, G. S. Levy, V. R. Eshleman, G. Fjeldbo, and F. D. Drake, Occultation experiment: Results of the first direct measurement of Mars's atmosphere and ionosphere, *Science*, *149*, 1243–1248, 1965.

Kliore, A. J., and P. M. Woiceshyn, Structure of the atmosphere of Jupiter from Pioneer 10 and 11 radio occultation measurements, in *Jupiter: Studies of the Interior, Atmosphere, Magnetosphere and Satellites*, edited by T. Gehrels, pp. 216–237, University of Arizona Press, Tucson, Arizona, 1976.

Kornblueh, L., M. Gorbunov, and L. Bengtsson, GNSS for operational meteorology and climatology: Applications to climatology and atmospheric process studies, *Report under ESA/ESTEC Contract No. 11930/96/NL/CN, Work Package 4*, Max-Planck-Institute for Meteorology, Hamburg, Germany, 1997.

Kuo, Y.-H., X. Zou, S. J. Chen, W. Huang, Y.-R. Guo, R. A. Anthes, M. Exner, D. Hunt, C. Rocken, and S. Sokolovskiy, A GPS/MET sounding through an intense upper-level front, *Bulletin of the American Meteorological Society*, *79*, 617–626, 1998.

Kursinski, E. R., The GPS radio occultation concept: Theoretical performance and initial results, Ph.D. thesis, California Institute of Technology, Pasadena, California, 1997.

Kursinski, E. R., G. A. Hajj, W. I. Bertiger, S. S. Leroy, T. K. Meehan, L. J. Romans, J. T. Schofield, D. J. McCleese, W. G. Melbourne, C. L. Thornton, T. P. Yunck, J. R. Eyre, and R. N. Nagatani, Initial results of radio occultation observations of Earth's atmosphere using the Global Positioning System, *Science*, *271*, 1107–1110, 1996.

Kursinski, E. R., G. A. Hajj, J. T. Schofield, R. P. Linfield, and K. R. Hardy, Observing Earth's atmosphere with radio occultation measurements using the Global Positioning System, *Journal of Geophysical Research*, *102*, 23,429–23,465, 1997.

Leitinger, R., H.-P. Ladreiter, and G. Kirchengast, Ionosphere tomography with data from satellite reception of Global Navigation Satellite System signals and ground reception of Navy Navigational Satellite System signals, *Radio Science*, *32*, 1657–1669, 1997.

Lemoine, F. G., D. D. Rowlands, J. A. Marshall, E. C. Pavlis, and J. C. Chan, Precision orbit determination with GPS/MET, Presented at the Second URSI international Workshop for Working Group AFG1, Feb. 22-23, 1996, Tucson, AZ, 1996.

Lindal, G. F., The atmosphere of Neptune: An analysis of radio occultation data acquired with Voyager 2, *The Astronomical Journal*, *103*, 967–982, 1992.

Lipa, B., and G. L. Tyler, Statistical and computational uncertainties in atmospheric profiles from radio occultation: Mariner 10 at Venus, *Icarus*, *39*, 192–208, 1979.

Lusignan, B., G. Modrell, A. Morrison, J. Pomalaza, and S. G. Ungar, Sensing the Earth's atmosphere with occultation satellites, *Proceedings of the IEEE*, *57*, 458–467, 1969.

Mathiesen, B., Error analysis tutorials: The vocabulary of error analysis, University of Michigan web site, http://www.physics.lsa.umich.edu/IP-LABS/Errordocs/vocaberr.html, 1997.

Melbourne, W. G., E. S. Davis, C. B. Duncan, G. A. Hajj, K. R. Hardy, E. R. Kursinski, T. K. Meehan, L. E. Young, and T. P. Yunck, The application of spaceborne GPS to atmospheric limb sounding and global change monitoring, *JPL-Publication 94-18*, Jet Propulsion Laboratory, California Institute of Technology, Pasadena, California, 1994.

Mortensen, M. D., and P. Høeg, Inversion of GPS occultation measurements using Fresnel diffraction theory, *Geophysical Research Letters*, *25*, 2441–2444, 1998.

Mortensen, M. D., R. P. Linfield, and E. R. Kursinski, Vertical resolution approaching 100 m for GPS occultations of the Earth's atmosphere, *Radio Science*, 1999, submitted.

O'Sullivan, D. B., B. M. Herman, and D. Feng, Retrieval of water vapor profiles from GPS/MET radio occultations, 1999, to be submitted.

Phinney, R. A., and D. L. Anderson, On the radio occultation method for studying planetary atmospheres, *Journal of Geophysical Research*, *73*, 1819–1827, 1968.

Rangaswamy, S., Recovery of atmospheric parameters from the APOLLO/SOYUZ-ATS-F radio occultation data, *Geophysical Research Letters*, *3*, 483–486, 1976.

Rieder, M., Advanced physical-statistical retrieval of humidity and temperature profiles from spaceborne downlooking microwave sounder data, Ph.D. thesis, Institut für Meteorologie und Geophysik, Karl-Franzens-Universität Graz, Graz, Austria, 1998.

Rius, A., G. Ruffini, and L. Cucurull, Improving the vertical resolution of ionospheric tomography with GPS occultations, *Geophysical Research Letters*, *24*, 2291–2294, 1997.

Rius, A., G. Ruffini, and A. Romeo, Analysis of ionospheric electron density distribution from GPS/MET occultations, *IEEE Transactions on Geoscience and Remote Sensing*, *36*, 383–394, 1998.

Rocken, C., R. Anthes, M. Exner, D. Hunt, S. Sokolovskiy, R. Ware, M. Gorbunov, W. Schreiner, D. Feng, B. Herman, Y.-H. Kuo, and X. Zou, Analysis and validation of GPS/MET data in the neutral atmosphere, *Journal of Geophysical Research*, *102*, 29,849–29,860, 1997.

Schreiner, B., GPS/MET orbit determination and excess phase processing, Presented at the Second URSI international Workshop for Working Group AFG1, Feb. 22-23, 1996, Tucson, AZ, 1996.

Seeber, G., *Satellite geodesy: foundations, methods, and applications*, de Gruyter, Berlin, Germany, 1993.

Smith, E. K., Jr., and S. Wientraub, The constants in the equation for atmospheric refractive index at radio frequencies, *Journal of Research of the National Bureau of Standards*, *50*, 39–41, 1953.

Smith, W. L., H. M. Woolf, C. M. Hayden, D. Q. Wark, and L. M. McMillin, The TIROS-N operational vertical sounder, *Bulletin of American Meteorological Society*, *60*, 1177–1187, 1979.

Sokolovskiy, S., and D. Hunt, Statistical optimization approach for GPS/MET data inversions, Presented at the Second URSI international Workshop for Working Group AFG1, Feb. 22-23, 1996, Tucson, AZ, 1996.

Steiner, A. K., G. Kirchengast, and H. P. Ladreiter, Inversion, error analysis, and validation of GPS/MET occultation data, *Annales Geophysicae*, *16*, 122–138, 1999.

Stewart, R. W., and J. S. Hogan, Error analysis for the Mariner-6 and -7 occultation experiments, *Radio Science*, *8*, 109–115, 1973.

Syndergaard, S., Modeling the impact of the Earth's oblateness on the retrieval of temperature and pressure profiles from limb sounding, *Journal of Atmospheric and Solar-Terrestrial Physics*, *60*, 171–180, 1998.

Syndergaard, S., Inversion of GPS occultation data for atmospheric profiling, in *Inverse Methods II*, Lecture Notes in Earth Sciences, Springer Verlag, 1999a, submitted.

Syndergaard, S., On the ionosphere calibration in GPS radio occultation measurements, *Radio Science*, 1999b, submitted.

Turchin, V. F., and V. Z. Nozik, Statistical regularization of the solution of incorrectly posed problems, *Izvestia Academy of Sciences SSSR, Atmospheric and Oceanic Physics, English Translation*, *5*, 14–18, 1969.

Twomey, S., *Introduction to the Mathematics of Inversion in Remote Sensing and Indirect Measurements*, Dover Publications, Inc., Mineola, New York, 1977.

Tyler, G. L., Radio propagation experiments in the outer solar system with Voyager, *Proceedings of the IEEE*, *75*, 1404–1431, 1987.

Vorob'ev, V. V., and T. G. Krasil'nikova, Estimation of the accuracy of the atmospheric refractive index recovery from Doppler shift measurements at frequencies used in the NAVSTAR system, *Physics of the Atmosphere and Ocean*, *29*, 602–609, 1994.

Ware, R., M. Exner, D. Feng, M. Gorbunov, K. Hardy, B. Herman, Y. Kuo, T. Meehan, W. Melbourne, C. Rocken, W. Schreiner, S. Sokolovskiy, F. Solheim, X. Zou, R. Anthes, S. Businger, and K. Trenberth, GPS sounding of the atmosphere from low Earth orbit: Preliminary results, *Bulletin of the American Meteorological Society*, *77*, 19–40, 1996.

Yuan, L. L., R. A. Anthes, R. H. Ware, C. Rocken, W. D. Bonner, M. G. Bevis, and S. Bussinger, Sensing climate change using the global positioning system, *Journal of Geophysical Research*, *98*, 14,925–14,937, 1993.

Zehnder, J. A., and P. R. Bannon, Frontogenesis over a mountain ridge, *Journal of the Atmospheric Sciences*, *45*, 628–644, 1988.

Zou, X., Y.-H. Kuo, and Y.-R. Guo, Assimilation of atmospheric radio refractivity using a nonhydrostatic adjoint model, *Monthly Weather Review*, *123*, 2229–2249, 1995.

Zou, X., F. Vandenberghe, B. Wang, M. E. Gorbunov, Y.-H. Kuo, S. Sokolovskiy, J. C. Chang, J. G. Sela, and R. Anthes, Direct assimilation of GPS/MET refraction angle measurements: Part I: Concept and results of raytracing, *Journal of Geophysical Research - Atmosphere*, 1998a, submitted.

Zou, X., B. Wang, F. Vandenberghe, M. E. Gorbunov, Y.-H. Kuo, S. Sokolovskiy, J. C. Chang, J. G. Sela, and R. Anthes, Direct assimilation of GPS/MET refraction angle measurements: Part II: variational assimilation using adjoint techniques, *Journal of Geophysical Research - Atmosphere*, 1998b, submitted.

Appendix A

Discretization of the Abel Transform

In this Appendix we discretize equation (3.32), having n measurements of bending angles α_j ($j = 1, 2, \ldots, n$) and corresponding impact parameters a_j. First we write the equation in the form

$$N(a) = \int_{a_1}^{b} A(x,a)\alpha(x)dx, \tag{A.1}$$

where

$$A(x,a) = \begin{cases} 0 & , \quad x < a \\ -\frac{1}{\pi\sqrt{x^2-a^2}} & , \quad x \geq a \end{cases}$$

is the kernel. a_1 is the lowest impact parameter and at some value $b \equiv a_{n+1} > a_n$ and above we shall assume the bending angle to be negligible. The atmosphere may be thought of as being divided into n spherical shells each with thickness $\Delta a_j = a_{j+1} - a_j$. Provided that each shell thickness is thin enough, $\alpha(a)$ may be approximated as a linear function of the impact parameter in each shell. Thus, between a_j and a_{j+1} we may write

$$\alpha(x) = \frac{x - a_j}{\Delta a_j}\alpha_{j+1} + \frac{a_{j+1} - x}{\Delta a_j}\alpha_j. \tag{A.2}$$

Splitting up the integration into n sub-integrals, we therefore get

$$N(a) = \sum_{j=1}^{n} \int_{a_j}^{a_{j+1}} A(x,a)[\frac{x - a_j}{\Delta a_j}\alpha_{j+1} + \frac{a_{j+1} - x}{\Delta a_j}\alpha_j]dx \tag{A.3}$$

with $\alpha_{n+1} = 0$ per definition. The integral in (A.3) may be solved analytically to yield

$$\frac{\alpha_{j+1}}{\Delta a_j}\int_{a_j}^{a_{j+1}} A(x,a)(x - a_j)dx$$
$$= \frac{\alpha_{j+1}}{\pi\Delta a_j}\left[\sqrt{a_{j+1}^2 - a^2} - \sqrt{a_j^2 - a^2} - a_j \ln\left(\frac{a_{j+1} + \sqrt{a_{j+1}^2 - a^2}}{a_j + \sqrt{a_j^2 - a^2}}\right)\right] \tag{A.4}$$

and

$$\frac{\alpha_j}{\Delta a_j}\int_{a_j}^{a_{j+1}} A(x,a)(a_{j+1}-x)dx$$
$$= -\frac{\alpha_j}{\pi\Delta a_j}\left[\sqrt{a_{j+1}^2-a^2}-\sqrt{a_j^2-a^2}-a_{j+1}\ln\Big(\frac{a_{j+1}+\sqrt{a_{j+1}^2-a^2}}{a_j+\sqrt{a_j^2-a^2}}\Big)\right], \quad \text{(A.5)}$$

assuming $a \leq a_j$. The refractivity, $N_i = N(a_i)$, at impact parameter a_i (chosen to be coincident with one of the a_j's) may now be written as

$$\begin{aligned} N_i = &\frac{1}{\pi}\sum_{j=i}^{n}\frac{\alpha_{j+1}}{\Delta a_j}\left[\sqrt{a_{j+1}^2-a^2}-\sqrt{a_j^2-a^2}-a_j\ln\Big(\frac{a_{j+1}+\sqrt{a_{j+1}^2-a^2}}{a_j+\sqrt{a_j^2-a^2}}\Big)\right] \\ &-\frac{1}{\pi}\sum_{j=i}^{n}\frac{\alpha_j}{\Delta a_j}\left[\sqrt{a_{j+1}^2-a^2}-\sqrt{a_j^2-a^2}-a_{j+1}\ln\Big(\frac{a_{j+1}+\sqrt{a_{j+1}^2-a^2}}{a_j+\sqrt{a_j^2-a^2}}\Big)\right]. \end{aligned} \quad \text{(A.6)}$$

Rearranging the first summation on the right-hand side of (A.6), exploiting that $\alpha_{n+1} = 0$, we arrive at

$$\begin{aligned} N_i = &-\frac{1}{\pi\Delta a_i}\left[\sqrt{a_{i+1}^2-a_i^2}-a_{i+1}\ln\Big(\frac{a_{i+1}+\sqrt{a_{i+1}^2-a_i^2}}{a_i}\Big)\right]\alpha_i \\ &+\frac{1}{\pi}\sum_{j=i+1}^{n}\left\{\frac{1}{\Delta a_{j-1}}\left[\sqrt{a_j^2-a_i^2}-\sqrt{a_{j-1}^2-a_i^2}-a_{j-1}\ln\Big(\frac{a_j+\sqrt{a_j^2-a_i^2}}{a_{j-1}+\sqrt{a_{j-1}^2-a_i^2}}\Big)\right]\right. \\ &\left.-\frac{1}{\Delta a_j}\left[\sqrt{a_{j+1}^2-a_i^2}-\sqrt{a_j^2-a_i^2}-a_{j+1}\ln\Big(\frac{a_{j+1}+\sqrt{a_{j+1}^2-a_i^2}}{a_j+\sqrt{a_j^2-a_i^2}}\Big)\right]\right\}\alpha_j, \end{aligned} \quad \text{(A.7)}$$

from which equation (3.33) follows directly.

Appendix B

Derivation of the Refractivity Field of a Frontal System

For fast ray-tracing purposes, simulating occultations, it is necessary to have a direct expression for the refractivity fields, since it is the refractivity gradients that determines the ray path. The goal here is to find an analytic expression for the 2D refractivity field across a frontal system, and at the same time assuring that hydrostatic integration (although not being strictly valid in a frontal zone) results in a typical temperature field of a frontal system having a warm and a cold side. It is also important to be able to express the refractivity field by a few key parameters like temperature difference, frontal slope, and characteristic horizontal scale of gradients. To simplify things, the effect of water vapor is not taken into account.

The starting point is a model for the potential temperature, θ_{f}, across a 2D frontal system [*Zehnder and Bannon*, 1988]:

$$\theta_{\mathrm{f}}(x,z) = \frac{\Delta T}{\pi} \arctan(\frac{x+Sz}{L}), \tag{B.1}$$

where ΔT is the temperature difference between the cold and the warm region, S is the horizontal/vertical slope of the front, and L is the characteristic horizontal scale of gradients. The total potential temperature field, θ, is then given by the superposition of a background field, θ_{b}, and the frontal system disturbance, θ_{f}:

$$\theta(x,z) = \theta_{\mathrm{b}}(z) + \theta_{\mathrm{f}}(x,z). \tag{B.2}$$

Poisson's equation relating real (dry) temperature, T, and potential temperature is given by [e.g., *Holton*, 1992]

$$T \approx \theta \sigma^{R/c_p}, \tag{B.3}$$

where σ is the sigma coordinate defined as p/p_{s}, p being the pressure, and p_{s} being the surface pressure[1]. In (B.3), R is the gas constant for dry air, and c_p is the specific heat at constant pressure. Substituting (B.3) into the dry air refractivity equation, $N = k_1 p/T$, gives an expression for the refractivity in terms of σ, θ, and p_{s}:

$$N = k_1 p_{\mathrm{s}} \frac{\sigma^{(1-R/c_p)}}{\theta}. \tag{B.4}$$

[1]Usually Poisson's equation is defined with p_{s} being a constant pressure level, but here, p_{s}, being the surface pressure, is allowed to vary horizontally across the front.

The hydrostatic equilibrium assumption gives

$$\sigma^{R/c_p} = 1 - \frac{g}{c_p}\int_0^z \frac{1}{\theta}dz, \tag{B.5}$$

with g being the mean gravitational constant. Substitution of (B.2) into (B.5) and doing a Taylor expansion to first order assuming $\theta_\mathrm{f} \ll \theta_\mathrm{b}$, gives

$$\sigma^{R/c_p} = \left(1 - \frac{g}{c_p}\int_0^z \frac{1}{\theta_\mathrm{b}}dz\right) + \frac{g}{c_p}\int_0^z \frac{\theta_\mathrm{f}}{\theta_\mathrm{b}^2}dz, \tag{B.6}$$

or

$$\sigma^{R/c_p} = (\sigma^{R/c_p})_\mathrm{b} + (\sigma^{R/c_p})_\mathrm{f}, \tag{B.7}$$

where $(\sigma^{R/c_p})_\mathrm{b} = \sigma_\mathrm{b}^{R/c_p}$ is the background sigma coordinate to the power of R/c_p. The frontal term, $(\sigma^{R/c_p})_\mathrm{f}$, can be integrated analytically assuming the background potential temperature to be

$$\theta_\mathrm{b}(z) = \theta_0 + \Gamma_\theta z, \tag{B.8}$$

where $\theta_0 = T_0 = 288.15$ K is the surface temperature for a standard atmosphere, and $\Gamma_\theta \approx 3.26$ K/km is the corresponding potential temperature lapse rate in the lower troposphere. The result of the integration is

$$\begin{aligned}(\sigma^{R/c_p})_\mathrm{f} = \frac{\Delta T}{\pi}\frac{g}{c_p\Gamma_\theta}\Bigg[&\left(\frac{1}{\theta_0} + B(x)\right)\arctan(\frac{x}{L}) \\ &- \left(\frac{1}{\theta_0 + \Gamma_\theta z} + B(x)\right)\arctan(\frac{x+Sx}{L}) \\ &+ A(x)\ln\left(\frac{(\theta_0+\Gamma_\theta z)^2\left(1+(\frac{x}{L})^2\right)}{\theta_0^2\left(1+(\frac{x+Sz}{L})^2\right)}\right)\Bigg]\end{aligned} \tag{B.9}$$

with

$$A(x) = \frac{\Gamma_\theta L}{2S\,C(x)}, \qquad B(x) = \frac{\Gamma_\theta x - S\theta_0}{S\,C(x)},$$
$$C(x) = \left(\frac{\Gamma_\theta L}{S}\right)^2\left(1+\left(\frac{x}{L}\right)^2\right) + \theta_0^2 - \frac{2\theta_0\Gamma_\theta x}{S}.$$

Next, we assume the surface pressure across the frontal system to be of the form

$$p_\mathrm{s} = p_\mathrm{sb}\left[1 + \frac{\Delta T\,g}{2R\,S\,T_0^2}\left(\sqrt{(2L)^2 + \left(D\tanh(\frac{x}{D})\right)^2} - \sqrt{(2L)^2 + D^2}\right)\right], \tag{B.10}$$

or

$$p_\mathrm{s} = p_\mathrm{sb}(1 + \frac{p_\mathrm{sf}}{p_0}), \tag{B.11}$$

where p_sb is the background surface pressure, p_sf is the frontal disturbance of surface pressure (defined by comparing (B.10) and (B.11)), $p_0 = 1013.25$ hPa is the surface pressure for the standard atmosphere, and D is a characteristic horizontal low-pressure

distance. The expression (B.10) gives zero disturbance as $|x| \to \infty$, has a minimum at $x = 0$, and ensures the correct change in pressure gradients across the frontal surface (in the limit $L \to 0$) given by the relation [*Haltiner and Martin*, 1957]

$$S = \frac{g\Delta\rho}{\Delta(\partial p/\partial x)}, \tag{B.12}$$

where $\Delta\rho$ is the air density difference between the cold and the warm region, and $\Delta(\partial p/\partial x)$ is the corresponding pressure difference.

Now (B.2), (B.7), and (B.11) are substituted into (B.4) to obtain

$$N = k_1 p_{\mathrm{sb}} \left(1 + \frac{p_{\mathrm{sf}}}{p_0}\right) \frac{\sigma_{\mathrm{b}}^{1-R/c_p} \left(1 + \frac{(\sigma^{R/c_p})_{\mathrm{f}}}{(\sigma^{R/c_p})_{\mathrm{b}}}\right)^{c_p/R-1}}{\theta_{\mathrm{b}} \left(1 + \frac{\theta_{\mathrm{f}}}{\theta_{\mathrm{b}}}\right)}, \tag{B.13}$$

or

$$N = N_{\mathrm{b}} \left(1 + \frac{p_{\mathrm{sf}}}{p_0}\right) \frac{\left(1 + \frac{(\sigma^{R/c_p})_{\mathrm{f}}}{(\sigma^{R/c_p})_{\mathrm{b}}}\right)^{c_p/R-1}}{\left(1 + \frac{\theta_{\mathrm{f}}}{\theta_{\mathrm{b}}}\right)}, \tag{B.14}$$

where

$$N_{\mathrm{b}} = k_1 p_{\mathrm{sb}} \frac{\sigma_{\mathrm{b}}^{(1-R/c_p)}}{\theta_{\mathrm{b}}} \tag{B.15}$$

is the background refractivity obtained from an independent model.

Equation (B.8) is only valid in the lower troposphere, and substituting (B.8) into (B.5) gives negative values of $(\sigma^{R/c_p})_{\mathrm{b}}$ for $z \approx 30$ km and above, which is unphysical. Therefore it is preferable to use better approximations for θ_{b} and $(\sigma^{R/c_p})_{\mathrm{b}}$ in (B.14):

$$\theta'_{\mathrm{b}}(z) = (\theta_0 - \Gamma_\theta H_\theta) + \Gamma_\theta H_\theta \exp(z/H_\theta), \tag{B.16}$$

and

$$(\sigma^{R/c_p})'_{\mathrm{b}}(z) = 1 - \frac{g}{c_p} \frac{1}{(\theta_0 - \Gamma_\theta H_\theta)} \left(z - H_\theta \ln(\frac{\theta'_{\mathrm{b}}(z)}{\theta_0})\right). \tag{B.17}$$

The form (B.16) has the advantage that substituted into (B.5), it can be integrated analytically to obtain (B.17). Its first order approximation for small z is equal to (B.8), thereby having the correct standard atmosphere potential lapse rate in the lower troposphere, and generally it has the exponential increase characteristic for the potential temperature throughout the troposphere and stratosphere. The potential temperature scale height, H_θ, is determined from (B.17) by the requirement that $(\sigma^{R/c_p})'_{\mathrm{b}} \to 0$ for $z \to \infty$. Using standard atmosphere parameters for θ_0 and Γ_θ, gives $H_\theta \approx 13.2$ km.

Also because of the assumption (B.8), equation (B.9) is only valid at low altitudes, and needs to be effectively "killed" at high altitudes. This can be achieved by

$$(\sigma^{R/c_p})'_{\mathrm{f}} = (\sigma^{R/c_p})_{\mathrm{f}} \exp\left(-\left(\frac{z}{U_z}\right)^4\right), \tag{B.18}$$

U_z being a vertical decay scale.

Taylor expansion of (B.14) to first order, assuming $p_{\mathrm{sf}} \ll p_0$, $\theta_{\mathrm{f}} \ll \theta'_{\mathrm{b}}$, and $(\sigma^{R/c_p})'_{\mathrm{f}} \ll (\sigma^{R/c_p})'_{\mathrm{b}}$ gives

$$N = N_{\mathrm{b}} \left(1 + \frac{p_{\mathrm{sf}}}{p_0} + (\frac{c_p}{R} - 1) \frac{(\sigma^{R/c_p})'_{\mathrm{f}}}{(\sigma^{R/c_p})'_{\mathrm{b}}} - \frac{\theta_{\mathrm{f}}}{\theta'_{\mathrm{b}}} \right), \tag{B.19}$$

or

$$N = N_{\mathrm{b}}(1 + \frac{N_{\mathrm{f}}}{N_{\mathrm{b}}}), \tag{B.20}$$

where N_{f} is the frontal disturbance of refractivity (defined by comparing (B.19) and (B.20)). To delimit the horizontal extend of the frontal zone the frontal disturbance is modified:

$$N'_{\mathrm{f}} = N_{\mathrm{f}} \exp\left(-\left(\frac{r}{U_r} \right)^4 \right), \tag{B.21}$$

where r is the distance between the location of the point in request and the center location of the front, and U_r is a horizontal decay scale.

Finally, to place the front on a sphere, the following parameters are defined:

$$x = r\cos(Q_0 - Q), \tag{B.22}$$

$$r = \Theta R_{\mathrm{mean}}, \tag{B.23}$$

$$\cos\Theta = \cos(\vartheta)\cos(\vartheta_0) + \sin(\vartheta)\sin(\vartheta_0)\cos(\varphi - \varphi_0), \tag{B.24}$$

$$\tan Q = \frac{\sin(\varphi - \varphi_0)\sin(\vartheta)\sin(\vartheta_0)}{\cos(\vartheta) - \cos(\Theta)\cos(\vartheta_0)}, \tag{B.25}$$

where
Q_0 is the angle between the orientation of the front (defined as the direction of steepest horizontal gradient), and the direction towards north. In polar coordinates on the globe, the origin is at the center location of the front given by (ϑ_0, φ_0), and Q_0 is positive eastward from north,
Q is the angle between the direction of the point in request given by (ϑ, φ), and the direction towards north. In polar coordinates on the globe, the origin is at the center of the front, and Q is positive eastward from north,
Θ is the distance (in radians) between the location of the point in request, and the center location of the front,
ϑ_0 is the center co-latitude of the frontal system,
φ_0 is the center longitude of the frontal system,
ϑ is the co-latitude of the point in request,
φ is the longitude of the point in request,
and R_{mean} is the Earth mean radius.

Using the following values for the key parameters, and superimposed on a 1D background refractivity field, gives the temperature field in Figure 4.4 when the refractivity is hydrostatically integrated from above:
$\Delta T = 31.4$ K, $S = 100$, $L = 200$ km, $D = 200$ km, $U_z = 30$ km, and $U_r = 5000$ km.

Appendix C

Published and Submitted Papers

C.1 On the Ionosphere Calibration in GPS Occultation Measurements [*Syndergaard*, 1999b]

C.2 Modeling the Impact of the Earth's Oblateness on the Retrieval of Temperature and Pressure Profiles from Limb Sounding [*Syndergaard*, 1998]

C.3 Inversion of GPS Occultation Data for Atmospheric Profiling [*Syndergaard*, 1999a]

DANISH METEOROLOGICAL INSTITUTE

Scientific Reports

Scientific reports from the Danish Meteorological Institute cover a variety of geophysical fields, i.e. meteorology (including climatology), oceanography, subjects on air and sea pollution, geomagnetism, solar-terrestrial physics, and physics of the middle and upper atmosphere.

Reports in the series within the last five years:

No. 94-1
Bjørn M. Knudsen: Dynamical processes in the ozone layer

No. 94-2
J. K. Olesen and K. E. Jacobsen: On the atmospheric jet stream with clear air turbulences (CAT) and the possible relationship to other phenomena including HF radar echoes, electric fields and radio noise

No. 94-3
Ole Bøssing Christensen and Bent Hansen Sass: A description of the DMI evaporation forecast project

No. 94-4
I.S. Mikkelsen, B. Knudsen, E. Kyrö and M. Rummukainen: tropospheric ozone over Finland and Greenland, 1988-94
Not published

No. 94-5
Jens Hesselbjerg Christensen, Eigil Kaas, Leif Laursen: The contribution of the Danish Meteorological Institute (DMI) to the EPOCH project "The climate of the 21st century" No. EPOC-003-C (MB)

No. 95-1
Peter Stauning and T.J. Rosenberg:
High-Latitude, day-time absorption spike events
1. morphology and occurrence statistics
Not published

No. 95-2
Niels Larsen: Modelling of changes in stratospheric ozone and other trace gases due to the emission changes : CEC Environment Program Contract No. EV5V-CT92-0079. Contribution to the final report

No. 95-3
Niels Larsen, Bjørn Knudsen, Paul Eriksen, Ib Steen Mikkelsen, Signe Bech Andersen and Torben Stockflet Jørgensen: Investigations of ozone, aerosols, and clouds in the arctic stratosphere : CEC Environment Program Contract No. EV5V-CT92-0074. Contribution to the final report

No. 95-4
Per Høeg and Stig Syndergaard: Study of the derivation of atmospheric properties using radio-occultation technique

No. 95-5
Xiao-Ding Yu, **Xiang-Yu Huang** and **Leif Laursen** and Erik Rasmussen: Application of the HIRLAM system in China: heavy rain forecast experiments in Yangtze River Region

No. 95-6
Bent Hansen Sass: A numerical forecasting system for the prediction of slippery roads

No. 95-7
Per Høeg: Proceeding of URSI International Conference, Working Group AFG1 Copenhagen, June 1995. Atmospheric research and applications using observations based on the GPS/GLONASS System
Not published

No. 95-8
Julie D. Pietrzak: A comparison of advection schemes for ocean modelling

No. 96-1
Poul Frich (co-ordinator), H. Alexandersson, J. Ashcroft, B. Dahlström, G.R. Demarée, A. Drebs, A.F.V. van Engelen, E.J. Førland, I. Hanssen-Bauer, R. Heino, T. Jónsson, K. Jonasson, L. Keegan, P.Ø. Nordli, **T. Schmith**, **P. Steffensen**, H. Tuomenvirta, O.E. Tveito: North Atlantic Climatological Dataset (NACD Version 1) - Final report

No. 96-2
Georg Kjærgaard Andreasen: Daily response of high-latitude current systems to solar wind variations: application of robust multiple regression. Methods on Godhavn magnetometer data

No. 96-3
Jacob Woge Nielsen, Karsten Bolding Kristensen, Lonny Hansen: Extreme sea level highs: a statistical tide gauge data study

No. 96-4
Jens Hesselbjerg Christensen, Ole Bøssing Christensen, Philippe Lopez, Erik van Meijgaard, Michael Botzet: The HIRLAM4 Regional Atmospheric Climate Model

No. 96-5
Xiang-Yu Huang: Horizontal diffusion and filtering in a mesoscale numerical weather prediction model

No. 96-6
Henrik Svensmark and Eigil Friis-Christensen: Variation of cosmic ray flux and global cloud coverage - a missing link in solar-climate relationships

No. 96-7
Jens Havskov Sørensen and Christian Ødum Jensen: A computer system for the management of epidemiological data and prediction of risk and economic consequences during outbreaks of foot-and-mouth disease. CEC AIR Programme. Contract No. AIR3 - CT92-0652

No. 96-8
Jens Havskov Sørensen: Quasi-automatic of input for LINCOM and RIMPUFF, and output conversion. CEC AIR Programme. Contract No. AIR3 - CT92-0652

No. 96-9
Rashpal S. Gill and Hans H. Valeur:
Evaluation of the radarsat imagery for the operational mapping of sea ice around Greenland

No. 96-10
Jens Hesselbjerg Christensen, Bennert Machenhauer, Richard G. Jones, Christoph Schär, Paolo Michele Ruti, Manuel Castro and Guido Visconti:
Validation of present-day regional climate simulations over Europe: LAM simulations with observed boundary conditions

No. 96-11
Niels Larsen, Bjørn Knudsen, Paul Eriksen, Ib Steen Mikkelsen, Signe Bech Andersen and Torben Stockflet Jørgensen: European Stratospheric Monitoring Stations in the Artic: An European contribution to the Network for Detection of Stratospheric Change (NDSC): CEC Environment Programme Contract EV5V-CT93-0333: DMI contribution to the final report

No. 96-12
Niels Larsen: Effects of heterogeneous chemistry on the composition of the stratosphere: CEC Environment Programme Contract EV5V-CT93-0349: DMI contribution to the final report

No. 97-1
E. Friis Christensen og C. Skøtt: Contributions from the International Science Team. The Ørsted Mission - a pre-launch compendium

No. 97-2
Alix Rasmussen, Sissi Kiilsholm, Jens Havskov Sørensen, Ib Steen Mikkelsen: Analysis of tropospheric ozone measurements in Greenland: Contract No. EV5V-CT93-0318 (DG 12 DTEE): DMI's contribution to CEC Final Report Arctic Trophospheric Ozone Chemistry ARCTOC

No. 97-3
Peter Thejll: A search for effects of external events on terrestrial atmospheric pressure: cosmic rays

No. 97-4
Peter Thejll: A search for effects of external events on terrestrial atmospheric pressure: sector boundary crossings

No. 97-5
Knud Lassen: Twentieth century retreat of sea-ice in the Greenland Sea

No. 98-1
Niels Woetman Nielsen, Bjarne Amstrup, Jess U. Jørgensen:
HIRLAM 2.5 parallel tests at DMI: sensitivity to type of schemes for turbulence, moist processes and advection

No. 98-2
Per Høeg, Georg Bergeton Larsen, Hans-Henrik Benzon, Stig Syndergaard, Mette Dahl Mortensen: The GPSOS project. Algorithm functional design and analysis of ionosphere, stratosphere and troposphere observations

No. 98-3
Mette Dahl Mortensen, Per Høeg:
Satellite atmosphere profiling retrieval in a nonlinear troposphere
Previously entitled: Limitations induced by Multipath

No. 98-4
Mette Dahl Mortensen, Per Høeg:
Resolution properties in atmospheric profiling with GPS

No. 98-5
R.S. Gill and M. K. Rosengren
Evaluation of the Radarsat imagery for the operational mapping of sea ice around Greenland in 1997

No. 98-6
R.S. Gill, H.H. Valeur, P. Nielsen and K.Q. Hansen: Using ERS SAR images in the operational mapping of sea ice in the Greenland waters: final report for ESA-ESRIN's: pilot projekt no. PP2.PP2.DK2 and 2nd announcement of opportunity for the exploitation of ERS data projekt No. AO2..DK 102
Not published

No. 98-7
Per Høeg et al.: GPS Atmosphere profiling methods and error assessments

No. 98-8
H. Svensmark, N. Woetmann Nielsen and A.M. Sempreviva: Large scale soft and hard turbulent states of the atmosphere

No. 98-9
Philippe Lopez, Eigil Kaas and Annette Guldberg: The full particle-in-cell advection scheme in spherical geometry

No. 98-10
H. Svensmark: Influence of cosmic rays on earth's climate

No. 98-11
Peter Thejll and Henrik Svensmark: Notes on the method of normalized multivariate regression

No. 98-12
K. Lassen: Extent of sea ice in the Greenland Sea 1877-1997: an extension of DMI Scientific Report 97-5

No. 98-13
Niels Larsen, Alberto Adriani and Guido Di-Donfrancesco: Microphysical analysis of polar stratospheric clouds observed by lidar at McMurdo, Antarctica

No.98-14
Mette Dahl Mortensen: The back-propagation method for inversion of radio occultation data

No. 98-15
Xiang-Yu Huang: Variational analysis using spatial filters

No. 99-1
Henrik Feddersen: Project on prediction of climate variations on seasonel to interannual timescales (PROVOST) EU contract ENVA4-CT95-0109: DMI contribution to the final report:Statistical analysis and post-processing of uncoupled PROVOST simulations

No. 99-2
Wilhelm May: A time-slice experiment with the ECHAM4 A-GCM at high resolution: the experimental design and the assessment of climate as compared to a greenhouse gas experiment with ECHAM4/OPYC at low resolution

No. 99-3
Niels Larsen et al.: European stratospheric monitoring stations in the Artic II: CEC Environment and Climate Programme Contract ENV4-CT95-0136. DMI Contributions to the project
(In Press)

No. 99-4
Alexander Baklanov: Parameterisation of the deposition processes and radioactive decay: a review and some preliminary results with the DERMA model
(In Press)

No. 99-5
Mette Dahl Mortensen: Non-Linear High Resolution Inversion of Radio Occultation Data

No. 99-6
Stig Syndergaard: Retrieval analysis and methodologies in atmospheric limb sounding using the GNSS radio occultation technique